Charles University in Prague
Faculty of Mathematics and Physics

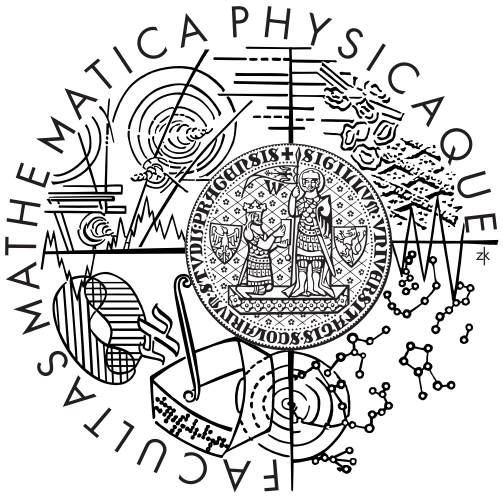

Hyperfine Interactions in Ferrites with Spinel Structure

Ph.D. Thesis

Vojtěch Chlan

Supervisor: prof. RNDr. Helena Štěpánková, CSc.

F-3: Physics of Condensed Matter and Materials Research

Prague 2010

Acknowledgements

I wish to express gratitude to my supervisor prof. RNDr. Helena Štěpánková, CSc. for her inspiring and patient guidance, for introducing me into the field of nuclear magnetic resonance and for teaching me how a physicist works.

I am much obliged to Ing. Pavel Novák, CSc. for introducing me into calculations of electron structure and for giving answers and hints whenever I needed.

I value all the people with whom I collaborated during my studies and work on the thesis. I wish to thank to people who kindly granted their samples, prof. V. A. M. Brabers from Technical University of Eindhoven, RNDr. Zdeněk Šimša, CSc. and RNDr. Zdeněk Jirák, CSc. from Institute of Physics, Dr. V. D. Doroshev from Donetsk Physicotechnical Institute, prof. J. M. Honig from Purdue University in West Lafayette, prof. dr hab. Inż. Andrzej Kozłowski and prof. dr hab. Inż. Zbigniew Kąkol from AGH University of Kraków. I express gratitude to Ing. Miroslav Maryško, CSc. from Institute of Physics, prof. dr hab. Inż. Andrzej Kozłowski and prof. dr hab. Inż. Zbigniew Kąkol for various magnetization measurements, and to prof. RNDr. Josef Štěpánek, CSc. for introducing me into Singular Value Decomposition used to analyse the NMR dynamics data.

I would also like to thank to my colleagues from the Department of Low Temperature Physics, for technical support and for friendly and pleasant atmosphere.

The calculations of electron structure used in this thesis were performed at subcluster Dorje of the computing centre Golias at the Institute of Physics.

This work was supported by grant 202/2006 B FYZ of the Grant Agency of Charles University.

Contents

Chapter 1

Introduction

The presented thesis focuses on three systems of transition metal oxides with spinel structure: manganese ferrite, lithium ferrite and magnetite. These magnetic systems belong to materials of great importance in today's technological applications, yet there are open issues concerning some of their fundamental physical properties, e.g. the arrangement and valence states of cations in manganese ferrite, or many interesting phenomena connected with low temperature structure of magnetite.

Two main methods are employed to investigate the above mentioned spinel systems: nuclear magnetic resonance (NMR) and the first principle calculations of electronic structure. NMR is a well suited experimental method for studying magnetic materials, as it easily distinguishes different magnetic sublattices and allows to inspect various details in the local structure. The calculations, based on density functional theory (DFT), are used as a complementary theoretical approach, helping to interpret the experimental results, as well as further elaborate the findings. And conversely, NMR provides a solid experimental framework for the calculated properties.

Although the studied ferrites are—as for the structure—all spinels, from the viewpoint of the applied methods, they offer a variety of observable properties and phenomena. The manganese ferrite and magnetite involve a complex mixture of several cationic states, in contrast to the well defined structure of ordered lithium ferrite. The structure of magnetite at low temperatures represents a unique system displaying interplay between various types of ordering.

The thesis opens with description of the studied systems and a brief survey of both applied methods (chapters 2, 3, and 4). The particular

procedures and practices, that were adopted and applied, are summarized in chapters 5 and 6.

The main topic of the thesis is presented and discussed in chapters 7, 8, and 9. Chapter 7 reports on manganese ferrites with different degrees of inversion and manganese contents, comprising collaboration of both applied methods. Capability of calculations to complement the NMR method is further demonstrated in chapter 8, where calculated anisotropy of hyperfine fields is confronted with NMR results. This new approach, developed on ordered lithium ferrite, is then applied to a much complex system of magnetite in chapter 9. Besides, switching of magnetic easy axis in magnetite below the Verwey transition and accompanying processes are observed by NMR and magnetic measurements and analyzed. Also, NMR experiments and calculations concerning magnetite with cationic vacancies are presented in chapter 9.

Chapter 2

Ferrites with Spinel Structure

Spinel ferrites have been studied for many years regarding their interesting structural and magnetic properties. Because a large number of these materials can be prepared as room temperature insulating ferromagnets, they play an important role in various technological devices. Manganese ferrite $MnFe_2O_4$ has been widely used in microwave and magnetic recording applications, and also lithium ferrite $Li_{0.5}Fe_{2.5}O_4$ is an important material for applications at microwave frequencies [1]. Magnetite Fe_3O_4 is well known, e.g. for its extensive use in traditional recording media and for its role in the emerging field of spintronics [2, 3].

2.1 Crystal Structure

Oxides with spinel structure have a general formula XY_2O_4, crystallize in the cubic crystal system and belong to the space group $Fd\bar{3}m$ (O_h^7). Oxygen anions arranged in a cubic close packed lattice form 64 tetrahedrons and 32 octahedrons in an unit cell. The cations X and Y occupy 8 of tetrahedral sites (A sites) and 16 of octahedral sites (B sites) respectively; the conventional unit cell then contains eight of such XY_2O_4 formula units.

In real crystals the perfect oxygen cubic close packed lattice is distorted by a small shift of the oxygen towards the nearest cationic neighbour in tetrahedral site. Tetrahedrons of the A sites are regular, while the octahedrons of the B sites are trigonally distorted with C_3 axis in one of $\langle 111 \rangle$ directions (see Table 2.1). More detailed description may be found in [4].

Site label	Number of sites	Site symmetry	Coordinates in primitive cell
a (A site)	8	$\bar{4}3m$ (T_d)	$\frac{1}{8}, \frac{1}{8}, \frac{1}{8}$ $\frac{1}{8}, \frac{1}{8}, \frac{1}{8}$
d (B site)	16	$\bar{3}m$ (D_{3d})	$\frac{1}{2}, 0, 0$ $\frac{1}{4}, \frac{1}{4}, \frac{1}{2}$ $\frac{3}{4}, \frac{1}{2}, \frac{3}{4}$ $0, \frac{3}{4}, \frac{1}{4}$
e	32	$3m$ (C_{3v})	$\frac{3}{4}+u, 1-u, \frac{1}{2}-u$ $\frac{3}{4}-u, u, u$ $u, \frac{1}{4}-u, \frac{1}{2}+u$ $1-u, \frac{1}{4}+u, 1-u$ $\frac{1}{2}-u, \frac{1}{2}-u, \frac{1}{4}+u$ $\frac{1}{2}+u, \frac{1}{2}+u, \frac{3}{4}-u$ $\frac{1}{4}-u, \frac{3}{4}-u, \frac{1}{4}+u$ $\frac{1}{4}+u, \frac{3}{4}+u, \frac{3}{4}+u$

Table 2.1: Occupied equivalent sites of the Fd$\bar{3}$m space group in one primitive cell are shown. Origin of the cell is taken at an octahedral site, the remaining positions in the conventional unit cell can be obtained through translations: $(0, \frac{1}{2}, \frac{1}{2})$, $(\frac{1}{2}, 0, \frac{1}{2})$, $(\frac{1}{2}, \frac{1}{2}, 0)$. The oxygen parameter u depends on the type of cations and their ionic radii; for ferrites the value of u is typically 0.005–0.015.

As the electronegativity of oxygen is large, the character of bonds in spinel oxides is rather of ionic type, which leads to several common aspects of these compounds. Ionic character of bonds is connected e.g. with usually low electric conductivity, which allows classifying these compounds as insulators. Also, in general, the spinel structure is very stable, and therefore, allows wide variety of cations entering the structure. Likewise, the structure is flexible, and so different cation arrangements at the A and B sites or even considerable concentration of cation vacancies is possible. The translation and local symmetries corresponding to the Fd$\bar{3}$m space group, however, strictly apply to the spinel structure where each sublattice contains only one kind of cations, i.e. all ions X occupy A sites and all ions Y occupy B sites. Such spinel structure is then called normal. In the case of different cations coexisting in the same sublattice, the symmetry is perturbed and additional parameter describing the deviation from normal spinel is needed.

The distribution of cations between A and B sites in XY_2O_4 may be described by formula $(X_{1-y}Y_y)_A[X_yY_{2-y}]_BO_4$, where y denotes the degree of inversion. For normal spinel, $y = 0$, while for 'inverse' spinel structure, $y = 1$, i.e. all ions X enter B sites and ions Y occupy all A sites and also the remaining half of B sites. Degree of inversion y is therefore defined as an amount of X and Y pairs that are swapped between the sublattices with respect to normal spinel $(X)_A[Y_2]_BO_4$. Spinel structures with ionic distri-

bution between normal and inverse structure are called mixed or partially inverted.

The degree of inversion in a particular compound is influenced by several factors, such as the magnitude of the ionic radii with respect to the size of given oxygen polyhedron, electronic configuration of the ions and electrostatic energy of the lattice. Moreover, the inversion may be also affected by a method of preparation, thermal treatment and actual history of the sample. For further text let us note that magnetite Fe_3O_4 and lithium ferrite $Li_{0.5}Fe_{2.5}O_4$ form inverse spinel structures, and the structure of manganese ferrite $MnFe_2O_4$ is mixed, i.e. both crystallographic sites are occupied by Mn and Fe. An example of compound with normal spinel structure is $ZnFe_2O_4$ ferrite.

2.2 Electronic Structure

In the case of spinel ferrites or spinels with other transition metal cations, one has to be revise the relatively simple image of insulating compounds with ionic character of bonds and with large energy gap between oxygen $2p$ states and the empty conduction band. The presence of transition metal ions causes additional narrow bands, usually lying in the energy gap. In some cases, as in oxide spinels with $3d$ ions in the A sites only, or in structures with high level of cationic ordering, e.g. normal $ZnFe_2O_4$ or ordered $Li_{0.5}Fe_{2.5}O_4$, the transport within the partially occupied $3d$ bands does not dominate the transport properties. However, when the transition metal ion coexist in different valence states, a rather complex question of electronic structure arises in such mixed valency compounds and disordered systems (e.g. due to partial inversion). Typical examples may be Fe^{2+} and Fe^{3+} ions in the B positions of (partially) inverted ferrites. Investigation of the occupancy of cationic sites, the valence states of the cations, possible charge ordering and its dynamics is then important for understanding the properties of these systems.

2.3 Magnetic Interactions

In oxide spinels the outer d electrons of transition metal cations may be considered as localized, so that the ligand field theory can be applied to deduce the magnetic behaviour. The splitting of energy levels due to ligand field is evocated by both the electrostatic crystal field and the covalence be-

tween the cation and the surrounding oxygen ligands. Both these effects also contribute to the stabilization energy of the cations in given surroundings.

The local symmetry of tetrahedral sites is cubic (T_d) and the symmetry of octahedral sites is trigonal (D_{3d}). Despite this, the dominant part of the ligand field for both sites is cubic, with point groups T_d and O_h. In case of ions from the $3d$ group, the cubic ligand field strength usually corresponds to the so-called intermediate ligand field, i.e. it is weaker than the correlation between equivalent $3d$ electrons but stronger than the spin-orbit coupling.

With respect to the further text relating mostly Fe and Mn ions, assumptions on the spin states of these cations in the spinel structure may be drawn. Both cations are expected to be in the high spin state. The Mn^{2+} and Fe^{3+} ions have then half-filled $3d$ shell, and as a consequence, their ground state is the singlet ^{6}S with spin 5/2 and zero orbital momentum, which is not split by a crystal field. Mn^{3+} has the electron configuration $3d^4$, which in the free ion yields ^{5}D multiplet (both spin and orbital momentum 2) as the ground state. In the regular octahedron this multiplet is split to lower orbital doublet $^5\mathrm{E}_g$ and higher orbital triplet $^5\mathrm{T}_{2g}$ (see e.g. [5] for a detailed discussion). Likewise the ground state of the free Fe^{2+} ion is ^{5}D, but now $^5\mathrm{T}_{2g}$ orbital triplet is the lowest state in an octahedral field. The symmetry of the octahedral sites in the spinel structure is trigonal. Despite this symmetry lowering, the doublet $^5\mathrm{E}_g$ of Mn^{3+} ion is subjected to a Jahn-Teller effect that in most cases leads to a tetragonal elongation of the oxygen octahedron.

Spinels are a typical example of a system allowing ferrimagnetic ordering. As the cations in the spinel structure are mutually separated by large oxygen anions effectively preventing direct overlap between the cationic orbitals, the direct exchange interaction appears to be weak. Instead, indirect exchange via oxygen p orbitals plays an important role, and is strong enough to create the ordering of magnetic moments. The Curie (or Néel) temperature of spinel ferrites is typically very high (even up to $\sim$ 900 K), and depends on compound purity and sample preparation.

Some basic predictions about the exchange interactions, e.g. the sign and relative strength, may be obtained from Goodenough-Kanamori-Anderson rules (GKA). GKA rules concern the spin-spin interactions between two atoms mediated through a virtual electron transfer between those two atoms or via an oxygen ligand shared by these two atoms. While overlapped orbitals allow such electron transfer, no transfer is allowed for orthogonal, i.e. non-overlapping orbitals. GKA rules state that the exchange interactions are antiferromagnetic where the electron transfer is between overlapping or-

bitals that are each half-filled, but they are ferromagnetic where the virtual electron transfer is from a half-filled to an empty orbital or from a filled to a half-filled orbital.

When the GKA rules are applied to the spinel ferrites, the A-B interaction between ions with half-filled $3d$ shell (e.g. Fe^{3+}, Mn^{2+}) is strongly antiferromagnetic (Metal(A)-O-Metal(B) bonds form angle $\sim 125°$) while the coupling between two neighbouring octahedral ions is ferromagnetic and much weaker (the Metal(B)-O-Metal(B) angle is $\sim 90°$). The A-A interactions are usually weaker, but become important when the number of magnetic ions in B sites is reduced, e.g. in $Li_{0.5}Fe_{2.5}O_4$.

2.4 Manganese Ferrite

2.4.1 Structure of Manganese Ferrite

Manganese ferrite belongs to ferrites with partially inverse spinel structure where both cation sublattices are occupied by manganese and iron. The proper distribution of cations in the sublattices is influenced by two factors: manganese content x, and degree of inversion y, describing the transposition of Mn and Fe ions between the sublattices. Furthermore, when the valence states and spin states of the cations are considered, more types of cations must be taken into the account, i.e. Fe^{2+}, Fe^{3+}, Mn^{2+} and Mn^{3+}; other valence states may usually be omitted as they are not preferred states in Mn-Fe ferrites. Therefore, additional parameters ought to be included to describe e.g. valency exchange Fe^{2+}–Fe^{3+} in the B sites.

The degree of inversion y depends strongly on the preparation method and on thermal treatment. Annealing at high temperatures (800 °C) achieves state of inversion close to a random distribution of cations ($y = 1/3$) while annealing at temperatures below 300 °C for a very long time allows to prepare almost normal manganese ferrite. In single crystals y ranges from 0.05 up to 0.30 [6, 7], however, in the polycrystals prepared at low temperatures by precipitation from the water solution, y may be found as high as $y = 0.52$ [8].

As the manganese ferrite is a mixed valence compound with cations partially inverted, the question of charge distribution becomes more complex. While valency states of manganese and iron on the A sublattice are 2+ and 3+ respectively, the situation for B sublattice is less clear. To fulfil the neutrality the valence states in B sublattice may be described by a formula $Mn_y^{3+}Fe_y^{2+}Fe_{2-2y}^{3+}$ [9], which means that iron ions carry the excess of charge

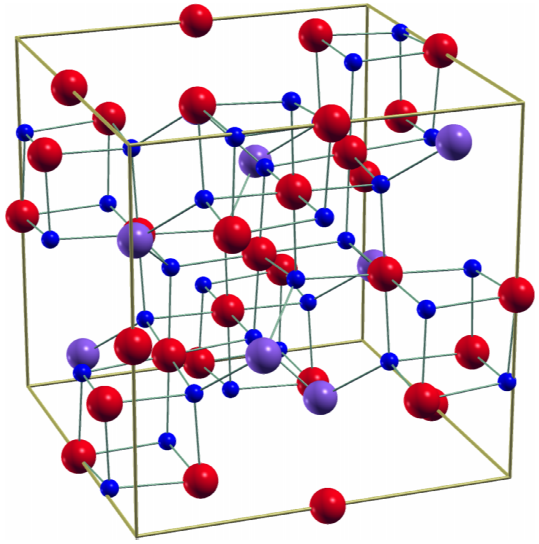

Figure 2.1: Face-centered cubic conventional unit cell of manganese ferrite $(Mn_8)[Fe_{16}]O_{32}$ in $Fd\bar{3}m$ space group. Manganese atoms are purple, iron atoms are red and oxygens are blue. Created using XCrysDen [10].

at the B sites. However, such concept of well defined Fe^{2+} and Fe^{3+} ions is not confirmed by microscopic methods, and so a picture of intermediate ionicity, e.g. $Fe^{2.7+}$, should be considered. Therefore, one of the interesting problems is the localization of an extra electron on the B sublattice that is formally represented by Fe^{2+} ion.

2.4.2 Magnetic Structure of Manganese Ferrite

It is generally accepted that the dominating exchange interaction in spinel ferrites is the antiferromagnetic A-B superexchange [11, 12]. The magnetic easy axis of manganese ferrite is in the $\langle 111 \rangle$ direction. The Mn^{2+} and Fe^{3+} which occupy the A sites have half-filled $3d$ shell (electronic configuration $3d^5$ with spin $S = 5/2$ and zero orbital momentum corresponding to 5 μ_B per formula unit) and their magnetic moments are expected to point in the same direction, antiparallel to the B sublattice magnetization. The moments of the Mn^{3+} and Fe^{2+} on B sites (having 4 and 6 electrons, respectively) possess magnetic moment of 4 μ_B. If the valence states $Mn_y^{3+}Fe_y^{2+}Fe_{2-2y}^{3+}$ in the B sublattice are accepted, then the spin magnetic moment μ_s per formula unit in μ_B is connected with the inversion parameter by the relation

$$\mu_s = 5 - 2y, \tag{2.1}$$

which was tested and evidenced in a number of Mn ferrites with different y [7].

Manganese ferrite is well studied experimentally, e.g. [13], and there are many older studies on ^{55}Mn NMR (e.g. [9, 14, 15, 16, 17, 18]), where ^{55}Mn resonance was found in a frequency range 250–610 MHz. However, ^{57}Fe NMR spectra were only rarely measured ([18, 19, 20]), probably due to low abundance of ^{57}Fe isotope and low sensitivity compared to that of ^{55}Mn isotope. Anisotropy of ^{57}Fe NMR spectra was investigated experimentally by Kovtun *et al.* [19], who measured dependence of ^{57}Fe NMR frequency on direction of external magnetic field in the (011) plane.

Also several theoretical calculations of the exchange interactions in this compound recently appeared [21, 22, 23]. From these studies it follows that the exchange interactions in the manganese ferrite comply with the standard Goodenough-Kanamori-Anderson rules [11, 12]. However, recently Shim *et al.* [20] proposed an abnormal spin structure on the basis of ^{57}Fe NMR spectra measured in polycrystalline manganese ferrite. Shim *et al.* concluded that on the A sites the spins of Mn^{2+} and Fe^{3+} ions are antiparallel and also the Fe^{3+} in the B sites are partially ordered antiferromagnetically. In [24] we showed that their analysis of ^{57}Fe NMR spectra was incorrect, and we reinterpreted these results in compliance with GKA rules.

2.5 Lithium Ferrite

Lithium ferrite $Li_{0.5}Fe_{2.5}O_4$ has been known since 1930's, and two polymorphic modifications of this compound have been identified: disordered and ordered structure.

2.5.1 Structure of Ordered Lithium Ferrite

The formula of lithium ferrite can be written as $(Fe)[Fe_{1.5}Li_{0.5}]O_4$, thus reflecting the distribution of cations in the atomic sites, i.e. lithium atoms occupy octahedral sites only. Lithium ferrite takes a special place among ferrites with spinel structure due to several distinguishing features of its structure.

Most markedly, the distribution of lithium and iron ions in the octahedral sublattice may be either ordered or disordered. At high temperatures (above 735–755 °C) or in a quenched sample, the site occupancy is disordered and the structure can be indexed according to the space group $Fd\bar{3}m$. On the other hand, lithium cations in the octahedral sites of a slowly cooled

Site label	Number of sites	Site symmetry	Coordinates in primitive cell	
c Fe(A)	8	C_3	$x,\ x,\ x$	$-x+\frac{1}{2},\ -x,\ x+\frac{1}{2}$
			$-x,\ x+\frac{1}{2},\ -x+\frac{1}{2}$	$x+\frac{1}{2},\ -x+\frac{1}{2},\ -x$
			$x+\frac{1}{4},\ x+\frac{3}{4},\ -x+\frac{3}{4}$	$-x+\frac{1}{4},\ -x+\frac{1}{4},\ -x+\frac{1}{4}$
			$x+\frac{3}{4},\ -x+\frac{3}{4},\ x+\frac{1}{4}$	$-x+\frac{3}{4},\ x+\frac{1}{4},\ x+\frac{3}{4}$
b Li(B)	4	D_3	$\frac{5}{8},\ \frac{5}{8},\ \frac{5}{8}$	$\frac{7}{8},\ \frac{3}{8},\ \frac{1}{8}$
			$\frac{3}{8},\ \frac{1}{8},\ \frac{7}{8}$	$\frac{1}{8},\ \frac{7}{8},\ \frac{3}{8}$
d Fe(B)	12	C_2	$\frac{1}{8},\ y,\ -y+\frac{1}{4}$	$\frac{3}{8},\ -y,\ -y+\frac{3}{4}$
			$\frac{7}{8},\ y+\frac{1}{2},\ y+\frac{1}{4}$	$\frac{5}{8},\ -y+\frac{1}{2},\ y+\frac{3}{4}$
			$-y+\frac{1}{4},\ \frac{1}{8},\ y$	$-y+\frac{3}{4},\ \frac{3}{8},\ -y$
			$y+\frac{1}{4},\ \frac{7}{8},\ y+\frac{1}{2}$	$y+\frac{3}{4},\ \frac{5}{8},\ -y+\frac{1}{2}$
			$y,\ -y+\frac{1}{4},\ \frac{1}{8}$	$-y,\ -y+\frac{3}{4},\ \frac{3}{8}$
			$y+\frac{1}{2},\ y+\frac{1}{4},\ \frac{7}{8}$	$-y+\frac{1}{2},\ y+\frac{3}{4},\ \frac{5}{8}$
e	24	C_1	$x,\ y,\ z$	$-x+\frac{1}{2},\ -y,\ z+\frac{1}{2}$
			$-x,\ y+\frac{1}{2},\ -z+\frac{1}{2}$	$x+\frac{1}{2},\ -y+\frac{1}{2},\ -z$
			$z,\ x,\ y$	$z+\frac{1}{2},\ -x+\frac{1}{2},\ -y$
			$-z+\frac{1}{2},\ -x,\ y+\frac{1}{2}$	$-z,\ x+\frac{1}{2},\ -y+\frac{1}{2}$
			$y,\ z,\ x$	$-y,\ z+\frac{1}{2},\ -x+\frac{1}{2}$
			$y+\frac{1}{2},\ -z+\frac{1}{2},\ -x$	$-y+\frac{1}{2},\ -z,\ x+\frac{1}{2}$
			$y+\frac{1}{4},\ x+\frac{3}{4},\ -z+\frac{3}{4}$	$-y+\frac{1}{4},\ -x+\frac{1}{4},\ -z+\frac{1}{4}$
			$y+\frac{3}{4},\ -x+\frac{3}{4},\ z+\frac{1}{4}$	$-y+\frac{3}{4},\ x+\frac{1}{4},\ z+\frac{3}{4}$
			$x+\frac{1}{4},\ z+\frac{3}{4},\ -y+\frac{3}{4}$	$-x+\frac{3}{4},\ z+\frac{1}{4},\ y+\frac{3}{4}$
			$-x+\frac{1}{4},\ -z+\frac{1}{4},\ -y+\frac{1}{4}$	$x+\frac{3}{4},\ -z+\frac{3}{4},\ y+\frac{1}{4}$
			$z+\frac{1}{4},\ y+\frac{3}{4},\ -x+\frac{3}{4}$	$z+\frac{3}{4},\ -y+\frac{3}{4},\ x+\frac{1}{4}$
			$-z+\frac{3}{4},\ y+\frac{1}{4},\ x+\frac{3}{4}$	$-z+\frac{1}{4},\ -y+\frac{1}{4},\ -x+\frac{1}{4}$

Table 2.2: Occupied equivalent sites of the $P4_332$ space group in one primitive cell are shown.

sample become ordered at low temperatures (below 735 °C) in such a way that rows of octahedral sites in [110] directions are occupied by regularly alternating sequence of lithium and iron atoms in ratio 1:3. Such ordering means that all six nearest octahedral sites to each lithium ion are occupied by iron ions while each iron atom in the octahedral site is surrounded by two lithium atoms and four octahedral iron atoms. The crystal remains cubic, however, symmetry reduces to space group $P4_332$ (O^6) and also the local symmetries of cationic sites are lowered (Table 2.2). This work is concerned with ordered lithium ferrite only.

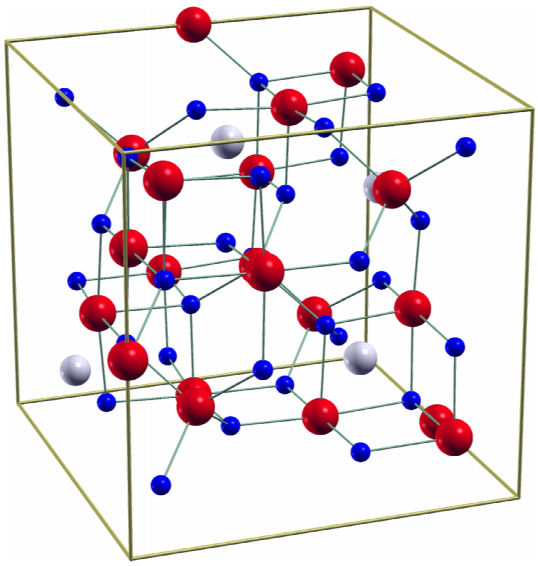

Figure 2.2: Simple cubic conventional unit cell of ordered lithium ferrite, $(Fe_8)[Li_4Fe_{12}]O_{32}$ in $P4_332$ space group. Iron atoms are red, oxygens are blue and lithium ions are gray. Created using XCrysDen [10].

The structure of lithium ferrite is completely inverted* and the valence states can be represented by formula $Fe^{3+}[Li^{+}_{0.5}Fe^{3+}_{1.5}]O^{2-}_{4}$. In contrast to e.g. manganese ferrites, the preferences of cations and their valence states do not depend on heat treatment, the crystal and magnetic structure of lithium spinel are very regular and stable. The fact that no cation can change its valence state easily together with high cationic order leads to relatively low electrical conductivity of lithium ferrite [25]. The magnetic properties are governed by a presence of ferric ions as the only type of magnetic ions. As Fe^{3+} has electron configuration ^{6}S, the theoretical value of magnetic moment per formula unit for collinear magnetic structure is 2.5 μ_B, which is in good agreement with experimental values [26].

2.5.2 ^{57}Fe NMR in Ordered Lithium Ferrite

There are some older papers on ordered lithium ferrite where ^{57}Fe NMR spectra were recorded [27, 28, 29]. Frequency anisotropy of ^{57}Fe NMR spectra at both tetrahedral and octahedral sites was investigated experimentally in [30]. The magnetic easy axis of lithium ferrite is in $\langle 111 \rangle$ direction.

*Strictly speaking, the inversion was defined for ratio of cations 1:2. In this case, we want to imply, that all Li atoms occypy B sites.

2.6 Magnetite

Magnetite Fe_3O_4 is one of the earliest discovered magnets and one of the best known magnetic compounds. With its interesting collective interplay among charge, orbital, lattice, and magnetic electronic orderings, magnetite belongs to class of compounds called Mott insulators. Despite the effort devoted to study of magnetite in the last 70 years, the physics of magnetite and in particular the question of its electronic structure is still an open problem of the solid state physics.

2.6.1 Structure of Magnetite

Magnetite is of special interest due to the Verwey phase transition, a metal-insulator transition, which occurs at a temperature $T_V \sim 120$–125 K, depending on the sample purity. The most pronounced effect of Verwey transition is an abrupt change of electric conductivity by two orders of magnitude together with a change of crystal symmetry from cubic $Fd\bar{3}m$ to monoclinic Cc (below T_V). Besides the Verwey transition, magnetite also undergoes a spin reorientation transition at temperature T_R (~ 130 K for stoichiometric magnetite [31]), at which the easy axis of magnetization changes from $\langle 100 \rangle$ below T_R to $\langle 111 \rangle$ above T_R.

The low-temperature structure is formed from the cubic unit cell with lattice parameter a as $\sqrt{2}a \times \sqrt{2}a \times 2a$ crystallographic supercell with space group Cc. The unit cell countains sixteen tetrahedral A sites (eight crystallographically non-equivalent sorts) and thrity-two octahedral B sites (sixteen crystallographically non-equivalent sorts), each nonequivalent sort consists of two atoms per unit cell. Such structure was identified by a neutron-diffraction study of a partially detwinned single crystal [32] and confirmed by ^{57}Fe NMR experiments that provide high sensitivity with respect to differences of particular site surroundings [31, 33].

Wright *et al.* [34] studied the low temperature structure by means of neutron powder and x-ray experiments and observed numerous superstructure peaks which were identified by comparing the results above and below T_V and attributed to the monoclinic unit cell with Cc symmetry. Despite numerous efforts and attempts in the past to refine the low-temperature structure, only an approximate structure in a smaller unit cell has been completely refined. Wright *et al.* found monoclinic P2/c symmetry cell with orthorhombic Pmca pseudosymmetry constraints on the atomic positions to give the best agreement with experiment. The P2/c unit cell has 1/4 volume

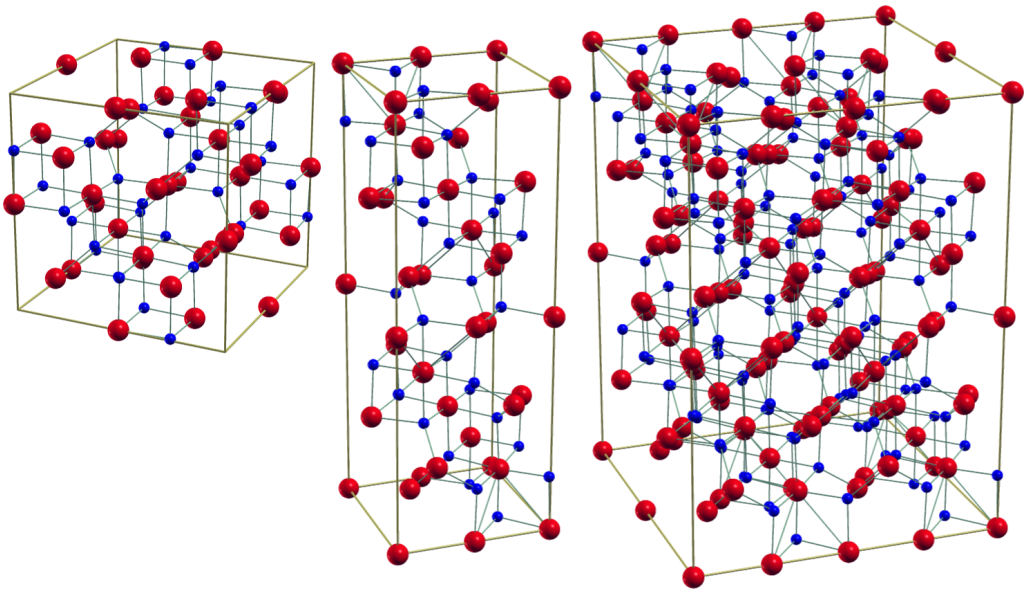

Figure 2.3: High temperature conventional face centered cubic unit cell of magnetite $(Fe_8)[Fe_{16}]O_{32}$ in $Fd\bar{3}m$ space group (left) is compared with low temperature monoclinic base-centered structure $(Fe_8)[Fe_{16}]O_{32}$ in P2/c space group (center) and low temperature monoclinic base-centered structure $(Fe_{32})[Fe_{64}]O_{128}$ in Cc space group (right). Monoclinic cells are rotated 45° around the vertical axis to coincide with the cubic structure on left. Iron atoms are red and oxygens are blue. Created using XCrysDen [10].

compared to Cc, corresponding to $\frac{1}{\sqrt{2}}a \times \frac{1}{\sqrt{2}}a \times 2a$ cell. The difficulties are a consequence of a tremendous complexity of the magnetite low temperature structure, as the monoclinic and pseudo-rhombohedral distortions are very subtle.

Magnetite is a mixed valence compound with completely inverse spinel structure. The tetrahedral sites are occupied by ferric ions, and thus the excess charge is manifested in the octahedral sites. The valence states then may be formally pictured as $(Fe^{3+})[Fe^{2+}Fe^{3+}]O_4^{2-}$. However, controversies with the charge ordering in magnetite and also in other oxides with mixed valency, e.g [35, 34, 36], suggest that such concept of well defined Fe^{2+} and Fe^{3+} ions in the octahedral sites should be reconsidered and that a fractional ionicity may be standard in this class of materials. Above the temperature of the Verwey transition, T_V, the averaged valency of octahedral iron is rather $Fe^{2.5+}$. However, below T_V non-integer numbers characterizing different valences of particular non-equivalent iron positions (e.g. due to a "charge wave") should be used; for example the simplest differentiation of octahedral

valences would yield a formula $(Fe^{3+})[Fe^{(2.5-\delta)+}Fe^{(2.5+\delta)+}]O_4^{2-}$.

2.6.2 Magnetic Properties of Magnetite

Besides the jump in the electronic conductivity at T_V, several magnetic features occur, e.g. a drop in the spontaneous magnetization well above T_V, a negative maximum of the magnetocaloric effect, anomalies in the magnetoresistance in the close vicinity of T_V, and the different dependence on magnetic field during low temperature cooling. As was already mentioned, just above the Verwey temperature the reorientation transition appears (at $T_R \sim 130$ K). The easy axis of magnetization turns its direction from $\langle 111 \rangle$ at high teperature to $\langle 100 \rangle$ at low temperature. After a long debate, it has been recognized that T_V and T_R are distinct temperatures [37, 38].

2.6.3 ^{57}Fe NMR in Magnetite

In the literature [31, 39] ^{57}Fe NMR spectra of magnetite in dependence on temperature are published. Whereas above T_V the symmetry of magnetite crystal structure is cubic and the NMR spectrum is simple, below T_V the spectrum becomes more complex due to lowered crystal symmetry. It was shown that the spectrum measured in zero external magnetic field at temperatures below T_V is in accordance with Cc space group. It consists of eight lines assigned to eight crystallographically non-equivalent tetrahedral A sites and sixteen lines from sixteen crystallographically non-equivalent octahedral B sites [31, 33, 39]. Spectra measured in external magnetic field display frequency shifts and line splitting as an effect of magnetic non-equivalency of iron sites and anisotropy of hyperfine interaction.

2.6.4 Magnetic Axis Switching in Magnetite

Switching of magnetic easy axis is a phenomenon related to the Verwey transition and the low symmetry phase of magnetite Fe_3O_4. Since the structure changes at T_V, each of high temperature cubic $\langle 100 \rangle$ directions may become the low temperature monoclinic c axis, doubled in comparison to the cubic lattice constant. As a result, the material breaks into several structural domains. When an external magnetic field $B \sim 0.2$ T is applied along particular $\langle 001 \rangle$ direction while cooling through the transition, this direction will then become both the unique c axis and also the magnetic easy axis. Intermediate and hard magnetic axes, b and a, then correspond to $\langle 110 \rangle$

directions of high temperature cubic cell. If now magnetite sample is magnetized along another direction of $\langle 001 \rangle$ type at temperatures lower than T_V, a reorientation of magnetic moments, i.e. easy axis switching, may take place and this direction becomes a new easy axis. This was observed at temperatures higher than $\sim$ 50 K [40, 41]. It was recently proved [42, 43] that also crystallographic c axis is forced to this particular direction, i.e. the manipulation of structure is possible by the magnetic field.

Although the axis switching phenomenon was studied by various approaches, the hyperfine methods, namely NMR, have not been employed. The former NMR measurements of magnetite in external magnetic field were performed at temperatures too low to allow observation of axis switching. NMR spectroscopy can easily see all different iron positions, allowing potentially a precise observation of the axis switching phenomenon.

2.6.5 Magnetite with Cationic Vacancies

Introducing a small number of cation vacancies into the magnetite structure raises an interesting question how the valence changes and whether some charge is localized near the iron vacancy. It has been observed that the cation vacancy appears on the octahedral sites [44]. Likewise the stoichiometric compound, the magnetite with small concentration of cation vacancies, $Fe_{3(1-\delta)}O_4$ undergoes a phase transition at Verwey temperature, where the crystal structure changes from cubic to monoclinic. For stoichiometric magnetite T_V is approximately 125 K and it decreases rapidly when the vacancy concentration increases [45].

Chapter 3

NMR in Magnetically Ordered Materials

The nuclear magnetic resonance (NMR) was used as the experimental approach in this work. Some basic principles of NMR spectroscopy are treated in the following chapter, especially the issues that are closely connected with subjects presented in chapters 7, 8, and 9. More detailed description may be found in many textbooks concerning NMR, e.g. [46, 47, 48, 49].

3.1 Nuclear Moments

Hyperfine interactions are described by terms of a multipole expansion of electromagnetic interaction of atomic nucleus with surrounding particles. From the viewpoint of NMR, there are two terms beyond the Coulomb electric interaction of nuclear and electron charges that are important contributions to the energy of the nucleus (given by Hamiltonian H). The magnetic dipolar interaction (H_m) and electric quadrupolar interaction (H_Q):

$$H = H_m + H_Q \tag{3.1}$$

Two properties of the nucleus are connected to H_m and H_Q, the nuclear magnetic dipolar moment and nuclear electric quadrupolar moment, respectively. Nuclear magnetic moment ($\boldsymbol{\mu}$) is closely linked to the nuclear spin $\mathbf{I}$ via gyromagnetic ratio

$$\boldsymbol{\mu} = \gamma \mathbf{I}, \tag{3.2}$$

and interacts with the surrounding magnetic field **B**:

$$H_m = -\boldsymbol{\mu} \cdot \mathbf{B} \tag{3.3}$$

Apparently, only nuclei with nonzero nuclear spin interact with the magnetic field.

Electric interaction relevant to NMR, is the electric quadrupolar interaction, i.e. the interaction of nuclear electric quadrupole momentum **Q** with the gradient of electric field **E**:

$$H_Q = \frac{e}{6}\mathbf{Q}\nabla\mathbf{E}. \tag{3.4}$$

Properties of tensor **Q** allow to describe it with one scalar component, Q. Tensor of electric field gradient is defined as $\mathbf{V} = \nabla\mathbf{E} - \mathbf{1}\,\frac{1}{3}\mathrm{Tr}(\nabla\mathbf{E})$ to have zero trace. While it has three eigenvalues V_{ii}, $|V_{zz}| \geq |V_{yy}| \geq |V_{xx}|$, it is usually described by the component V_{zz} and the asymmetry $\eta = \frac{V_{yy}-V_{xx}}{V_{zz}}$. Quadrupolar interaction is non-zero only for nuclei with spin $I \geq 1$ and for local electric fields of lower than cubic symmetry.

3.2 Nuclear Magnetic Resonance

In dependence on nuclear properties ($\boldsymbol{\mu}$, Q) and on values and symmetries of magnetic and electric fields (**B**, **V**) acting on the nucleus, the energy level of nuclear ground state may split into two or more energy levels E_i. The large number of nuclei present in a matter may be considered as a statistical ensemble of N particles, that in equilibrium at temperature T occupy these split energy levels E_i according to Boltzmann statistics:

$$N(E_i) \approx \mathrm{e}^{-\frac{E_i}{kT}} \tag{3.5}$$

Differences in occupation of the energetic levels induce the polarization of nuclear spin system, which leads to macroscopic nuclear magnetization:

$$\mathbf{M}_n = \frac{N\gamma^2\hbar^2 I(I+1)}{3k_B T}\mathbf{B}, \tag{3.6}$$

$\mathbf{M}_n$ has equilibrium direction in the direction of **B**. When deviated from this direction, it performs precessional rotation around the direction of magnetic field **B** with Larmor frequency:

$$\boldsymbol{\omega} = -\gamma\mathbf{B}. \tag{3.7}$$

As the value and direction of $\mathbf{B}$ varies among particular nuclei and also fluctuates in time, there is a distribution Ω of Larmor frequencies in the ensemble of nuclear spins.

Inducing transitions between two energy levels (E_i, E_j) by a suitable external intervention changes the nuclear magnetization and brings the nuclear system out of the equilibrium. The change of magnetization $\mathbf{M}_n$ (described by longitudinal and transverse components, $\mathbf{M}_n^0$ and $\mathbf{M}_n^\perp$) can be induced by radio frequency (rf) magnetic field with frequency ω_{rf}, so that $\hbar\omega_{\mathrm{rf}}$ is sufficiently close to the energetic difference $E_i - E_j$.

In practice, the rf field is produced in pulses, by an appropriate rf voltage in rf coil: rf pulse of suitable length and phase can manipulate the magnetization $\mathbf{M}_n$ out of its equilibrium direction. If the magnetization is moved out of its equilibrium direction, it performs precessional movement around the direction of $\mathbf{B}$, characterized by the Larmor frequencies of nuclei in distribution Ω. As a consequence, the transverse component $\mathbf{M}_n^\perp$ rotates around the direction of $\mathbf{B}$ and induces oscillating electric current in the rf coil.

The nuclear magnetization undergoes relaxation processes that arise from interactions of the nuclear spins with surroundings. First process, the spin-lattice relaxation (T_1), concerns the longitudinal component of nuclear magnetization ($\mathbf{M}_n^0$) lying in the direction of field $\mathbf{B}$ and is connected with dissipation of energy from the nuclear system. Second process, the spin-spin relaxation (T_2), is related to the transverse component ($\mathbf{M}_n^\perp$) that is perpendicular to $\mathbf{B}$ and is induced by random processes. Additionally, inhomogeneities of $\mathbf{B}$ in the volume of sample lead to changes of $\mathbf{M}_n^\perp$ characterized approximately by rate $T_{2\mathrm{N}}$. The relaxation of $\mathbf{M}_n^\perp$ is then faster, characterized by T_2^*, $\frac{1}{T_2^*} = \frac{1}{T_2} + \frac{1}{T_{2\mathrm{N}}}$.

After the rf pulse, distribution of precession frequencies disperses (T_2^*), effectively reducing the net transverse magnetization $\mathbf{M}_n^\perp$, which also reduces the induced signal (Free Induction Decay). Simultaneously, due to spin-lattice relaxation, the magnetization $\mathbf{M}_n$ gradually returns to its equilibrium.

In strongly correlated systems, $\mathbf{M}_n^\perp$ may decay rapidly, which essentially disallows measurement of NMR signal, as it comes directly after the strong excitation pulse. Therefore, spin echo method is widely used, consisting of at least two pulses, e.g. $\frac{\pi}{2}$-pulse and π-pulse separated by a delay τ. First pulse rotates the nuclear magnetization into the plane perpendicular to the equilibrium direction (i.e. it maximizes $\mathbf{M}_n^\perp$ and minimizes $\mathbf{M}_n^0$), where loss of $\mathbf{M}_n^\perp$ occurs due to T_2^* relaxation. However, non-zero nuclear

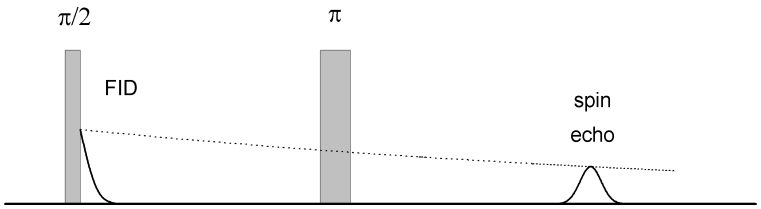

Figure 3.1: Basic pulse sequence producing a spin echo. The Free Induction Decay (FID) after the first pulse is usually unobservable because of the rapid T_2^* relaxation. NMR signal is then obtained from the spin echo, separately formed after the second pulse.

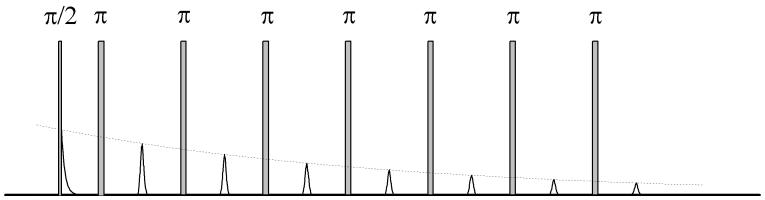

Figure 3.2: An example of multi-pulse Carr-Purcell sequence. The individual echoes may be coherently summed to increase the NMR signal, however, their amplitude decays with spin-spin relaxation (T_2).

magnetization still remains in the perpendicular plane, if the T_1 and T_2 relaxation mechanisms are slow enough ($\tau \ll T_1, T_2$). Then after a time τ the π-pulse is applied, which acts essentially as a time reversal on the phases in the distribution Ω. After another time τ, the coherence is restored in a spin echo (Fig. 3.1). In principle, it is possible to apply additional π-pulses in order to produce more spin echoes, in a form of Carr-Purcell sequence (Fig. 3.2). The number of observed spin echoes is limited by T_2 relaxation.

The measured NMR time domain signal is Fourier transformed in order to acquire the NMR spectrum. Frequencies of the spectra lines correspond to the Larmor frequencies of the resonating nuclei, and thus reflect the values of local magnetic field. The intensity of NMR line is proportional to the number of resonating nuclei.

3.3 Hyperfine Magnetic Field

In magnetic materials, spin and orbital moments of unpaired electrons ($\hat{\mathbf{s}}$, $\hat{\mathbf{l}}$), create hyperfine magnetic field $\mathbf{B}_{\mathrm{hf}}$ at the position of the nucleus:

$$\hat{\mathbf{B}}_{\mathrm{hf}} = -\frac{\mu_0 \mu_B}{2\pi} \sum_i \left(\frac{\hat{\mathbf{s}}_i}{r^3} - \frac{3\mathbf{r}(\hat{\mathbf{s}}_i \cdot \mathbf{r})}{r^5} + \frac{\hat{\mathbf{l}}_i}{r^3} + \frac{8\pi}{3} \hat{\mathbf{s}}_i \delta(\mathbf{r}) \right). \tag{3.8}$$

The first two terms arise from dipolar interaction with electron spins, $B_{\mathrm{hf}}^{\mathrm{dip}}$, third term originates in orbital motion of electrons, $B_{\mathrm{hf}}^{\mathrm{orb}}$, and the last term, Fermi contact interaction, is due to overlap of the wave function of nucleus electrons at the position of the nucleus (mostly s electrons). In atoms with unpaired electron spins, where the spatial wave functions of s electrons are polarized via interaction with unpaired d electrons, the Fermi contact interaction is dominant contribution to $\mathbf{B}_{\mathrm{hf}}$. Dipolar and orbital terms in transition metal compounds are usually smaller than the contact term, since the orbital moments of $3d$ electrons are quenched by the crystal field. For cubic site symmetry, which may be e.g. in tetrahedral spinel sites, the dipolar term is zero. The hyperfine field is inhomogeneous and fluctuating, however, its time-averaged value is nonzero in magnetic materials, and thus may represent the magnetic field in equation 3.3.

The presence of strong hyperfine magnetic field (eq. 3.8) is the fundamental aspect in application of NMR spectroscopy to studying the magnetic materials. The time-averaged value of hyperfine field is high, typically it is in the order of tens of Tesla for nuclei in magnetic atoms (those with unpaired d or f electrons). The spin polarization is mediated by the electrons from magnetic atoms to the other atoms, and as a consequence, transferred hyperfine field of lower magnitude appears also on nuclei of non-magnetic atoms. This enables to detect NMR signal on various isotopes in a given compound.

The hyperfine field arises due to strong interaction of electron moments with the spin of nucleus, which implies several consequences:

- The value of hyperfine field is immensely sensitive to the local electron structure.
- The NMR spectra are wide in frequency scale; even for a spectrum of a single isotope.
- The resonance lines display considerable inhomogeneous broadening.

- Alternating part of the local magnetic field enhances significantly the action of rf field on the nuclei, as well as the response of nuclear magnetization. The enhancement differs for nuclei in magnetic domains from those in magnetic domain walls.
- The resonance frequency depends on temperature, approximately following the temperature dependence of electron magnetization. (Provided, e.g. no phase transition occurs.)

For the purpose of studying the magnetic materials, NMR spectroscopy is well suited to investigate crystal structure, especially its local character. In the first place, resonating nuclei in a particular crystal site produce distinct subspectrum, that reflects the local symmetry of that site. Therefore, it is possible to observe NMR signal from different crystal sublattices separately. Moreover, when the local electronic structure surrounding the resonating nucleus is somehow perturbed, the value of hyperfine field changes, compared to unperturbed surrounding. As a consequence, a satellite line emerges in the vicinity of the spectral line. Source of such perturbation may be, e.g. a substitution of neighbouring cation with a different one, a change of its valence or spin state, displacement from its equilibrium position, etc.

3.3.1 Hyperfine Field and Electron Magnetization

As the value and direction of hyperfine field corresponds to value and direction of the atomic magnetic moment, the NMR spectroscopy is further applicable to examining the magnetic structure in a magnetic material. The temperature dependence of NMR spectrum may be exploited for studying the exchange interactions, and measurements in external magnetic field provide valuable additional information on the magnetic structure. The latter approach is discussed in the following text.

The hyperfine interaction may be anisotropic, and thus depend markedly on the direction of electron magnetization. The dependence of hyperfine field $B_{\mathrm{hf}}(\mathbf{n})$ on the direction of electron magnetization $\mathbf{n}$ may be approximated by power series up to quadratic term (in components of $\mathbf{n}$):

$$B_{\mathrm{hf}} = B_{\mathrm{iso}} + \mathbf{n} \cdot \mathbf{A} \cdot \mathbf{n}. \tag{3.9}$$

B_{iso} denotes the isotropic part of B_{hf}, and $\mathbf{A}$ is a second rank traceless symmetric tensor, which in general has five independent components. The number of independent components decreases when additional relations be-

tween the components arise from local symmetry of the crystallographic position of the resonating nucleus.

The matrix of tensor $\mathbf{A}$ of a given site can be expressed in coordinate system of the crystallographic unit cell. However, such tensor expression represents just one particular position of crystallographically equivalent sites. In order to involve all other equivalent sites in the unit cell into our consideration, their respective tensors $\mathbf{A}^{(i)}$ have to be generated by relations

$$\mathbf{A}^{(i)} = \mathbf{G}^{(i)} \cdot \mathbf{A} \cdot (\mathbf{G}^{(i)})^{-1}, \tag{3.10}$$

where $\mathbf{G}^{(i)}$ formally denote the unitary matrices representing a crystallographic point group symmetries that are associated with the space group of the given crystal structure. Such process yields a set of k different tensors for a given type of crystallographic site, $\mathbf{A}^{(1)}, \ldots, \mathbf{A}^{(k)}$. (Detailed derivation is given in [50].)

Now one can evaluate the anisotropic contributions to the hyperfine field by substituting these generated tensors into the equation (3.9). Such process yields a set of k dependences, given by equations:

$$B^{(i)} = B_{\text{iso}} + \mathbf{n} \cdot \mathbf{A}^{(i)} \cdot \mathbf{n}. \tag{3.11}$$

These equations may then be used for description of experimental or calculated data in order to obtain the components of tensor $\mathbf{A}$.

A degeneracy is usually present in NMR spectra measured in zero external magnetic field, as the easy axis of magnetization lies in a direction with high symmetry. When the dependence of $B^{(i)}$ on directions $\mathbf{n}$ in a given plane forced by external magnetic field is studied (i.e. angular dependence), some of the dependences given by equations (3.11) may coincide, and as a consequence, the number of individual branches in the angular dependence of NMR spectrum is lower than k. For complicated systems, where the number of branches is high, the NMR spectra have to be measured in dependence on the direction of external magnetic field to obtain the tensor $\mathbf{A}$.

An example of anisotropy of resonance frequency may be given on octahedral sites in manganese ferrite. For the octahedral B site with trigonal axial symmetry, only one parameter is sufficient to describe the tensor $\mathbf{A}$, and consequently, the angular dependence of frequency f has a form:

$$f = \beta(3\cos^2\theta - 1), \tag{3.12}$$

where θ is the angle between the direction of electron magnetization and the local trigonal axis, parameter β is related to the eigenvalues of tensor

A. In B site of the spinel structure the trigonal symmetry axis is along one of the four $\langle 111 \rangle$ directions. For the easy axis of magnetization lying e.g. in [111] direction, the iron nuclei in B sites with trigonal axis in [111] become magnetically nonequivalent with the remaining octahedral nuclei (that have trigonal axis directions $[\bar{1}11]$, $[1\bar{1}1]$, or $[11\bar{1}]$). Therefore, two resonant lines (B_1 and B_2) appear with ratio of integral intensities $1 : 3$.

If the electron magnetization was in direction [100] (e.g. forced by an applied external magnetic field), all four types of B sites would be magnetically equivalent. As a consequence, there would be a single B line in the NMR spectrum.

Chapter 4

Calculations of Electronic Properties

Nuclear magnetic resonance is a powerful tool capable of providing information on local crystallographic and magnetic properties that are difficult to obtain by other experimental methods. The lack of complementary experimental approach or insufficient resolution of such methods may raise problems, especially in complicated magnetic systems where interpretation of NMR spectra is troublesome or even not available so far. However, such valuable support can be granted by theoretical methods of calculating the crystal properties from the first principles which have been developing rapidly in past decades.

4.1 Calculation Method

Density Functional Theory (DFT) belongs to modern and widely used methods to perform calculations of electronic structure of solids. It postulates that the total energy E_{tot} of the ground state is a functional of electron density $\rho(\mathbf{r})$ and that such functional takes its minimum for electron density of the ground state. Considering the adiabatic approximation, the functional of total energy of the ground state has a form:

$$E_{\mathrm{tot}}[\rho] = T_{\mathrm{s}}[\rho] + E_{\mathrm{N-e}}[\rho] + E_{\mathrm{e-e}}[\rho] + E_{\mathrm{N-N}} + E_{\mathrm{xc}}[\rho], \tag{4.1}$$

where T_{s} is kinetic energy of non-interacting electrons, $E_{\mathrm{N-e}}$ means Coulomb interaction of nuclei and electrons, $E_{\mathrm{e-e}}$ denotes Coulomb repulsion of elec-

trons in the mean field approximation, $E_{\mathrm{N-N}}$ stands for repulsive Coulomb interaction of the fixed nuclei, and E_{xc} is the exchange-correlation energy. All terms except E_{xc} can be well described, however, to handle the exchange-correlation term E_{xc} it is essential to employ a suitable approximation. Currently used possibilities are based either on Local Spin Density Approximation (LSDA) or Generalized Gradient Approximation (GGA).

LSDA assumes that E_{xc} can be expressed by local exchange-correlation energy density μ_{xc} and electron density $\rho(\mathbf{r})$ in a form:

$$E_{\mathrm{xc}} = \int \mu_{\mathrm{xc}}\, \rho(\mathbf{r})\, \mathrm{d}\mathbf{r} \tag{4.2}$$

and approximates the form of density μ_{xc}. GGA appropriately adds gradient terms to electron density, or even adds kinetic energy density to the exchange-correlation energy.

Applying variational principle to minimize the total energy functional $E_{\mathrm{tot}}[\rho]$ yields Kohn-Sham equation:

$$(-\Delta + V_{\mathrm{N-e}} + V_{\mathrm{e-e}} + V_{\mathrm{N-N}} + V_{\mathrm{xc}})\psi_i(\mathbf{r}) = \varepsilon_i \psi_i(\mathbf{r}). \tag{4.3}$$

This equation has to be solved in self-consistent iterative cycle, because the potentials on the left side of the equation are functions of electron density $\rho(\mathbf{r})$ which depends on the calculated Kohn-Sham wave functions $\psi_i(\mathbf{r})$ and their occupation numbers n_i:

$$\rho(\mathbf{r}) = \sum_i n_i |\psi_i(\mathbf{r})|^2. \tag{4.4}$$

In order to properly describe magnetic materials one has to perform spin-polarized calculation, and thus to consider electron density consisting of two components. The calculations are then carried out separately for density of electrons with the spin 'up', $\rho^{\mathrm{UP}}(\mathbf{r})$ and with the spin 'down', $\rho^{\mathrm{DN}}(\mathbf{r})$.

The Linearized Augmented Plane Wave method (LAPW) is one of the most accurate approaches to solve the Kohn-Sham equations in order to gain the ground state density, total energy, and energy bands. The solutions of Kohn-Sham equations are expanded into a set of basis functions $\phi_{\mathbf{k}_n}$:

$$\psi_{\mathbf{k}}(\mathbf{r}) = \sum_n c_n \phi_{\mathbf{k}_n}. \tag{4.5}$$

The space of unit cell is divided into non-overlapping atomic spheres centred at the atomic sites and interstitial region. Inside the atomic spheres, basis

functions $\phi_{\mathbf{k}_n}$ have the form of atomic-like wave functions:

$$\phi_{\mathbf{k}_n} = \sum_{lm} (A_{lm,\,\mathbf{k}_n} u_l(r, E_l) + B_{lm,\,\mathbf{k}_n} \dot{u}_l(r, E_l)) Y_{lm}(\mathbf{r}), \tag{4.6}$$

while in the interstitial space the functions are expanded by plane waves:

$$\phi_{\mathbf{k}_n} = \frac{1}{\sqrt{\omega}} \mathrm{e}^{i\mathbf{k}_n \cdot \mathbf{r}} \tag{4.7}$$

where $\mathbf{k}_n = \mathbf{k} + \mathbf{K}_n$, $\mathbf{K}_n$ are the reciprocal lattice vectors and $\mathbf{k}$ is the wave vector inside the first Brillouin zone. $u_l(r, E_l)$ is the regular solution of radial Schrödinger equation for energy E_l and $\dot{u}_l(r, E_l)$ is its derivative at the same energy E_l. In order to improve the linearization and to allow a consistent treatment of semicore and valence states in one energy window, additional basis functions, local orbitals (LO), are added [51]:

$$\phi^{\mathrm{LO}}_{\mathbf{k}_n} = \sum_{lm} (A_{lm,\,\mathbf{k}_n} u_l(r, E_{1,l}) + B_{lm,\,\mathbf{k}_n} \dot{u}_l(r, E_{1,l}) + C_{lm,\,\mathbf{k}_n} u_l(r, E_{2,l})) Y_{lm}(\mathbf{r}). \tag{4.8}$$

These LO consist of a linear combination of two radial functions at two different energies (E_1, E_2) and one energy derivative (at one of these energies). The coefficients A_{lm}, B_{lm} and C_{lm} are determined by the requirements that ϕ^{LO} should fulfil the continuity conditions at the interface of atomic spheres and interstitial region.

However, the standard LAPW method with such constraints on the planewaves is not the most efficient way to linearize the APW method [52]. More efficiently, one can use the standard APW basis with $u_l(r, E_l)$ at a fixed energy E_l (in order to keep the eigenvalue problem linear) and add a new local orbital (lo):

$$\phi_{\mathbf{k}_n} = \sum_{lm} (A_{lm,\mathbf{k}_n} u_l(r, E_l)) Y_{lm}(\mathbf{r}), \tag{4.9}$$

$$\phi^{\mathrm{lo}}_{lm} = (A_{lm} u_l(r, E_{1,l}) + B_{lm} \dot{u}_l(r, E_{1,l})) Y_{lm}(\mathbf{r}). \tag{4.10}$$

In this new lo (different from LO in eq. 4.8) the A_{lm} and B_{lm} do not depend on $\mathbf{k}_n$, and are determined by the requirement that ϕ^{lo} is zero at the sphere boundary and is normalized. Such scheme allows to reduce the basis, and therefore greatly reduces the computational time.

Both methods outlined above, LAPW and APW+lo, are implemented in the program package WIEN2k [53], which thus combines the efficiency of APW with convenience of LAPW. WIEN2k was used for calculations of electronic structure in this work.

Besides the capabilities to calculate many different physical properties also various forms of LDA+U for treatment of localized electrons and strongly correlated systems are implemented. Best suited for strongly correlated systems studied in this work is the scheme introduced by Anisimov *et al.* [54] with an approximate correction for the self-interaction (SIC scheme).

4.2 Calculating Hyperfine Parameters and Interrelated Problems

Electron density calculated by WIEN2k allows to determine wide range of crystal properties and microscopic parameters from the first principles. The input comprises specification of the crystal structure (i.e. space group symmetry, cell parameters and atomic positions) and the electronic configurations of atoms. In the initialization procedure local point group symmetries and local rotation matrices are determined and the basis of atomic functions is generated, from which the initial atomic densities are calculated with chosen exchange-correlation potential. Finally the mesh of k-points is generated in the first Brillouin zone and a starting electron density is evaluated as a superposition of initial atomic densities. The number of k-points and the size of the basis are two fundamental parameters affecting the accuracy and time demands of the calculation.

The self-consistent iteration cycle (SCF) at first generates the potentials from electron density. Then the core and valence electrons are handled separately—core states and densities are calculated fully relativistically while valence states and densities are treated by means of LAPW/APW+lo methods. At the end of each cycle the core and valence densities are added together, normalized and mixed with the density of previous step or several steps in order to accomplish a stable convergence.

Principal quantities, relevant for analysis of NMR spectra, are the values of hyperfine magnetic fields on involved nuclei, and in case that also the electric quadrupolar interaction is considered, the components of electric field gradient (EFG) tensor. Besides these outputs, calculated electric charges and magnetic moments of particular ions are often helpful and valuable piece of information.

Despite the large potential of *ab initio* calculations to complement the NMR experiments, there are several downsides of LSDA-based approach when applied to the magnetic system. One of them, important to NMR, is that the contact hyperfine field on paramagnetic ions is systematically

underestimated by LSDA [55, 56, 57]. A good agreement between experimental and calculated hyperfine field may be observed when the contact field is dominated by the transferred hyperfine interaction [55, 58, 59, 60]. However, considerable discrepancies occur when the contact hyperfine field is predominately due to on-site contribution of s core states, which both LSDA and GGA describe inaccurately.

Chapter 5

Applied NMR Methods

5.1 Experimental Equipment

The NMR experiments included in this work were performed using the NMR spectrometer based on a commercial Bruker Avance high-resolution console, adapted for measurements of magnetic materials. The spectrometer, basically, consists of excitation section, that generates rf pulses of desired properties, and detection section, that allows coherent acquisition, summation and further processing of the NMR signal [61].

The spectrometer enables measuring frequency-swept NMR spectra in range 6–600 MHz, which is sufficient for most of the transition metal compounds (e.g. ^{57}Fe NMR spectra range up to $\sim$ 80 MHz). As the NMR spectra of these compounds are broad, our experiment proceeded by sweeping the frequency region with a fixed step. For measuring the NMR spectra in this work frequency steps in range 30–60 kHz were used, and the resulting NMR spectrum were obtained as an envelope of the individual steps (example in Fig. 5.1).

A special attention to spectrometer sensitivity has to be paid, when measuring ^{57}Fe NMR spectra. Isotope ^{57}Fe has exceptionally low sensitivity (given by magnetogyric factor) and low natural abundance, compared to nuclei of some other transition metals (Table 5.1). The content of ^{57}Fe isotope was natural in all studied samples. On the other hand, NMR of ^{57}Fe may benefit from its low spin, which leads to less complicated spectra, undisturbed by the electric quadrupole interaction.

For broadband NMR experiments, it was necessary for the NMR probe

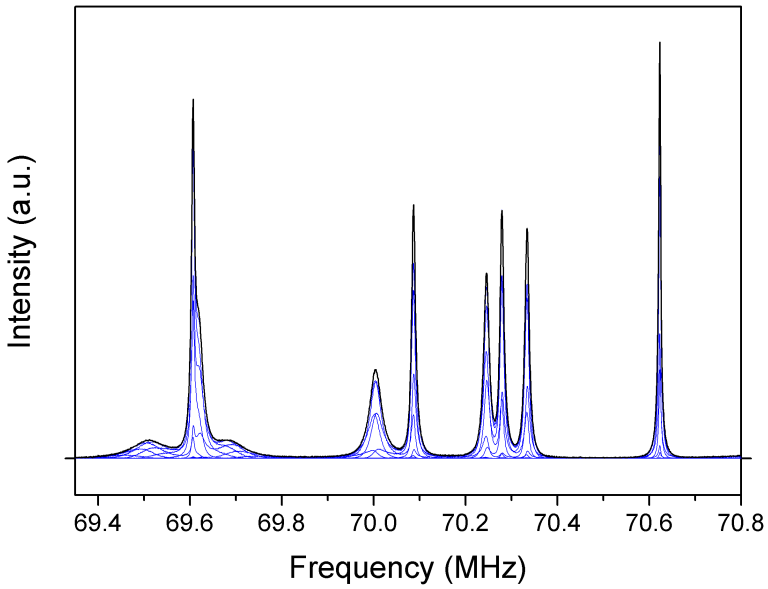

Figure 5.1: The NMR spectrum is obtained as an envelope of individual Fourier transforms at different excitation frequencies.

isotope	spin	γ (MHz/T)	Q (10^{-28} m^2)	natural abundance
^{47}Ti	5/2	2.404	30.2	7.4%
^{49}Ti	7/2	2.405	24.7	5.4%
^{51}V	7/2	11.21	−5.2	99.8%
^{53}Cr	3/2	−2.412	−15.0	9.5%
^{55}Mn	5/2	10.58	0.33	100.0%
^{57}Fe	1/2	1.382	–	2.2%
^{59}Co	7/2	10.08	0.42	100.0%
^{61}Ni	3/2	−3.811	0.16	1.1%
^{63}Cu	3/2	11.32	−0.22	69.2%
^{65}Cu	3/2	12.10	−0.20	30.8%

Table 5.1: NMR properties of selected nuclei of 3d transition elements in ground state. γ stands for magnetogyric ratio, Q denotes quadrupolar moment.

to allow measurement within the whole spectral range. Therefore, the measured sample was positioned into rf coil in homemade NMR probe with damped frequency characteristics to maintain comparable sensitivity in the entire NMR spectrum. For samples demanding high intensity of rf pulses, a probe with a resonant circuit was used, where the circuit impedance was matched by a tunable capacitor to the amplifier output and receiver input.

The used NMR probes can operate in wide temperature ranges, starting from helium temperatures. Variable temperature, e.g. for measurement of temperature dependence, was supplied by continuous flow helium cryostats, allowing to precisely maintain a given temperature during the NMR experiment via a temperature sensor positioned close to the sample.

The external magnetic fields, which are suitable for certain NMR experiments, were supplied by superconducting magnet with split solenoid that allows rotating the probe with respect to the direction of the magnet axis. Compared to the values of hyperfine fields, the applied magnetic fields are much weaker. When the direction of external magnetic field is parallel or anti-parallel to the electron magnetization, only the isotropic parts of hyperfine field change—the spectral lines shift to lower or higher frequencies. For other directions, magnetocrystalline anisotropy determines the changes of magnetization; in any case, also the anisotropy of hyperfine interaction starts to play an important role.

5.2 Applied Procedures

In order to acquire reliable NMR spectra, preliminary measurements and adjustments at given temperature are required. To achieve optimal excitation of the NMR signal, the length and intensity of rf pulses were carefully set and verified at different frequencies, so that any undesired frequency dependence of excitation or detection was avoided.

Adjusting the parameters of rf pulses was also used to aim at specific type of nuclei in the sample, as e.g. the enhancement of rf field is fundamentally different in magnetic domains and magnetic domain walls. Additionally, at least rough estimate of relaxation rates was performed, to properly design the pulse sequence.

Lengths of used excitation pulses were usually 1–10 μs, with amplitudes up to ~ 150 V. Depending on T_2 relaxation times, there were typically 20–100 pulses in CPMG sequences, separated by delays 10–1000 μs. Repetition times between the scans (i.e. time between two consecutive CPMG series)

ranged from minimal times $\sim$ 10 ms up to tens of seconds, depending on T_1 relaxation times. Additional factors increasing minimal repetition times in some cases were the maximal allowed duty cycle of the rf pulse power amplifier, or avoiding such an excessive irradiation by the rf field that could cause undesirable heating of the measured sample.

Chapter 6

Processes Applied in the Calculations

This chapter describes practices that were adopted for all calculations and followed in the whole thesis. At first, a starting input structure was constructed, usually using the experimental data: space group, lattice constants and internal structural parameters. The radii of atomic spheres (muffin-tin radius, RMT) were typically set 1.8–2.0 a.u. for 3*d* ions and 1.4–1.6 a.u. for oxygens. (Rydberg atomic units are used in calculations; here 1 a.u. denotes the Bohr radius, $a_0 = 5.291772108 \times 10^{-11}$ m.) The actual values may have varied between different calculations, e.g. 1.8 a.u. for all irons in manganese ferrite calculations and 2.0 a.u. in magnetite. However, within one calculation of a given structure or for sake of comparison of two similar calculations, the RMT parameters were strictly held at the same value.

After compiling the structural input, the self-consistent calculation was performed employing GGA exchange-correlation potential of Perdew, Burke and Ernzerhof [62], starting with somewhat lower values of the most important parameters: number of k-points, RK_{max} and G_{max}. The number of k-points in the irreducible part of Brillouin zone denotes how dense or sparse the generated k-mesh will be. The more k-points the more divisions in each direction of the reciprocal unit cell are produced. The other two parameters influence how the Kohn-Sham wave functions, charge density and potential are expanded. The parameter RK_{max} is defined as $RMT_{min} \times K_{max}$, where RMT_{min} is the smallest of all atomic sphere radii and K_{max} is the magnitude of the largest k-vector in the plane wave expansion. RK_{max} thus determines where the plane wave expansion of the wave function is truncated in the

interstitial region, and so governs the number of used basis functions. Finally, parameter G_{max} denotes the maximum magnitude of k-vectors in the Fourier expansion of charge density and potential. It specifies where the Fourier expansion is truncated in the interstitial space.

Strongly correlated materials display behaviour that cannot be described effectively in terms of non-interacting electrons. To improve the description of localized electrons ($3d$ in our case), a well developed extension to local spin density approximation, LDA+U, is applied: self-interaction correction (SIC [54]). The method is controlled by two parameters, U and J, that represent the on-site coulombic repulsion ("Hubbard parameter") and Hund's exchange parameter ("Stoner parameter"). Typical values of these parameters are $U \sim 1 - 10$ eV and $J \sim 0.1 - 1$ eV. However, a single parameter $U_{\text{eff}} = U - J$ is usually used in full potential methods (and $J = 0$). In this work the SIC scheme was employed with the GGA potential.

Despite the undisputed benefits contributed by including the LDA+U method, the correction brings specific stumbling blocks at the same time. For instance, in case of cubic magnetite the ${}^5T_{2g}$ triplet ground state of B site iron (formal valence $Fe^{2.5+}$) is split into doublet and singlet due to the trigonal distortion of the octahedron. The splitting of ${}^5T_{2g}$ is small, however, the LDA+U method lowers the energy of the occupied states and increases the energy of the less occupied or empty states. As a consequence, the calculation reaches an insulating ground state corectly, but the splitting of ${}^5T_{2g}$ is amplified by LDA+U, leading to a large, physically incorrect, charge disproportionation of the B site iron atoms. Hence when using LDA+U, one has to pay an increased attention, as there exists a danger of stabilizing an incorrect ground state.

When the convergence of SCF iterative calculation with a given set of parameters (number of k-points, RK_{max}, G_{max}, ...) was reached, the results were inspected. At first, it was tested whether significant atomic forces were present, and if needed, procedures of optimizing the internal structural parameters and lattice parameters with respect to the total energy and atomic forces were performed. These procedures were repeated with the number of k-points, RK_{max} and G_{max} being gradually increased until such values were reached that the calculated quantities (e.g. magnetic moments) displayed no sensitivity to further improvement of these parameters. Typical number of k-points in the Brillouin zone reached during this process was $N_k \gtrsim 1000/n$, where n is the number of atoms in the unit cell. Final size of the basis function matrix usually was 100–120 basis functions per atom of the unit cell, which corresponds to values of parameter $RK_{max} \sim 7.0$. Limit

for charge density Fourier expansion was typically $G_{max} \sim 15\,Ry^{\frac{1}{2}}$.* For complicated calculations, i.e. supercell structures or large crystal cells with low symmetry, these steps were first completed for a small basic crystal cell and then repeated for a supercell or for a cell with lowered symmetry.

In calculations where a specific direction of magnetization was needed, the spin-orbit interaction (s-o) was introduced. Due to increased complexity of the s-o calculations, such cases were first treated without spin-orbit interaction, i.e. the internal parameters were minimized, lattice parameters optimized and the calculation fully converged, and s-o was enabled afterwards.

When introducing the spin-orbit interaction into a spin-polarized system, several events occur. First of all the spin-orbit interaction in magnetic system lowers the symmetry in most of the spacegroups. Only such symmetry operations are kept that either do not change the direction of magnetization (identity, inversion, rotations with the rotation axis parallel to magnetization), or invert it (mirror planes, but only in systems containing inversion). As the spin-orbital interaction couples spin-up and spin-down states, they are no longer separable and the number of eigenvalues doubles. Moreover, because the s-o interaction is diagonalized in the space of the scalar relativistic eigenstates, it is usually necessary to take more eigenstates into account. The overall intricacy of treating the spin-orbital interaction is further amplified since the Hamiltonian and overlap matrices in the s-o calculation are now always complex matrices, even for structures with inversion symmetry.

6.1 Calculating the Hyperfine Field

Although some corrections and improvements to LSDA methods regarding the calculation of the contact hyperfine field were developed [56, 63], they still do not provide sufficient accuracy that could be compared to NMR experiment. We performed calculations on the barium hexaferrite system to demonstrate this issue.

Despite the fact that barium hexaferrite (M-type) contains ferric ions in five non-equivalent crystal positions, it is a simple, experimentally well covered structure, and therefore, it can be used as a model structure to illustrate the disagreement of calculated and measured hyperfine fields. The

*Although G_{max} has the dimension of length^{-1}, G^2_{max} may be given in atomic units of energy, hence it is usually called 'energy cut-off' and represented by $Ry^{\frac{1}{2}}$.

	LDA+U		GGA+U				NMR
site	B_{Fermi}	B^{*}_{hf}	B_{Fermi}	B^{*}_{hf}	$B^{\mathrm{orb}}_{\mathrm{hf}}$(iso)	$B^{\mathrm{dip}}_{\mathrm{hf}}$(iso)	B_{hf}
2a	−36.7	−53.2	−37.6	−54.3	0.52	0.00	54.924
2b	−23.7	−39.7	−24.0	−40.2	0.72	0.03	42.781
$4f_{\mathrm{IV}}$	37.0	52.9	37.4	53.5	−0.77	0.00	52.762
$4f_{\mathrm{VI}}$	38.6	54.9	40.2	56.7	−0.58	0.00	55.542
12k	−31.1	−47.6	−32.2	−48.9	0.58	0.00	50.843

Table 6.1: Calculated Fermi contact hyperfine field (B_{Fermi}) and value of hyperfine field (B^{*}_{hf}) with a basic correction to Fermi contact term applied according to [56] are displayed. Experimental value of isotropic part of hyperfine field (B_{hf}) is also printed (from [64]). All values are in units of Tesla.

comparison of hyperfine fields, as calculated by WIEN2k code (i.e. not corrected) with LDA+U or GGA+U potentials, and the experimental values (by NMR) are given in Table 6.1. Not only the calculated fields are shifted to significantly lower values than the experimental ones, this shift is also non-uniform as e.g. 2a has lower value of hyperfine field than $4f_{\mathrm{IV}}$, contradictory to the experiment.

When a basic correction to contact hyperfine field is applied according to [56], i.e. adding $-4.2\,\mathrm{T}\times\mu$, where μ is the calculated magnetic moment of the atom (in units of μ_{B}), an improvement is reached: the huge discrepancy between calculated and experimental fields reduce, yet the differences in the order of percents remain. One should note that the total isotropic hyperfine magnetic field includes also respective isotropic parts of the magnetic dipolar interaction of the nuclear spin with the on-site spin of electrons ($B^{\mathrm{dip}}_{\mathrm{hf}}$) and orbital magnetic moments ($B^{\mathrm{orb}}_{\mathrm{hf}}$). These were calculated (with GGA); sum of their isotropic parts is below 1 T as can be seen in Table 6.1.

However, when pursuing complicated systems where the differences of hyperfine fields are much more subtle than in the case of barium hexaferrite, calculations burdened with substantial errors in contact fields would make even a qualitative comparison of hyperfine fields with experiment impossible. Therefore, the calculated hyperfine fields must be treated with caution, which in practice restricts reasonable application to two particular cases, described in the following text.

6.1.1 Small Contact Field

In case of hyperfine fields on nucleus of a non-magnetic ion, the contact term arising from the s electrons is small, and therefore, the contribution of transferred hyperfine field via the valence electrons becomes dominant. This applies e.g. to compounds having a non-magnetic sublattice or compounds with non-magnetic substitutions in a magnetic sublattice. It is then possible to use the calculated hyperfine field, eventually together with other hyperfine parameters (e.g. related to electric quadrupolar interaction), to simulate a theoretical NMR spectrum for comparison with the experiment.

We demonstrated the feasibility of this approach on lutetium iron garnet [60, 65]. NMR spectra simulated from calculated hyperfine parameters were in a good agreement with corresponding experimental NMR spectra for both cases: lutetium nuclei in regular non-magnetic sublattice of the garnet, as well as the lutetium being the anti-site defect (thus effectively a 'substitution') in magnetic sublattice of ferrice ions.

6.1.2 Hyperfine Field Anisotropy Calculation

A different approach is based on entirely bypassing the problematic contact term that is purely isotropic, by considering the anisotropy of the hyperfine field alone. The anisotropic component of the hyperfine field, ΔB_{hf}, consists of three parts that arise from the dipolar interaction of the nuclear spin with on-site electron spin, on-site electron orbital moment and magnetic moments of all other ions in the system:

$$\Delta B_{\mathrm{hf}} = \Delta B_{\mathrm{hf}}^{\mathrm{dip}} + \Delta B_{\mathrm{hf}}^{\mathrm{orb}} + \Delta B_{\mathrm{lattice}}^{\mathrm{dip}} \tag{6.1}$$

All these three parts of ΔB_{hf} can be calculated *ab initio*. As ΔB_{hf} sensitively reflects the electron structure of the ion in question, it may be well used to compare with the experiment, e.g. dependence of NMR spectrum on the direction of external magnetic field.

In order to introduce the magnetization into the calculation, naturally, the spin-orbit interaction has to be included. This imposes some further requirements on the calculation as spin-orbit coupling may reduce the symmetry, even split some equivalent atoms into non-equivalent ones, and also the eigenvectors become complex. While small systems may be calculated self-consistently with ease, for some complicated systems containing many atoms the convergence can be very difficult after adding the spin-orbit interaction.

However, in compounds we consider, the spin-orbit coupling represents a small perturbation. Therefore, it is a fairly good approximation to converge first the calculation without s-o, and then obtain the anisotropy with a single SCF step with s-o enabled.

6.1.3 Further Progress in Calculation of Contact Hyperfine Field

Besides the two approaches stated above, it is viable to attempt at circumventing the problem by other means. The core s electrons are polarized by on-site electrons with unpaired spins (e.g. $3d$), and so their contact hyperfine field should be proportional to the $3d$ magnetic moments. On the other hand, the contribution of valence s electrons, that are rather polarized by off-site electrons, should be related to the magnetic moment of these valence s electrons.

In ferrites, by calculating the spin magnetic moments of the $3d$ electrons and the valence $4s$ electrons of the iron atom, one can try to express the contact hyperfine field as their linear combination. After adding the contributions of the on-site interaction of the nuclear spin with the orbital and spin moment of the $3d$ electrons, the coefficients of the linear combination can be calculated by comparison with the hyperfine field experimentally determined in a number of iron compounds. Such method brings the theoretical contact fields within ~ 1 T of the values deduced from experiment. We describe this approach in [66].

Chapter 7

Results on Manganese Ferrites

Manganese ferrite has a partially inversed spinel structure where both cation sublattices are occupied partly by manganese and partly by iron. Two fundamental parameters determine the distribution of manganese and iron cations in the sublattices: manganese content x and degree of inversion y. This chapter concerns with two types of manganese ferrite single crystals that refer to these parameters: a series of $MnFe_2O_4$ with varying degree of inversion y and a series of $Mn_xFe_{3-x}O_4$ with varying manganese content x.

The first of the series, manganese ferrite single crystals with different degrees of inversion, we studied by means of ^{57}Fe NMR and by calculations of electronic structure. Issues of valence states of the cations and spin structure are addressed in the section 7.1.

The latter of the studied systems, manganese ferrite $Mn_xFe_{3-x}O_4$ single crystals, we investigated by ^{57}Fe NMR spectroscopy. The study of influence of manganese content x on distribution and valence states of cations in manganese ferrite is presented in section 7.2.

7.0.1 Studied Samples

The studied ferrite samples, prepared by group of Dr. V. A. M. Brabers (Technical University of Eindhoven), were high quality single crystals, grown by pulling the optically heated floating zone through the sintered polycrystalline rods of approximately 5 mm in diameter, as described in [67]. The iron and manganese contents, determined in the final single crystals by the wet chemical analysis, were within $\pm 3\%$ to the original compositions of the

polycrystalline rods. X-ray diffraction was used to prove that samples were homogeneous spinels without any second phase.

Samples of the B25 series were prepared from the same rod and various degrees inversions were achieved by a subsequent heat treatment. The inversion parameters y of samples from the B25 series were determined by Dr. M. Maryško and Dr. Z. Šimša (unpublished results) using magnetic measurements at 4.2 K and employing equation 2.1, while the inversion y of the sample B15A4 was directly obtained in Jirák *et al.* [6] using the neutron scattering measurements. Manganese ferrite samples studied in this work are summarized in Table 7.1.

sample	notation	μ_s (μ_B)	y_{mag}	$y_{neutron}$	sample
$MnFe_2O_4$	Sp1159				$Mn_{0.52}Fe_{2.48}O_4$
$MnFe_2O_4$	B25K9	4.88	0.06		$Mn_{0.84}Fe_{2.16}O_4$
$MnFe_2O_4$	B25C3	4.74	0.13		$Mn_{0.95}Fe_{2.05}O_4$
$MnFe_2O_4$	B25B10	4.71	0.15		$Mn_{1.00}Fe_{2.00}O_4$
$MnFe_2O_4$	B25D4	4.61	0.19		$Mn_{1.10}Fe_{1.90}O_4$
$MnFe_2O_4$	B25E4	4.56	0.22		$Mn_{1.25}Fe_{1.75}O_4$
$MnFe_2O_4$	B25A3	4.38	0.31		$Mn_{1.58}Fe_{1.42}O_4$
$Mn_{0.98}Fe_{2.02}O_{4.006}$	B15A4	4.79	0.09	0.077 ± 0.017	$Mn_{1.80}Fe_{1.20}O_4$

Table 7.1: Studied single crystal ferrite samples are listed, with their nominal composition, magnetic moments per formula unit and inversion parameters determined from magnetic measurements or from neutron diffraction.

7.1 Manganese Ferrites with Varying Degree of Inversion

For $MnFe_2O_4$ compound the distribution of Fe and Mn cations in tetrahedral A sites can be described by formula Fe_yMn_{1-y} and in octahedral B sites by formula $Fe_{2-y}Mn_y$, where y denotes the inversion parameter. While in manganese ferrite with normal spinel structure a simple picture of valence configuration $(Mn^{2+})[Fe^{3+}]_2O_4$ would hold, with nonzero degree of inversion the number of different cationic states increases.

7.1.1 ^{57}Fe NMR Experiments

In this section we describe a study of eight manganese ferrite samples with Mn content $x = 1$: Sp1159, B15A4, and six samples of series B25. ^{57}Fe NMR spectra were recorded in zero external magnetic field at temperature

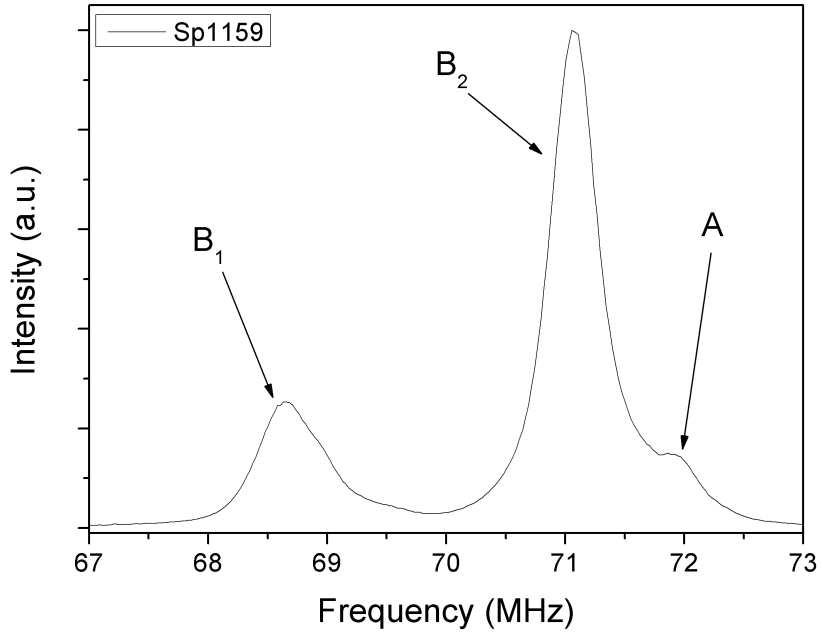

Figure 7.1: ^{57}Fe NMR spectrum of single crystal sample Sp1159 ($MnFe_2O_4$) was measured in zero external magnetic field at 4.2 K.

4.2 K, see Fig. 7.1, 7.4, and 7.5. Sample Sp1159 was used to assign the spectral lines to specific crystallographic positions, and therefore, it was also measured in external magnetic fields. All NMR spectra were recorded using the Carr-Purcell pulse sequence with excitation conditions carefully set to obtain NMR signal from nuclei in magnetic domains. Length of used sequences was much shorter than spin-spin relaxation times.

Two intensive resonance lines (66.67 and 71.09 MHz for Sp1159) can be observed in the NMR spectra. These lines are attributed to resonating nuclei of iron ions in octahedral B sites. Splitting of B site resonance into two lines (B_1 and B_2) originates in anisotropy of hyperfine field in trigonally distorted octahedral B sites (according to equation 3.12). In addition to B_1 and B_2 lines, all spectra include third line at higher frequency (71.94 MHz for sample Sp1159). This line corresponds to the resonance of iron nuclei in tetrahedral A sites.

Assignment of the resonant lines to A and B sites is evidenced by measuring the sample Sp1159 in external magnetic fields pointing along [100] direction. With increasing the external field, the B subspectrum moves

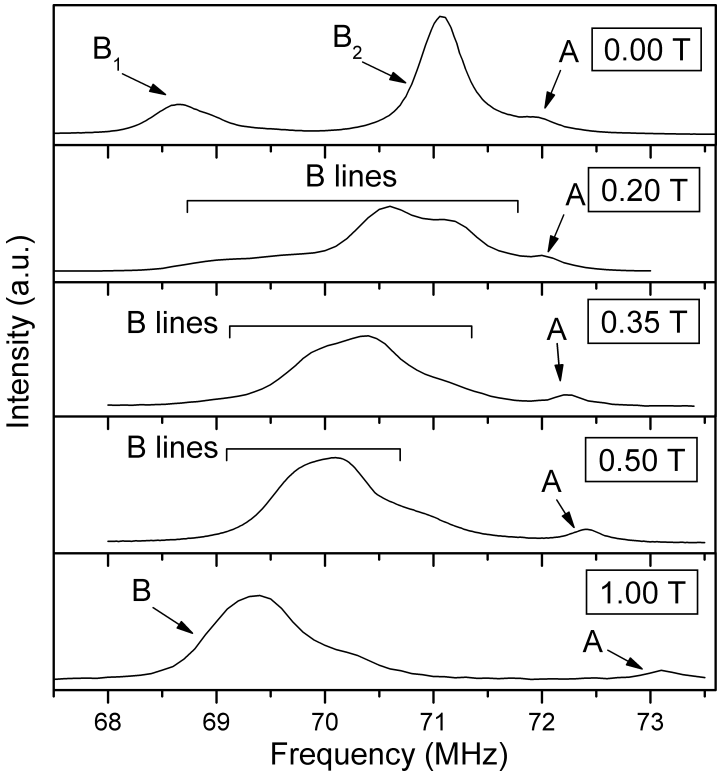

Figure 7.2: ^{57}Fe NMR spectra of $MnFe_2O_4$, (sample Sp1159), in dependence on external magnetic field applied approximately in [100] direction were measured at 4.2 K.

towards lower frequencies, on the other hand, the A line shifts to higher frequencies (Fig. 7.2). This behaviour indicates that the hyperfine fields in B sites have opposite direction with respect to the direction of hyperfine fields in A sites. Since the hyperfine field on ^{57}Fe nucleus is known to be antiparallel to the magnetic moment of the ion, the electronic magnetization of B sublattice lies in the direction of total magnetization, while magnetization of A sublattice lies in the opposite direction. Furthermore, the assignment of resonance lines is also supported by the fact that the intensity of A line increases with increasing inversion y (Fig. 7.4), since higher degree of inversion means higher amount of ferric ions in the tetrahedral A sites.

Analysis of our ^{57}Fe NMR experiments shows that the spin structure of manganese ferrite is the one that complies with the Goodenough-Kanamori-Anderson rules. This however contradicts the recent results of Shim *et al.* [20], who measured ^{57}Fe NMR spectra of powder manganese ferrite in external magnetic field. We reanalyzed these results and showed that their

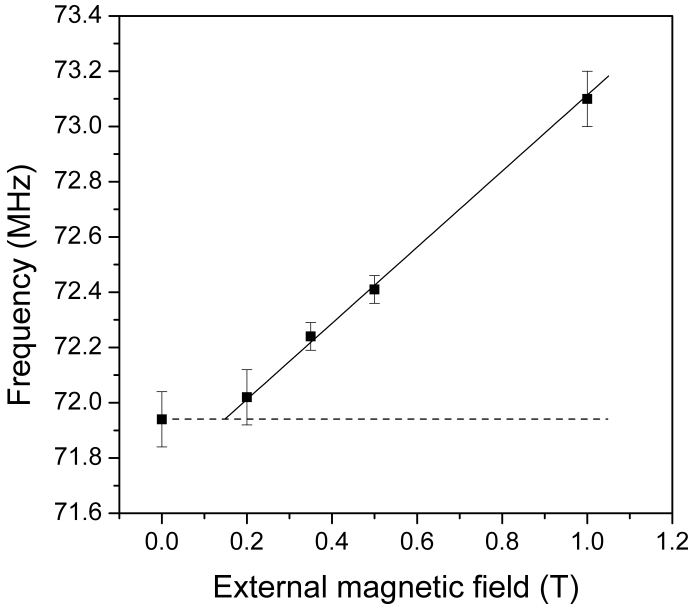

Figure 7.3: Frequency shift of A line for sample Sp1159 in dependence on external magnetic field (squares). Above 0.2 T the dependence corresponds to a linear growth given by the gyromagnetic ratio of ^{57}Fe nucleus (solid line). Non-linear behaviour in the lower fields is influenced by the presence of magnetic domain structure.

analysis of ^{57}Fe NMR spectra was incorrect, as the authors did not consider a rather large hyperfine field anisotropy in the octahedral B sites, which broadens the B site spectrum in a powder sample. We reinterpreted the results of Shim *et al.* in [24].

As follows from the local symmetry of B sites (and is in agreement with the angular dependence of resonant frequency f of the B lines [19]), the hyperfine field anisotropy contribution in equation 3.12 for the direction of magnetization [100] is zero (see section 3.3.1). Therefore, applying field along this direction caused the B lines that were initially split for magnetization along [111], to merge into one line (with maximum at about 69.4 MHz). Simultaneously, the A line, having zero hyperfine field anisotropy in general, was originally at 71.94 MHz and shifted with the applied field linearly (above ~ 0.20 T) to higher frequencies. Slope of the shift is given by gyromagnetic ratio of ^{57}Fe nucleus as demonstrated in Fig. 7.3.

$MnFe_2O_4$ single crystal samples (the B25 series, see Table 7.1) were measured in zero external magnetic field at temperature 4.2 K (displayed in Fig. 7.4). A broad range of degrees of Mn-Fe inversion was introduced into these samples by different heat treatment. The values of inversion, denoted

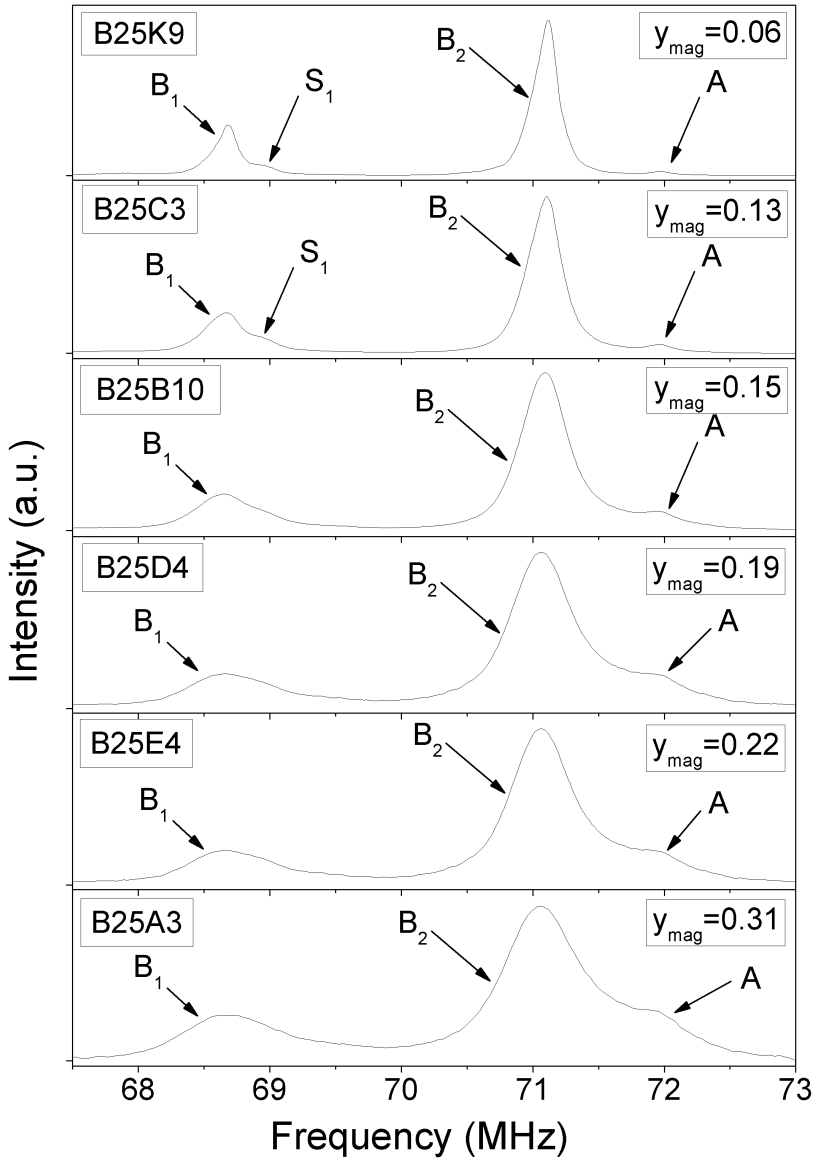

Figure 7.4: ^{57}Fe NMR spectra of six $MnFe_2O_4$ single crystals in zero external magnetic field at 4.2 K.

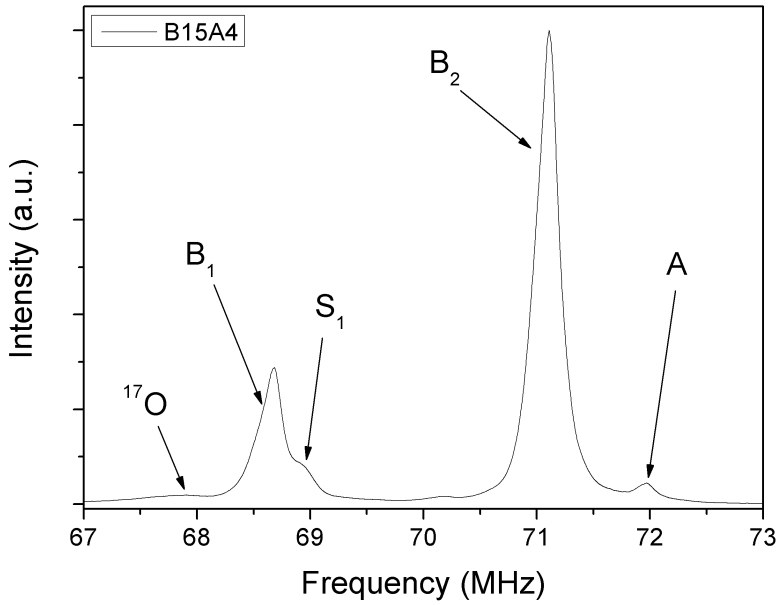

Figure 7.5: ^{57}Fe NMR spectrum of single crystal sample B15A4 ($Mn_{0.98}Fe_{2.02}O_4$) was measured in zero external magnetic field at 4.2 K. Interestingly, also a weak ^{17}O NMR line appears near the B_1 line.

as y_{mag} in Fig. 7.4, were evaluated from magnetic measurements at 4.2 K by using equation 2.1. Besides the B25 series, also spectrum of single crystal sample $Mn_{0.98}Fe_{2.02}O_{4.006}$ (notation B15A4, see Fig. 7.5) was measured.

For a small degree of inversion, the disorder in the system is low, and so the NMR lines are relatively narrow. This makes possible to observe a satellite structure, especially near the B_1 line, which is well apart from the other lines in the spectrum (e.g. satellite at 68.96 MHz for sample B25K9). Increase of the inversion brings more disorder to the cationic configuration, therefore, the spectral lines become significantly broadened and satellites become undistinguishable.

The character of B15A4 spectrum corresponds to spectra of the B25 series. Concerning the line widths and intensity of the A line, the NMR spectrum of B15A4 resides between two B25 samples with the lowest inversion (B25K9 and B25C3), as can be seen from their confrontation in Fig. 7.6.

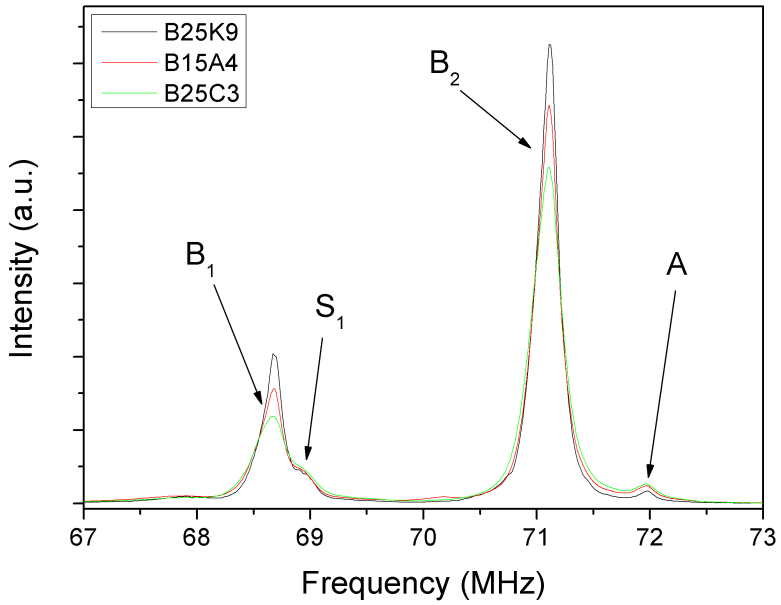

Figure 7.6: NMR spectrum of B15A4 is compared with spectra of samples B25K9 and B25C3. The spectra are normalized with respect to their integral intensity.

7.1.2 Analysis of the Inversion

In order to analyze the NMR results quantitatively, we pursued the intensities of NMR spectral lines. Due to overlap of the spectral lines, a mere integration of the line area would not suffice even for spectrum of sample with the lowest inversion. Therefore, in order to obtain spectral line intensities, the spectra were subjected to a fitting procedure.

For a fitting function it was inappropriate to use Lorentzian, which would correspond to homogeneous line broadening, or the Gaussian, corresponding to a sum of large number of small independent contributions, as the inhomogeneous broadening does not necessarily result in a Gaussian distribution [68]. The experimental spectral lines are described better by a Lorentzian powered to factor of two (a special case of Pearson function of type VII), rather than pure Lorentzian or Gaussian, especially at the tails that are essential e.g. in the case of a weak line overlapping with a long tail of an intensive line. Such Lorentzian powered to factor of two:

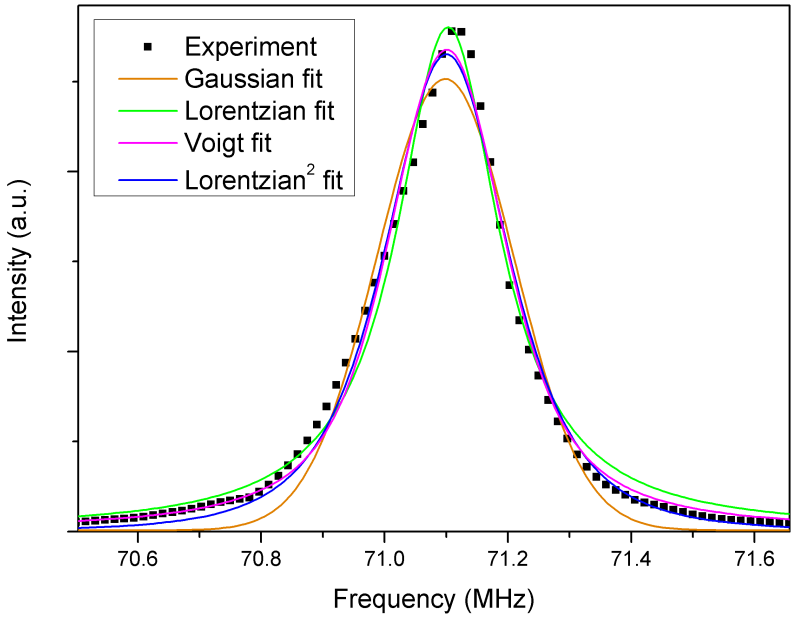

Figure 7.7: Comparison of various fitting functions is displayed. It can be seen, that pure Gaussian or Lorentzian curves fail to describe the experimental data, especially at tails of the line, where Lorentzian^2 or Voight functions perform better. NMR line B_2 of sample B25K9 with the lowest degree of inversion was used.

$$L^2(f;\, A,\, f_0,\, w) = \frac{2Aw}{\pi} \frac{w}{((f - f_0)^2 + w^2)^2}, \tag{7.1}$$

provides reasonable agreement with the experimental data (see Fig. 7.7 for comparison of several fitting curves). It involves three parameters, A, f_0, and w, denoting the amplitude, frequency offset and width.

Two main factors influence the reliability of the fits. Most markedly, the spectral lines have slightly asymmetric shapes, which is due to presence of asymmetrical shifts of non-resolved satellite spectral lines. Such character of the line shape can be clearly observed on B_2 line, where the satellites are not resolved, while quite a distinct satellite appears near B_1 line at 68.97 MHz, denoted as S_1. (See Fig. 7.4, spectrum of B25K9.) Example of the fitting procedure for Fe(A) and Fe(B_2) lines is displayed in Fig. 7.8.

Generally, a satellite line emerges in such cases where the local structure surrounding the atom with resonating nucleus differs from the prevailing one

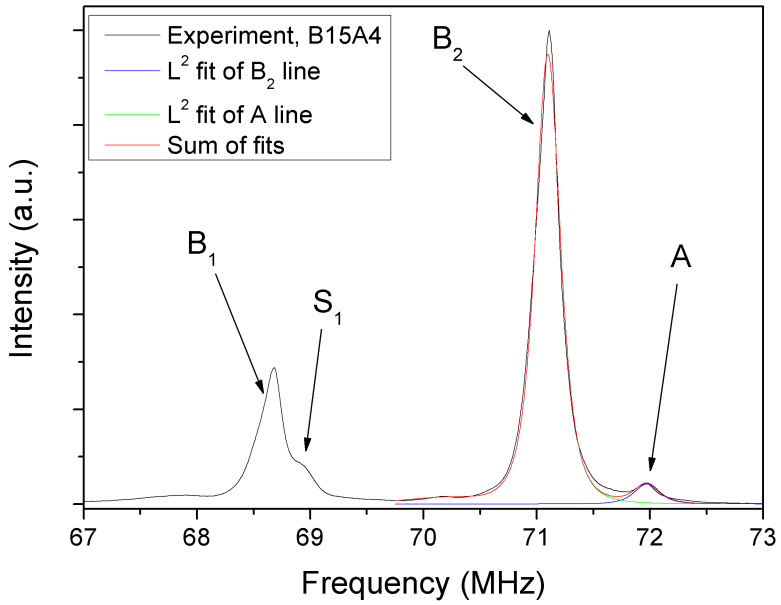

Figure 7.8: Example of the fitting procedure for Fe(A) and Fe(B_2) NMR lines of sample B15A4.

(chapter 3). In case of manganese ferrite, the satellites originate predominantly due to manganese cations in B sites, Mn(B), and iron cations in A sites, Fe(A), that are connected with the inversion. For low values of inversion, the concentration of Mn(B) and Fe(A) is rather small, therefore, only satellites corresponding to the presence of one such ion in the vicinity of the resonating nucleus occur, and relative intensity of such satellites is low, compared to the intensity of main line.

As the degree of inversion increases, supposing random distribution of Mn(B) and Fe(A) so that a binomic distribution of probability may be used, even the satellites relevant to multiple occurrences of Mn(B) or Fe(A) in the nearest neighbourhood of the resonating nucleus must be considered. Moreover, the probability of coincidental presence of both types of ions, Mn(B) and Fe(A), is no longer negligible. E.g. for inversion $y \sim 0.17$, the relative intensity of ideal nearest neighbourhood of a B site (i.e. the former "main line", corresponding to perfectly normal distribution of cations) is lower than 10% of the total B subspectrum. Therefore, one can expect quite a high number of satellite lines corresponding to various configurations of neighbouring ions with respect to the resonating nucleus. As a consequence,

individual satellites can no longer be distinguished, since they merge together, and concurrently, the distinguished features of the spectrum are reduced. The lines become significantly broadened and overlapped, which is the second important factor burdening the quality of the fits.

The degree of inversion can be estimated from intensities of the NMR spectral lines, since the integral intensity is proportional to the number of resonating nuclei. Therefore, the intensities of NMR lines are related to the concentration of corresponding atoms in sublattices:

$$I_{\mathrm{A}} \sim y, \tag{7.2}$$

$$I_{\mathrm{B}_2} \sim \frac{3}{4}(2-y). \tag{7.3}$$

Comparing these intensities then yields relation between the ratio of intensities and inversion y:

$$\frac{I_{\mathrm{A}}}{I_{\mathrm{B}_2}} = \frac{y_{\mathrm{NMR}}}{\frac{3}{4}(2-y_{\mathrm{NMR}})}. \tag{7.4}$$

Values of inversion parameter y acquired from this procedure are displayed in Table 7.2 as y_{NMR} case *a*.

Another way of determining the inversion is to confront the integral intensity of the resolved satellite S_1 with the B_1 line intensity. If the arrangement of cations is random, the intensities of satellite S_1 and line B_1 may be written according to binomic distribution as:

$$I_{\mathrm{S}_1} \sim 6k(1-k)^5, \tag{7.5}$$

$$I_{\mathrm{B}_1} \sim (1-k)^6. \tag{7.6}$$

Parameter k denotes the concentration of such a local crystal arrangement, that induces the satellite S_1; i.e. it takes different values $k_{\mathrm{Fe(A)}}$ or $k_{\mathrm{Mn(B)}}$ depending on whether the satellite S_1 is induced by Fe(A) or by Mn(B), respectively (deduced inversion is displayed in Table 7.2, cases *b*, *c*). The ratios of the intensities of the corresponding spectral lines are then connected with the degree of inversion by:

$$\frac{I_{\mathrm{S}_1}}{I_{\mathrm{B}_1}} = \frac{6k}{1-k}. \tag{7.7}$$

The procedure of obtaining degree of inversion by using satellite S_1, however, loses its justification as soon as higher binomic contributions start to play a role due to increasing probability for co-occurrence of Mn(B) and Fe(A) ions. Nevertheless, it is worthy to analyze the results in a bit more detail.

The presence of satellite S_1 is connected with the inversion of manganese and iron cations, i.e. S_1 originates either due to Mn(B) or Fe(A). The number of satellite lines in the B subspectrum can be determined from the symmetry analysis of the local crystal structure, i.e. considering that there are six nearest tetrahedral and six nearest octahedral neighbours to each octahedral B site, and also including the direction of magnetization $\langle 111 \rangle$. Both Mn(B) or Fe(A) would induce a satellite pattern of three lines with mutual ratio of intensities 1:2:1 in the NMR spectrum of Fe(B). The satellite S_1 then can be attributed to one of these lines with nominal intensity of 1 belonging to B_1 parent line. The remaining satellites (intensities 2 and 1) belong to the B_2 line and are most likely unresolved or hidden under the main line.

As the inversion is low, we can neglect any multiple occurrences of either Mn(B) or Fe(A), likewise the co-occurrence of both. However, the probability that one Fe atom is present in any of the six neighbouring A sites of Fe(B) is different from the probability of one Mn atom being in any of the six B sites in the neighbourhood. This is simply due to the fact, that concentration of iron atoms in A sublattice is $k_{\mathrm{Fe(A)}} = y$, which is two times higher than the concentration of manganese atoms in B sublattice, $k_{\mathrm{Mn(B)}} = y/2$. Therefore, we can exploit the difference in these two scenarios, compare the values of inversion obtained from analysis of satellite S_1 and Fe(A) line and ask what induces the satellite S_1. Values of inversion parameter y evaluated from 7.7 are displayed in Table 7.2 as cases b and c. Analysing line intensities in the spectra of samples with low inversion, i.e. B25K9, B25C3, and B15A4, we can suggest that the satellite S_1 is more likely to be induced by the presence of manganese in the nearest B neighbourhood to the resonating ^{57}Fe nuclei in the B_1 sites. Although the difference between those two scenarios is factor of two, the assignment, based solely on satellite S_1 intensity, remains quite speculative, owing to large relative errors in determination of y.

While increasing number of possible satellites disallows obtaining higher values of inversion y from the intensities of satellite S_1, evaluation of y from Fe(A) and Fe(B_2) intensities is not hindered by such systematic error. Therefore, it was possible to obtain the values of inversion from NMR spectra for all measured samples (Table 7.2, case a). Direct comparison of NMR results with those from neutron diffraction was possible for the B15A4 sample. The intensity of NMR line corresponds to the amount of iron in the tetrahedral sites, hence to obtain the degree of inversion y, a factor of 0.02 was subtracted to reflect the fact that sample B15A4 is slightly iron rich, $Mn_{0.98}Fe_{2.02}O_{4.006}$. For samples of the B25 series (manganese content

sample	y_{neutron}	y_{mag}	$I_{\text{A}}/I_{\text{B}_2}$	y_{NMR} (a)	$I_{\text{S}_1}/I_{\text{B}_1}$	y_{NMR} (b)	y_{NMR} (c)
B15A4	0.077(17)	0.09(2)	0.045(5)	0.05(1)	0.21(11)	0.01(1)	0.05(2)
B25K9		0.06(2)	0.022(6)	0.03(1)	0.13(5)	0.02(1)	0.04(2)
B25C3		0.13(2)	0.049(8)	0.07(1)	0.26(16)	0.04(3)	0.08(5)
B25B10		0.15(2)	0.11(1)	0.16(2)			
B25D4		0.19(2)	0.19(4)	0.25(4)			
B25E4		0.22(2)	0.19(5)	0.25(5)			
B25A3		0.31(2)	0.24(4)	0.31(5)			

Table 7.2: Values of inversion y evaluated from NMR experiments performed in this work are confronted with values of inversion obtained by from magnetization measurements and equation 2.1 or from neutron diffraction. Column (a) contains values of y_{NMR} evaluated from equation 7.4. Inversion evaluated from intensity of satelite S_1 using equation 7.7 is displayed in columns (b) and (c), supposing the satellite S_1 originates due to Fe(A) and Mn(B), respectively. Results for B15A4 sample were corrected for non-stoichiometricity. Indicated errors of y_{neutron} and y_{mag} arise from 5% experimental error in the integral intensities of reflections, and 1% error in the measurement of magnetic moment.

$x = 1.00$), the NMR results were compared with inversion evaluated from magnetization measurements and equation 2.1.

Despite considerable errors the values of degree of inversion display, at least y_{NMR} (a), evaluated from Fe(A) line intensities, can be used to compare results of particular methods. Comparison of y_{NMR} (a) and y_{neutron} on sample B15A4 shows that evaluation from NMR gives about 40% lower degree of inversion. Also comparing y_{NMR} (a) and y_{mag} (samples B25) reveals that the values given by NMR (using intensity of A line) are systematically lower. This is clearly seen for samples with small inversion, where the lines are well separated: inversion evaluated from fits of A line is roughly half the value of y_{mag}. For compounds with higher inversion, the disagreement is less pronounced; however, the decomposition of NMR spectra is less reliable, because of an increasing overlap of the lines. (Possibly, Fe(A) line might cover some satellites, analogous to satellite S_1, but belonging to Fe(B_2) line.)

Our explanation of the differences lies in non-random distribution of the cations. The analysis of the inversion (eq. 7.4) assumed that the NMR line intensity is proportional to the concentration of corresponding atom in its sublattice. However, if some pairing of Fe(A) was present (e.g. Fe(A)-Fe^{2+}(B), Fe(A)-Mn^{3+}(B)), it could have an effect on the Fe(A) NMR line intensity. For example, localized Fe^{2+}(B) has considerable orbital momentum, which is connected with very rapid relaxation of its nuclear spin, and

compound	Fe radius (a.u.)	Mn radius (a.u.)	O radius (a.u.)	matrix size (RK_{max})	k-points (division)	G_{max}
$(Mn_2)[Fe_4]O_8$	1.9	1.9	1.58	1919 (7.0)	16 (6 6 6)	16
$(Mn_{15}Fe)$ $[Fe_{31}Mn]O_{64}$ supercell S_A	1.8	1.8	1.6	12576 (7.0)	28 (6 6 6)	16
$(Mn_{15}Fe)$ $[Fe_{31}Mn]O_{64}$ supercell S_B	1.8	1.8	1.6	12576 (7.0)	63 (6 6 6)	16
$(Mn_{15}Fe)$ $[Fe_{31}Mn]O_{64}$ supercell S_C	1.8	1.8	1.6	12576 (7.0)	28 (6 6 6)	16
$(Mn_{15}Fe)$ $[Fe_{31}Mn]O_{64}$ supercell S_D	1.8	1.8	1.6	12576 (7.0)	63 (6 6 6)	16

Table 7.3: Parameters used for calculations are displayed. For density of states plots, numbers of k-points were increased for normal cell of $Mn_2Fe_4O_8$ and supercell S_C to 104 (division: 14 14 14) and 44 (division: 7 7 7) respectively. 1 a.u. = 0.0529177 nm.

therefore it cannot be observed by NMR. As a consequence, Fe^{3+}(A) trapped in a close proximity of such Fe^{2+}(B) would not contribute to the NMR signal. Such pairing could be induced by Coulomb attractive interaction: since the A sublattice is otherwise occupied by Mn^{2+}, Fe^{3+}(A) represents an extra positive charge, whereas Fe^{2+}(B) possesses an extra negative charge.

Such pairing process is effective especially for small values of inversion. As the inversion increases, the number of Fe^{2+}(B) or Mn^{3+}(B) increases and the extra charge carried by such cation tends to delocalize. The delocalization causes gradual disappearance of the orbital momentum, and thus the above stated relaxation mechanism becomes ineffective. Analogously, the non-random arrangement affects the results obtained by analysis of satelite S_1 intensity, as the assumed binomic distribution becomes invalid.

7.1.3 Calculations of Manganese Ferrite Electronic Structure

In this section the question of electronic states of the cations in $MnFe_2O_4$ is addressed by performing the *ab initio* calculations of its electronic structure. Besides calculating the unit cell of normal manganese ferrite, that is composed of two formula units, i.e. $Mn_2Fe_4O_8$, the calculations were also performed on $2 \times 2 \times 2$ supercells, since the former calculations [21, 22] were limited to a normal distribution $(Mn)[Fe_2]O_4$ of manganese and iron, which does not allow to study the partially inverted structures.

The parameters used for calculations are summarized in Table 7.3. For

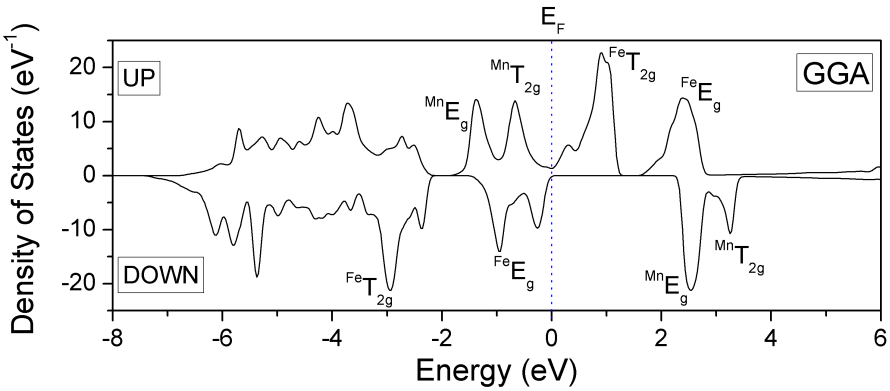

Figure 7.9: Density of states plot for spins up (minority) and down (majority) near the Fermi level for normal cell of manganese ferrite. Calculation used GGA, which resulted in (half) metallic character of the compound.

the exchange-correlation functional the generalized gradient approximation of Perdew-Burke-Ernzerhof [62] was employed. Calculated density of states reveals half metallic band structure (see Fig. 7.9), which does not conform with manganese ferrite being an insulator. There are two possible explanations for this disagreement. One of them is that the atomic disorder in real manganese ferrite samples leads to Anderson localization, which is responsible for insulating character. Hence, the calculation cannot arrive to an insulating state, as it is performed on $MnFe_2O_4$ cell with zero inversion. The second explanation lies beyond density functional theory, as electron correlations may play a significant role. These two possibilities were analyzed by performing adequate calculations.

In order to introduce some cationic disorder into the structure, a supercell $2 \times 2 \times 2$ was formed with 112 atoms. Afterwards, one manganese atom was swapped with iron atom, so that the compound became $(Mn_{15}Fe)[Fe_{31}Mn]O_{64}$, corresponding to an inversion factor $y = 0.0625$. Within the supercell there were four possible positions for such Mn(B)–Fe(A) pair, thus four different superstructures were produced: S_A, S_B, S_C, and S_D (see Table 7.4 and Fig. 7.10). However, changing the normal spinel to a partially inverted one caused the symmetry to decrease drastically from cubic to rhombohedral for supercells S_A, S_C and to monoclinic for other two structures. The magnetic structure of these supercells was set collinear with all spins on the A sublattice antiparallel to the spins on sublattice B, i.e. in ac-

	spacegroup	Fe(A)-Mn(B) distance (nm)
S_A	R3m	0.551493
S_B	Cm	0.353918
S_C	R3m	0.694496
S_D	Cm	0.549269

Table 7.4: Parameters of four calculated supercell structures, d is the Mn(B)-Fe(A) distance.

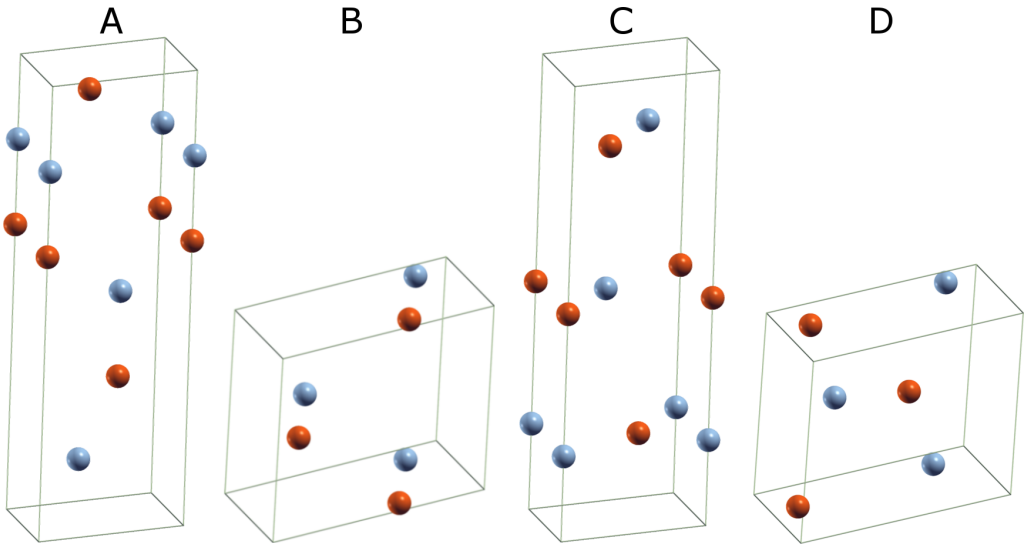

Figure 7.10: Schematically drawn unit cells of the calculated supercells S_A–S_D. For simplicity, all atoms but the inversion pair, Fe(A) and Mn(B), are omitted. Orange spheres denote iron atoms Fe(A) and grey spheres represent manganese atoms Mn(B).

cordance with our NMR measurements. Free internal structural parameters were optimized for all four structures by minimizing the total energy and the forces on the nuclei. To that end, the RMT radii were slightly adjusted in the supercells, in order not to constrain the atomic displacements.

The effect of cationic disorder on electronic structure was studied on one of the supercells (S_C) to suggest, whether the Anderson localization is the cause for non-insulating DOS in the normal cell calculation. GGA calculation of the S_C supercell illustrates that the metallic character of the DOS persists an installation of disorder into the structure via the cationic inversion, see Fig. 7.11.

The question concerning the role of electron correlations in manganese ferrite was investigated by employing GGA+U. Values of parameters $U_{\mathrm{Mn}} =$

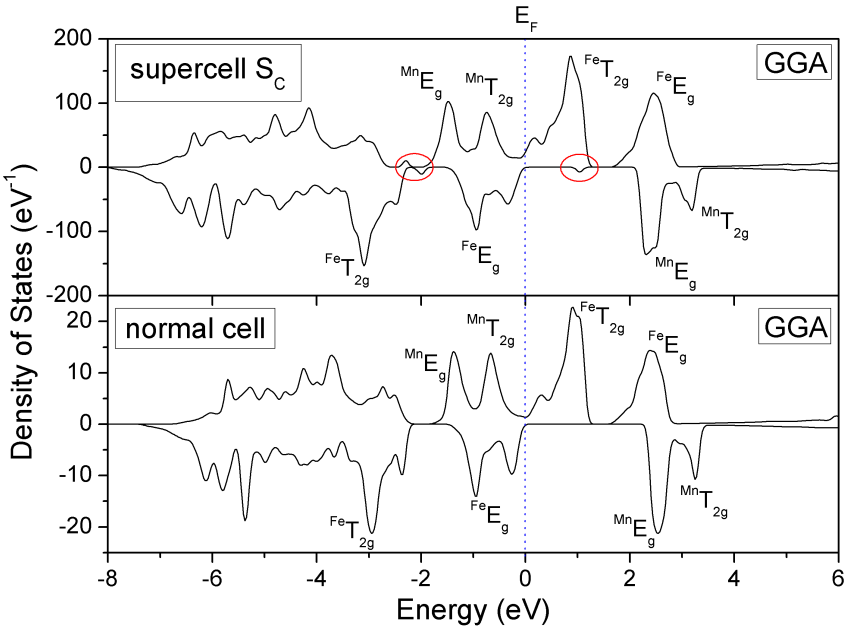

Figure 7.11: Comparison of density of states for spins up (minority) and down (majority) near the Fermi level for normal cell (no cationic disorder) and supercell structure S_C (inversion $y = 0.0625$). Several of the d bands of Fe(A) and Mn(B) are well separated and visible (emphasised in red ovals). Note that the number of states in the supercell plot is higher due to its eight times larger unit cell.

4.0 eV and $U_{\mathrm{Fe}} = 4.5$ eV were used to calculate the normal $MnFe_2O_4$ cell. GGA+U is expected to lower the energy of occupied states, while increasing the energy of partially occupied or empty states. This is evidenced in Fig. 7.12, the $^{\mathrm{Mn}}T_{2g}$ and $^{\mathrm{Fe}}T_{2g}$ states in the minority (up) spin channel become clearly separated, and therefore a true gap is opened.

Magnetic moments, as obtained from four supercell calculations, are summarized in Table 7.5. To identify the valence state of the cations, the magnetic moments are more suitable than the charges. However, the moments cannot be taken too literally, as the contribution to atomic moments from the interstitial region is disregarded. The values of magnetic moments of Mn(A) and Fe(A) confirm, that the valence states are Mn^{2+} and Fe^{3+} in the tetrahedral sites, both corresponding to formal spin moment of 5 μ_{B}. The moment of Fe(B) is slightly larger than that of Fe(A), despite that there is one extra electron with the opposite spin direction present on the

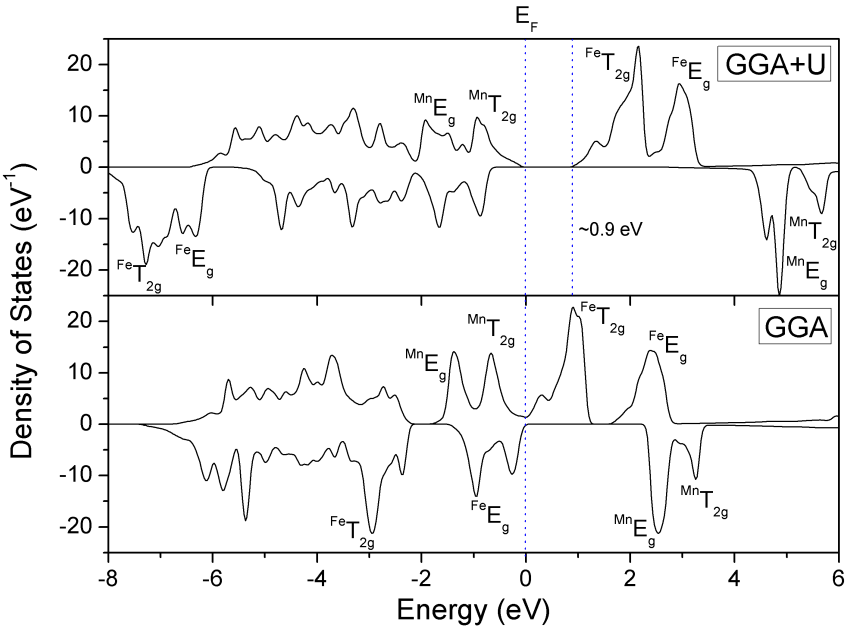

Figure 7.12: Comparison of density of states for spins up (minority) and down (majority) near the Fermi level, calculated with GGA and with GGA+U. Potentials $U_{\mathrm{Mn}} = 4.0$ eV and $U_{\mathrm{Fe}} = 4.5$ eV were applied on the $3d$ orbitals.

octahedral Fe atoms, which should reduce the moments of Fe(B) instead. This is likely to be connected with the larger Fe($3d$)-O($2p$) hybridization in the tetrahedral site compared to the octahedral one. Scan of the moments of iron ions on the B sites shows that the extra electron is not localized, but distributed over the octahedral irons. Similar conclusion follows from the comparison of metal-oxygen distances (Table 7.6). Ionic radius of octahedral Mn^{3+} is the same as the one of Fe^{3+} and equals to 0.0645 nm, while the radius of Fe^{2+} is 0.0780 nm. The difference between Fe(B)-oxygen distances is of the order 10^{-3} nm, i.e. much smaller than the difference of the ionic radii.

Contrary to irons, the magnetic moments of Mn(B) display quite significant differences among the four calculated structures. Values of the moments indicate that for the S_A supercell the Mn(B) is clearly Mn^{2+}, while for S_B and S_D the octahedral manganese is rather Mn^{3+}. In case of S_C, the magnetic moment of Mn(B) is even lower, which implies that the valence of Mn(B) is actually +4. Valence states inferred from the magnetic mo-

	μ (μ_B)	S_A	S_B	S_C	S_D
Mn(A)	max.	4.008	4.023	4.023	4.019
	mean	3.998	4.003	4.008	4.005
	min	3.987	3.991	3.999	3.997
Fe(A)		3.901	3.897	3.906	3.906
Fe(B)	max.	−4.041	−4.035	−4.029	−4.034
	mean	−4.038	−4.026	−4.013	−4.026
	min	−4.033	−4.018	−4.003	−4.017
Mn(B)		−4.161	−3.443	−2.649	−3.450
Oxygen	max.	−0.241	−0.237	−0.234	−0.237
	mean	−0.223	−0.217	−0.210	−0.217
	min	−0.075	−0.056	−0.078	−0.076
E_{tot} (meV)		71	0	756	128
Fe(A)–Mn(B) distance (nm)		0.551493	0.353918	0.694496	0.549269

Table 7.5: Magnetic moments contained within the atomic spheres and total energy relative to supercell S_B.

	R (nm)	S_A	S_B	S_C	S_D
Fe(B)	max.	0.20341	0.20428	0.20432	0.20386
	mean	0.20329	0.20354	0.20377	0.20354
	min	0.20282	0.20323	0.20361	0.20306
Mn(B)		0.21550	0.20280	0.19252	0.20258

Table 7.6: Distance cation-oxygen for octahedral Fe and Mn ions.

ments agree with Mn(B)-oxygen distances in Table 7.6, as the ionic radii of octahedral Mn^{2+}, Mn^{3+}, and Mn^{4+} in high spin states are 0.0970 nm, 0.0785 nm, and 0.0670 nm, respectively. The octahedron in S_C is significantly contracted around the smaller Mn^{4+}, while oxygens in S_A are pushed further away from the Mn^{2+}.

Of interest are the total energies, though only those supercells that have the same symmetry should be compared directly. As seen from Table 7.5, the differences in energy, $E_{tot}(S_C) - E_{tot}(S_A)$ and $E_{tot}(S_D) - E_{tot}(S_B)$, correlate notably with distance of the Fe(A)-Mn(B) pair. The energetic differences between the supercells are significant when compared to 109 meV energy, which is the energy gained per interchange of one pair Fe–Mn (calculated by Singh *et al.* [21]). The conclusion to be drawn is that the total energy is sensitive to the location of iron on the A-site and Mn on the B-site, and close arrangement of the Fe(A)-Mn(B) pair is preferred. Such outcome

supports the conception of non-random distribution of iron atoms in the A sublattice.

7.1.4 Hyperfine Field Anisotropy in Manganese Ferrite

In the following, the anisotropic contributions to the hyperfine field on ^{57}Fe nucleus were evaluated by including the spin-orbit interaction (s-o) in the calculations. The procedure consisted in lowering the symmetry of a fully converged calculation without s-o, so that the structure was suitable for any direction of magnetization in the $(0\bar{1}1)$ plane. Such plane was chosen in consistence with rotation plane used in measurements of ^{57}Fe NMR spectra anisotropy by Kovtun *et al.* [19] to allow direct comparison. As a result of lower crystal symmetry (4 operations left of 48), the total number of non-equivalent atom sorts in the unit cell increased from 3 to 7. The octahedral irons split to three magnetically nonequivalent groups with ratio 1:2:1.

The energy window was increased from 2.0 Ry to 3.2 Ry in order to include more eigenstates into the calculation. The evaluation of hyperfine field anisotropy contributions $\Delta B_{\mathrm{hf}}^{\mathrm{dip}}$ and $\Delta B_{\mathrm{hf}}^{\mathrm{orb}}$ was performed self-consistently. Individual dependences $\Delta B_{\mathrm{hf}}^{\mathrm{dip}}$ and $\Delta B_{\mathrm{hf}}^{\mathrm{orb}}$, together with off-site dipolar contributions $\Delta B_{\mathrm{lattice}}^{\mathrm{dip}}$, are displayed in Fig. 7.13.

The experimental angular dependence of ^{57}Fe NMR spectra of octahedral sites in manganese ferrite was measured by Kovtun *et al.* on a cylindrical sample in external magnetic field 0.5 T, which was applied in a plane of (011) type. For a better comparison with the calculated anisotropy (see Fig. 7.14), the isotropic part of the experimental data was subtracted and the frequency scale was transformed into units of Tesla.

Calculated values of hyperfine field in the angular dependence for the octahedral sites are included within the interval (-0.45, 0.24) in units of Tesla around its isotropic part, which is markedly shorter than the interval (-1.28, 0.64) of the experimental data. However, from the comparison in the Fig. 7.14 it is clear that the shapes of calculated curves are commensurate with the experimental dependences: the calculation correctly reproduced the numbers of lines in particular directions so that an unambiguous assignment of individual dependences in experimental and calculated results is possible.

The dependence of NMR resonance frequency and related anisotropy of the hyperfine field may be analyzed quantitatively by using equation 3.9 and considering the form of anisotropy tensor $\mathbf{A}$. As the octahedral sites in manganese ferrite have local site symmetry D_{3d} with $\bar{3}$ axis along $\langle 111 \rangle$, the

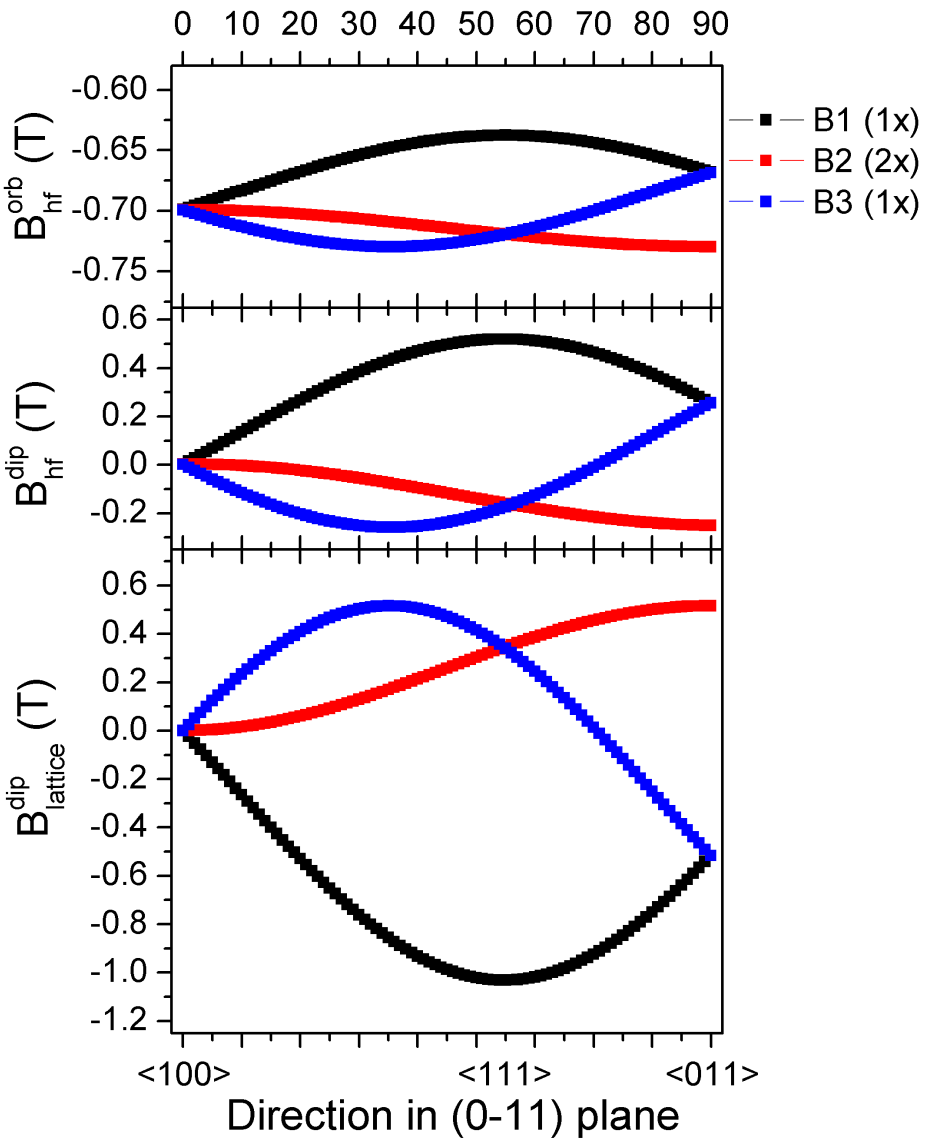

Figure 7.13: Angular dependences of the individual calculated terms of ΔB_{hf} are displayed; dipolar interaction of the nuclear spin with on-site electron spin, $\Delta B_{\mathrm{hf}}^{\mathrm{dip}}$, on-site electron orbital moment, $\Delta B_{\mathrm{hf}}^{\mathrm{orb}}$, and magnetic moments of all other ions in the system, $\Delta B_{\mathrm{lattice}}^{\mathrm{dip}}$. Note, that the scale of $\Delta B_{\mathrm{hf}}^{\mathrm{orb}}$ plot is different.

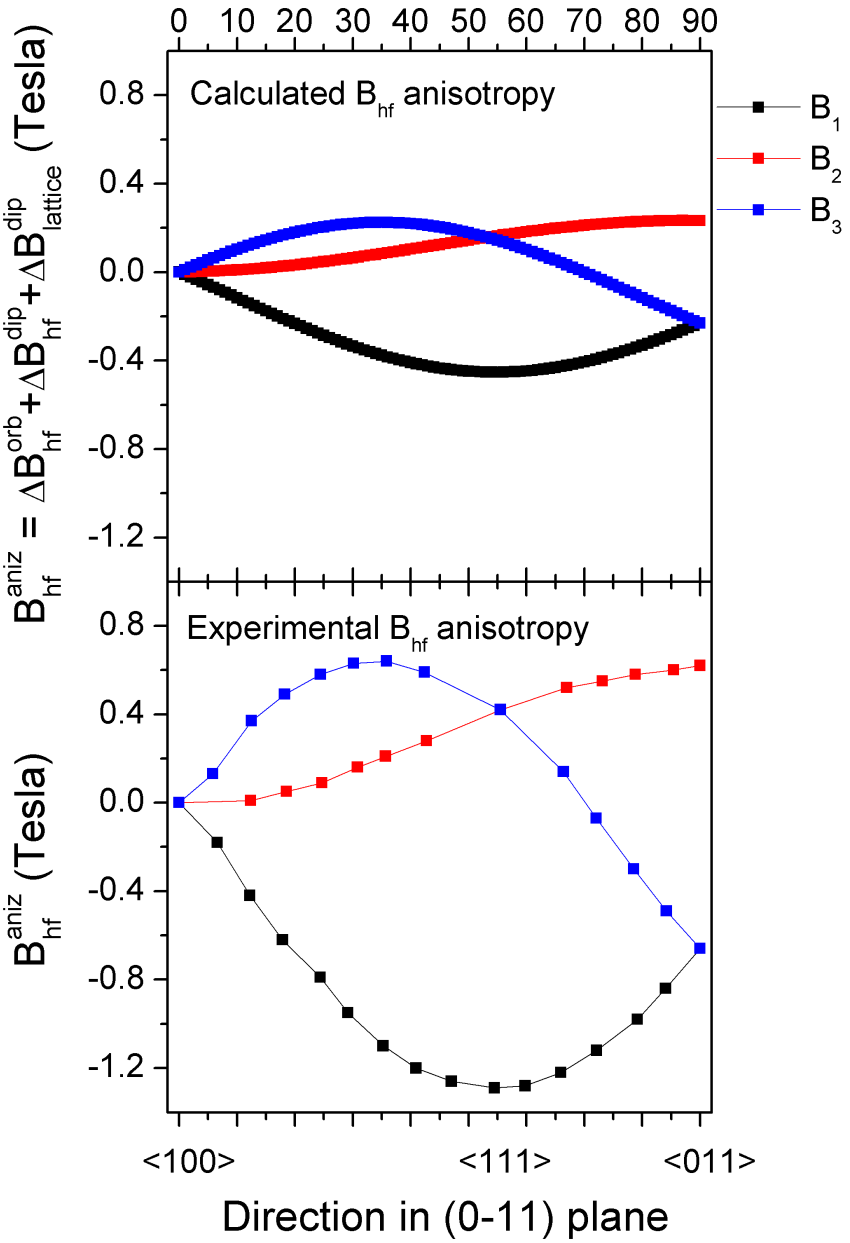

Figure 7.14: Comparison of experimental and calculated hyperfine field anisotropy of the octahedral B sites for direction of magnetization in $(0\bar{1}1)$ plane is displayed. Isotropic parts were left out for both sets of data. The experimental data were derived from angular dependences of ^{57}Fe NMR spectra measured at 1.8 K in external magnetic field of 0.5 T by Kovtun *et al* [19].

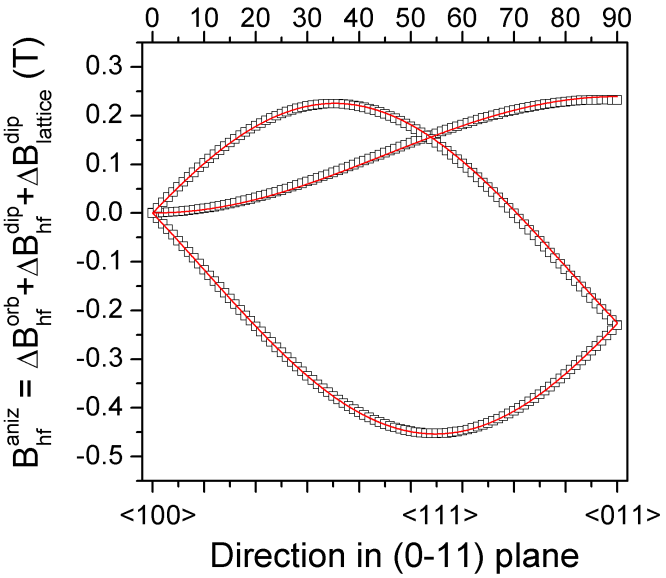

Figure 7.15: An example of fitting procedure. Calculated anisotropy in octahedral sites (squares) was fitted using equations for $B^{(1)}$ and $B^{(2,3)}$ (red line).

tensor $\mathbf{A}$ keeps only one independent component, and may be represented in the coordinate system of the crystallographic unit cell in a matrix form:

$$\mathbf{A}^{(1)} = \begin{pmatrix} 0 & p & p \\ p & 0 & p \\ p & p & 0 \end{pmatrix} \tag{7.8}$$

for a site having $\bar{3}$ in [111] direction. Applying equation 3.10 then produces different forms of tensor $\mathbf{A}$, i.e. $\mathbf{A}^{(2)}$, $\mathbf{A}^{(3)}$, $\mathbf{A}^{(4)}$, corresponding to the

magnetically nonequivalent octahedral sites:

$$\begin{aligned}
\mathbf{A}^{(2)} &= \begin{pmatrix} 0 & p & -p \\ p & 0 & -p \\ -p & -p & 0 \end{pmatrix}, \\
\mathbf{A}^{(3)} &= \begin{pmatrix} 0 & -p & p \\ -p & 0 & -p \\ p & -p & 0 \end{pmatrix}, \\
\mathbf{A}^{(4)} &= \begin{pmatrix} 0 & -p & -p \\ -p & 0 & p \\ -p & p & 0 \end{pmatrix}.
\end{aligned} \tag{7.9}$$

The direction of magnetization in $(0\bar{1}1)$ plane may be described by angle α, direction [100] identifies with $\alpha = 0°$ and [011] corresponding to $\alpha = 90°$. When substituted into the equation 3.11, tensors $\mathbf{A}^{(i)}$ yield four branches. However, for this particular plane of rotation, branches corresponding to tensors $\mathbf{A}^{(2)}$ and $\mathbf{A}^{(3)}$ coincide, and as a consequence, only three different angular dependences appear:

$$\begin{aligned}
B^{(1)} &= B_{\text{iso}} + p\sin^2\alpha + p\sqrt{2}\sin 2\alpha, \\
B^{(2,3)} &= B_{\text{iso}} - p\sin^2\alpha, \\
B^{(4)} &= B_{\text{iso}} + p\sin^2\alpha - p\sqrt{2}\sin 2\alpha.
\end{aligned} \tag{7.10}$$

These equations were used to fit the experimental and calculated data in order to obtain the components of tensor $\mathbf{A}$. See Fig. 7.15 for an example of such fit. The description of angular dependences using power series approximation sufficiently matches the experimental and calculated data. The values of parameter p in units of Tesla were obtained from fits of the experimental and calculated dependences as -0.63 ± 0.09 and -0.23 ± 0.03, respectively.

7.2 Manganese Ferrites with Varying Manganese Content

Following text aims at studying series of manganese ferrite $Mn_xFe_{3-x}O_4$ samples ($x = 0.52$, 0.84, 0.95, 1.00, 1.10, 1.25, 1.58, 1.80) using ^{57}Fe NMR method. Despite being defined for $x = 1$, the idea of degree of inversion, as the amount of Mn and Fe pairs that are swapped between the sublattices, remains valid even for compounds with $x \neq 1$. While for $x \geq 1$, degree of

inversion y denotes the amount of iron in the A sites, for $x \leq 1$, y gives the amount of manganese in the B sites.

^{57}Fe NMR spectra of single crystals $Mn_xFe_{3-x}O_4$ measured in zero external magnetic field at 4.2 K are displayed in Fig. 7.16. In accordance with NMR results in the previous chapter (section 7.1.1), all spectra clearly exhibit two resonance lines (e.g. 71.07 and 68.66 MHz for $x = 1.00$ sample) which are assigned to the iron nuclei at B sites. The ratio of integral intensities of B lines matches 1:3, which is expected from the splitting due to anisotropy of hyperfine field (details described in chapter 3).

In addition to B_1 and B_2 lines, spectra of samples with $x \leq 1.10$ include third resolved line at higher frequencies (e.g. 71.90 MHz for $x = 1.00$ sample). This line corresponds to the resonance of iron nuclei at tetrahedral A sites as was evidenced in previous section 7.1.1. For the series of samples with various Mn content x, the intensity of A line increases with decreasing x (Fig. 7.16), which further supports the assignment of the resonance lines.

The frequency splitting of B lines does not depend on manganese content x within the experimental error (Fig. 7.17) and neither does the value of parameter β (from equation 3.12), see Table 7.7. Resonant lines of B_1 and B_2 sites hardly change their positions for $0.84 \leq x \leq 1.25$. For the lowest content of manganese, $x = 0.52$, the lines shift to higher frequencies while for the Mn rich samples ($x = 1.58$ and $x = 1.80$) the frequencies slightly decrease. Beside the frequency shifts with x, it is also evident that the spectra of samples $0.84 \leq x \leq 1.25$ exhibit relatively narrow lines, in comparison with samples having x outside of this range.

The origin of these frequency shifts and line broadening may be explained when the arrangement on neighbouring cationic sites is taken into account. For values of x close to 1, the concentration of Fe(A) or Mn(B) is quite low as it is created by the inversion only. Therefore, the probability of "normal spinel" surroundings corresponding to the main line, i.e. all six nearest A sites occupied by Mn atoms or all six nearest B sites occupied by Fe atoms, is higher than probabilities of single or even multiple occurrences of the Fe(A) or Mn(B) in the nearest neighbourhood. Such situation may be observed in the spectra of samples $0.95 \leq x \leq 1.10$ (Fig. 7.16), where only small part of resonating nuclei in the B sites experience different hyperfine fields due to one Fe(A) or Mn(B) present in the nearest neighbourhood. As a consequence, a weak satellite line appears in the vicinity of the B_1 line at frequency ~ 69 MHz.

However, as the manganese content x decreases, the concentration of Fe in the A sublattice increases (as it is indicated by the intensity of Fe(A)

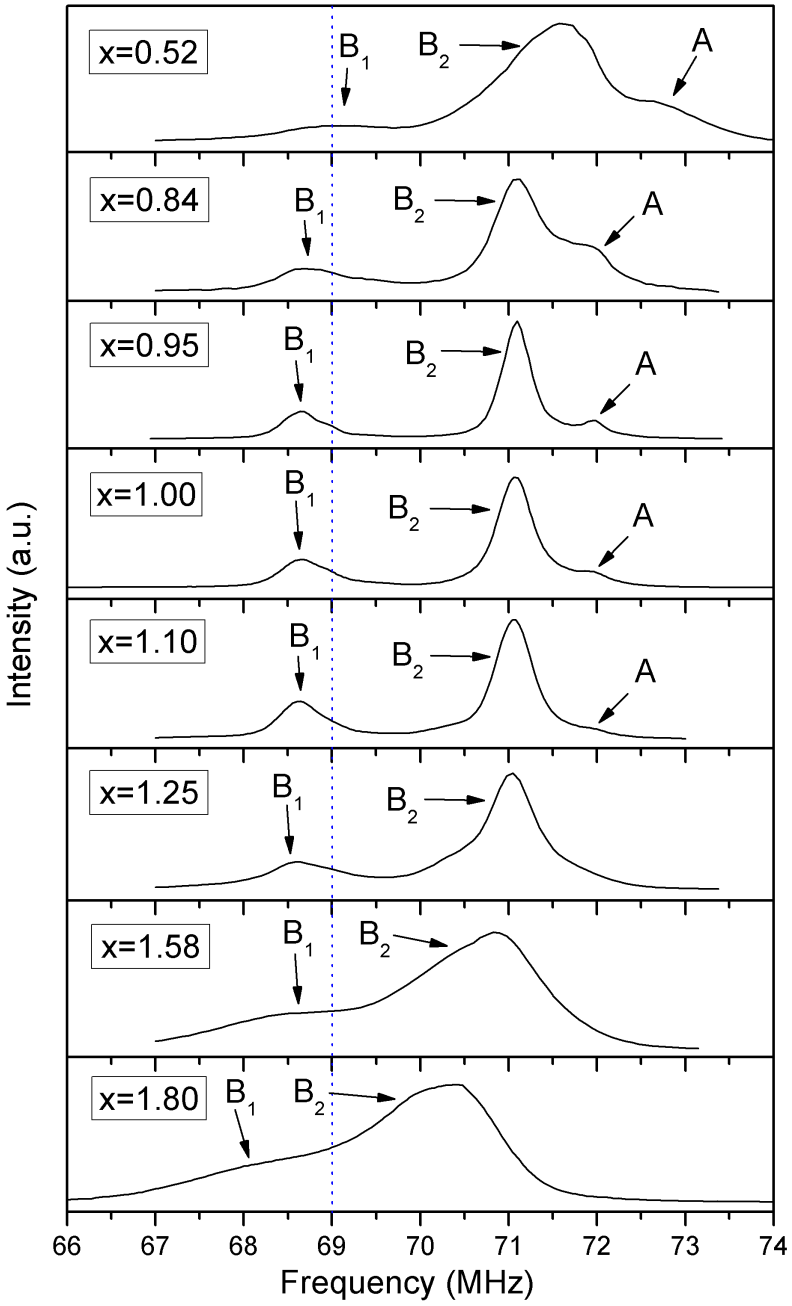

Figure 7.16: ^{57}Fe NMR spectra of eight single crystals $Mn_xFe_{3-x}O_4$ measured in zero external magnetic field at 4.2 K. Blue vertical line denotes the position of a weak satellite line resolved in the vicinity of the B_1 at ~ 69 MHz for $x = 1.00$.

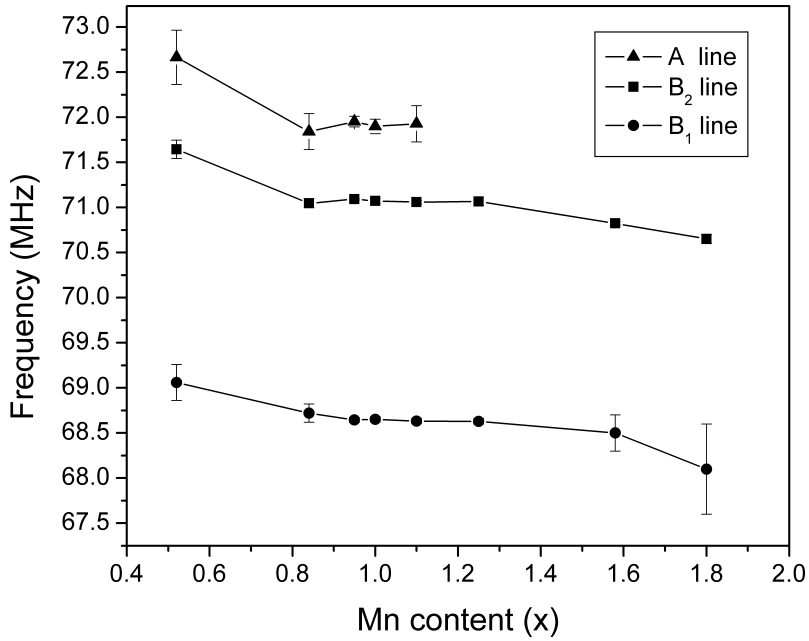

Figure 7.17: Dependence of ^{57}Fe line positions on Mn content x in zero external magnetic field at 4.2 K.

line); the concentration of Mn(B) is relatively small compared to concentration of Fe(A), and so only effects of Fe(A) may be considered. For high concentration of Fe(A), the probability that the six nearest A sites to a resonating Fe(B) are occupied by manganese becomes negligible, whereas the probability of one or more Fe(A) ion present in the neighbourhood rapidly increases. The frequency shift induced by one Fe ion is quite low; however, the shift will increase when more ions are introduced into the nearest neighbourhood. And e.g. for $x = 0.52$, the majority of the resonating nuclei in the B sites has several Fe(A) neighbours, as a consequence, the B lines then appear shifted to higher frequencies.

The situation for $x > 1$ seems analogous, though now the frequency shift is induced by Mn(B), whose concentration increases with x. Again, influence of the other type of cation, Fe(A), may be neglected as it is evidenced by the vanishing of the Fe(A) line for $x > 1.25$. Similarly to previous scenario, when the concentration of Mn(B) reaches high values, almost all Fe(B) nuclei are influenced by presence of several Mn(B) atoms in the nearest neighbourhood. In this case, the frequency shift induced by Mn(B) is opposite to that one induced by Fe(A).

Mn content (x)	B lines splitting (MHz)	parameter β (MHz)
1.80	2.60 ± 0.20	0.990 ± 0.080
1.58	2.33 ± 0.04	0.872 ± 0.015
1.25	2.44 ± 0.02	0.913 ± 0.009
1.10	2.43 ± 0.02	0.911 ± 0.007
1.00	2.42 ± 0.02	0.908 ± 0.008
0.95	2.45 ± 0.01	0.918 ± 0.005
0.84	2.33 ± 0.05	0.873 ± 0.018
0.52	2.58 ± 0.04	0.969 ± 0.014

Table 7.7: Frequency splitting of B lines in manganese ferrites $Mn_xFe_{3-x}O_4$.

7.3 Summary of Manganese Ferrite Results

In this chapter the main resonance lines of ^{57}Fe NMR spectrum were unambiguously assigned to iron nuclei in corresponding crystallographic positions. The assignment was supported by measurements in external magnetic field and by analysing the series of samples with gradually varying degree of inversion or manganese content. We confirm that the magnetic structure complies with the Goodenough-Kanamori-Anderson rules, i.e. all moments within a given sublattice are parallel and the total magnetizations of sublattices are mutually antiparallel.

We measured and analyzed the NMR spectra of sample series with various degrees of inversion y and found a systematic difference in values of y obtained from NMR from those obtained by other methods (neutron diffraction, magnetization measurements). A conclusion was drawn that the distribution of inverted iron atoms in the A sublattice is not entirely random. This was supported by calculations of manganese ferrite electronic structure, that have shown that a pairing of Fe(A)-Mn(B) is energetically favourable. By calculating the density of states we have also demonstrated that applying GGA+U opens the insulating gap in the band structure of manganese ferrite.

Chapter 8

Results on Lithium Ferrite

The following chapter concerns study of ordered lithium ferrite using ^{57}Fe NMR spectroscopy and *ab initio* calculations of its electronic properties. Results of calculations, namely the anisotropies of hyperfine field at ^{57}Fe nuclei, are obtained and analyzed. Based on their comparison with experimental data, an assignment of ^{57}Fe NMR resonance lines to crystallographic positions is presented. Also the resonance of ^{7}Li isotope is suggested and discussed on account of calculated hyperfine parameters.

8.1 ^{57}Fe NMR in Lithium Ferrite

Single crystal of the ordered $Li_{0.5}Fe_{2.5}O_4$ sample was granted by Dr. V. D. Doroshev (Donetsk Physicotechnical Institute). The sample was grown by the spontaneous crystallization method from a solution of the molten salt [69]. Content of ^{57}Fe isotope was natural, and the ordered state of the sample was guaranteed by the cooling conditions.

Spectrum was measured at 4.2 K using the Carr-Purcell pulse sequence, and excitation conditions were carefully set to obtain NMR signal from nuclei in magnetic domains. The spectrum comprises of two subspectra: two lines, split with ratio 6:2, that originate from tetrahedral A sites, and three lines (ratio 3:3:6) arising from octahedral B sites (Fig. 8.1). The numbers and intensities of the lines reflect the local symmetry of the crystallographic sites of ordered lithium ferrite (see Table 2.1) and the fact that the magnetization lies in direction $\langle 111 \rangle$ in zero external magnetic field. It is in agreement with former NMR experiments on ordered lithium ferrite [29, 30]

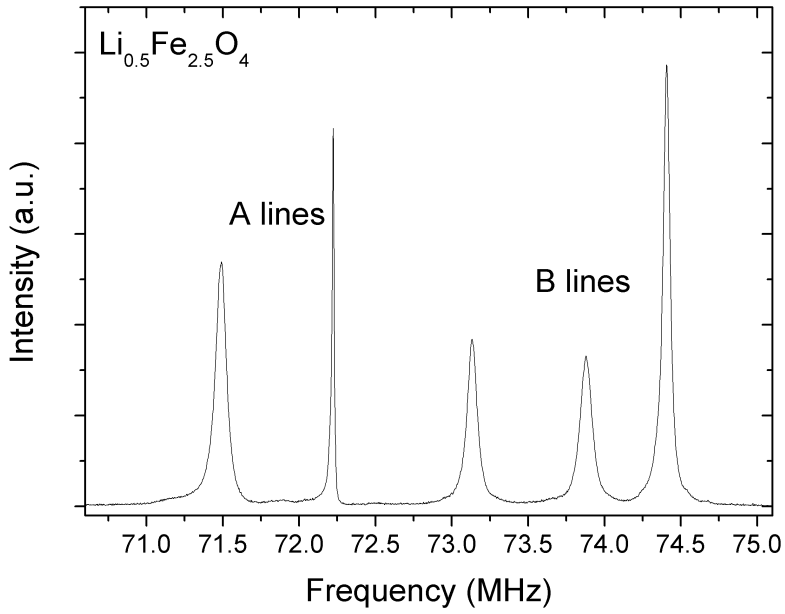

Figure 8.1: ^{57}Fe NMR spectrum of $Li_{0.5}Fe_{2.5}O_4$ single crystal at zero external magnetic field and 4.2 K.

although it provides better frequency resolution than the older works, which utilize the amplitude of echo signal to obtain the NMR spectrum.

8.2 Calculation of Electronic Structure of Lithium Ferrite

The structure of lithium ferrite containing 56 atoms in the unit cell was compiled from data in [70]. Such unit cell consists of eight formula units, i.e. it can be denoted as $(Fe_8)[Li_4Fe_{12}]O_{32}$. The structure was subjected to the process of minimization of free internal parameters and optimization of lattice parameter using WIEN2k with GGA method (PBE [62]). SIC [54] double counting scheme for irons was used ($U_{\text{eff}} = 4.5$ eV, $J = 0$ eV). Parameters used for the calculation are summarized in Table 8.1.

Lattice constant and internal structural parameters, obtained from volume optimization and minimization of internal positions, were compared with the experimental data, a structure refinement of lithium ferrite [71]. There is a noticeable difference (see Table 8.2) between experimental and

compound	Fe radius (a.u.)	Li radius (a.u.)	O radius (a.u.)	matrix size (RK_{max})	k-points (division)	G_{max}
(Fe_8) $[Li_4Fe_{12}]O_{32}$ (without s-o)	1.8	1.7	1.6	7419 (7.0)	10 (5 5 5)	14
(Fe_8) $[Li_4Fe_{12}]O_{32}$ (s-o)	1.8	1.7	1.6	4048 (6.0)	40 (4 4 4)	14

Table 8.1: Parameters used for calculations of lithium ferrite are displayed. RK_{max} denotes $RMT_{min} \times K_{max}$. 1 a.u. = 0.0529177 nm.

	lattice parameter (nm)	Li–O distance (nm)	Fe(B)–O distances (nm)	Fe(A)–O distances (nm)
experimental	0.83339(1)	0.2109(1)	0.19586(9) 0.20152(9) 0.20652(10)	0.18848(10) 0.1914(2)
calculation	0.84423	0.21374	0.19840 0.20513 0.20910	0.19029 0.19394
ratio of calculated and experimental parameter	1.0130	1.0135	1.0130 1.0179 1.0125	1.0096 1.0133

Table 8.2: Experimental lattice parameter and nearest neighbour distances are compared with the results calculated ab initio. Bottom row shows ratio between parameters obtained from these two methods.

calculated lattice parameters (1.3%), more commonly expressed as a difference in unit cell volume (4%). Such discrepancy is expected, because GGA is well known to overestimate the volume by 2–4%. The gradient correction acts as an isotropic negative pressure, and thus favours volume expansion, while e.g. LDA usually underestimates the volume by $\sim 3\%$ [72, 73, 74].

In addition to structural parameters, the values of hyperfine parameters were extracted from the calculations. Results for isotopes, which are of the interest for NMR measurements, are summarized in Table 8.3. One should notice the substantial errors in calculated contact hyperfine fields on iron nuclei, as was detailed in chapter 6. The transferred magnetic hyperfine field in case of lithium or the parameters of electric quadrupolar interaction are not burdened by such errors and may be used in further analysis. Beside the isotropic contact hyperfine field, the terms contributing to anisotropy of hyperfine interaction were calculated. Their analysis and comparison with experiment are elaborated in the following text.

nucleus	nuclear spin	experiment $\lvert B_{hf}\rvert$ (T)	contact term B_{hf} (T)	V_{zz} (10^{-21} Vm^{-2})	η
^{57}Fe(A)	1/2	52.051	−34.9	−1.10	0.36
^{57}Fe(B)	1/2	53.706	36.5	1.73	0
^{7}Li(B)	3/2		−0.095	0.07	0

Table 8.3: Calculated contact hyperfine fields and parameters of electric quadrupolar interaction are displayed. Despite nonzero values of EFG tensor, there is no manifestation of quadrupole interaction in ^{57}Fe NMR spectra, since the spin of this nucleus is 1/2 in ground state. The experiment provides the absolute value of B_{hf}.

8.3 Hyperfine Field Anisotropy in Lithium Ferrite

In order to calculate the anisotropic contributions to the hyperfine field, the spin-orbit interaction (s-o) was included. The calculation was started from results of a fully converged calculation performed without s-o by lowering the symmetry to comply with any direction of magnetization in the $(0\bar{1}1)$ plane. Choice of the plane was the same as that one used in measurements of ^{57}Fe NMR spectra anisotropy [30] to allow direct comparison. This setting (magnetization in $(0\bar{1}1)$ plane) increased the total number of non-equivalent atom types in the unit cell from 5 to 30: crystallographically equivalent tetrahedral iron sites split into four magnetically nonequivalent sorts (each with a multiplicity 2), while the octahedral iron sites gave rise to seven magnetically nonequivalent sorts (in numbers 1, 2, 1, 2, 2, 2 and 2).

During the calculation the s-o interaction is diagonalized in the space of the scalar relativistic eigenstates, therefore, the energy window was increased (from 2.0 Ry to 4.0 Ry) to include additional eigenstates. The evaluation of hyperfine field anisotropy contributions ΔB_{hf}^{orb} and ΔB_{hf}^{dip} was performed both ways, using self-consistent s-o SCF calculation and by calculating with just one s-o iteration. Comparison of these two methods displayed in Fig. 8.2 reveals that the two approaches lead to the same results. With direction of magnetization contained within the $(0\bar{1}1)$ plane, two of the A lines should coincide due to symmetry reasons, which is not fully reproduced in the calculated dependence. Slight splitting of the doubled curve corresponding to line A2 in Fig. 8.2 thus provides an estimate of the calculation accuracy.

Detailed insight of the particular contributions to the calculated aniso-

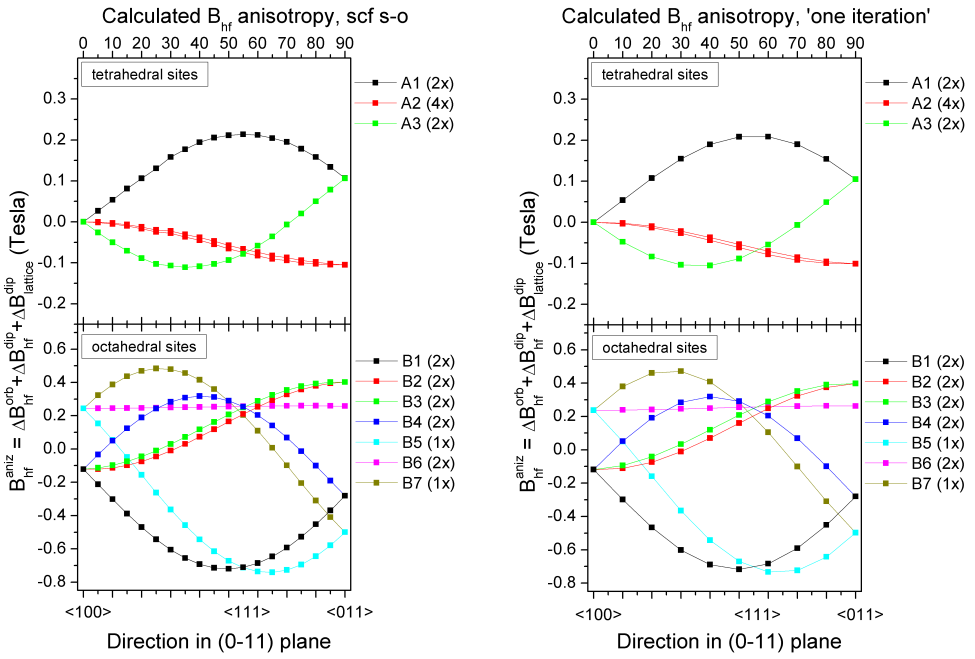

Figure 8.2: Calculated anisotropy of hyperfine field on ^{57}Fe nuclei in tetrahedral and octahedral sites of lithium ferrite is shown. Figure compares results obtained from self-consistently converged s-o calculation and from calculation with just one s-o iteration after converged calculation without s-o. Only anisotropic parts of $B_{\rm hf}^{\rm orb}$ and $B_{\rm hf}^{\rm dip}$ were included. Labelling of the curves was chosen in such way to correspond to notation used by Doroshev *et al.* [30], numbers in parentheses denote multiplicity of a given curve.

tropy, $B_{\rm hf}^{\rm orb}$, $B_{\rm hf}^{\rm dip}$, and $B_{\rm lattice}^{\rm dip}$ is displayed in Fig. 8.3. Firstly, it can be seen that for tetrahedral sites the dipolar term of the hyperfine field, $B_{\rm hf}^{\rm dip}$, is dominant, whereas for octahedral sites it is rather dipolar field of neighbouring ions, $B_{\rm lattice}^{\rm dip}$, that plays an important role. Although the orbital part of the hyperfine field, $B_{\rm hf}^{\rm orb}$, has relatively high value, its variation with the change of magnetization seems to be quite insignificant. In principle, both $B_{\rm hf}^{\rm orb}$ and $B_{\rm hf}^{\rm dip}$ have non-zero isotropic parts $B_{\rm hf}^{\rm orb}$(iso) and $B_{\rm hf}^{\rm dip}$(iso), which were subtracted when comparing the total anisotropy with the experiment. In further text, only the anisotropic parts

$$\begin{aligned} \Delta B_{\rm hf}^{\rm orb} &= B_{\rm hf}^{\rm orb} - B_{\rm hf}^{\rm orb}({\rm iso}), \\ \Delta B_{\rm hf}^{\rm dip} &= B_{\rm hf}^{\rm dip} - B_{\rm hf}^{\rm dip}({\rm iso}), \\ \Delta B_{\rm lattice}^{\rm dip} &= B_{\rm lattice}^{\rm dip}, \end{aligned} \tag{8.1}$$

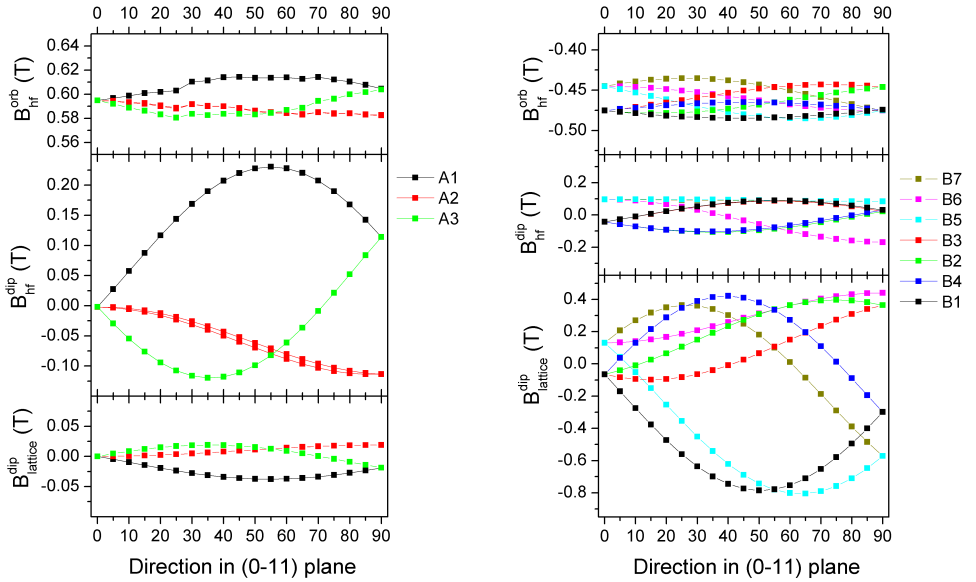

Figure 8.3: The individual contributions to the calculated anisotropy of ^{57}Fe NMR, $B_{\rm hf}^{\rm orb}$, $B_{\rm hf}^{\rm dip}$, and $B_{\rm lattice}^{\rm dip}$, are displayed for the tetrahedral and octahedral sites. Note, that the scale of $\Delta B_{\rm hf}^{\rm orb}$ plot is different.

were considered ($B_{\rm lattice}^{\rm dip}({\rm iso}) = 0$). Apparently, the particular contributions $\Delta B_{\rm hf}^{\rm orb}$, $\Delta B_{\rm hf}^{\rm dip}$, and $\Delta B_{\rm lattice}^{\rm dip}$ have often different signs, and as a consequence, partially cancel out in some cases. Additionally, unfolding the dependences into individual components revealed that the slight splitting of A_2 dependence originated because of the dipolar term $B_{\rm lattice}^{\rm dip}$.

Angular dependence of ^{57}Fe NMR spectra at both tetrahedral and octahedral sites of ordered lithium ferrite was acquired experimentally by V. D. Doroshev *et al.* [30], using a sphere shaped sample, oriented by a magnetic method. Spectra were measured in external magnetic field 0.266 T, which was applied in a plane of (011) type. For sake of comparison with the calculated anisotropy (see Fig. 8.4), we rescaled these data into units of Tesla and subtracted the isotropic parts (52.15 T for A sites and 53.57 T for B sites).

For the octahedral sites the calculated dependences of hyperfine field on direction of magnetization are included within the interval (-0.75, 0.48) in units of Tesla, which matches with the interval (-0.75, 0.41) of the experimental data. Such agreement was not reached for tetrahedral sites, where the calculated curves are found within a range of $\sim$ 0.32 T, while

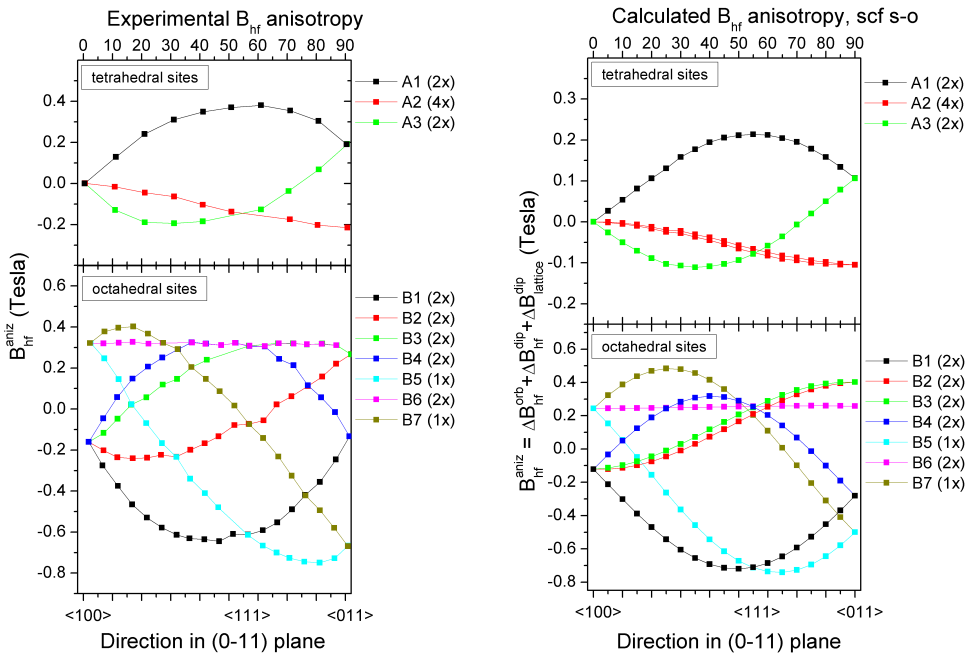

Figure 8.4: Experimental hyperfine field anisotropies derived from angular dependences of ^{57}Fe NMR spectra measured at 4.2 K in external magnetic field 0.266 T are compared with self-consistently calculated hyperfine field anisotropy for tetrahedral A sites (3 lines) and octahedral B sites (7 lines) in the $P4_332$ structure for direction of magnetization in $(0\bar{1}1)$ plane. Both experimental and calculated fields were adjusted by subtracting their isotropic parts.

the experimental are in the range of ~ 0.59 T. The reason may lie in underestimation of calculated hyperfine parts ΔB_{hf}^{orb} and ΔB_{hf}^{dip}, analogous to problems with the contact field. Then the difference should be high for tetrahedral sites, where ΔB_{hf}^{dip} is dominant, while for anisotropy of octahedral sites, given mainly by $\Delta B_{lattice}^{dip}$, the difference should be small. On the other hand, such error is likely to be small, as can be seen on the behaviour of individual parts in the dependence B6 (Fig. 8.3). Even though the three individual terms of anisotropy change values with rotation of magnetization, their sum has almost constant character, in accordance with B6 curve in the experiment.

Most importantly, the calculated curves do reproduce the numbers of lines in particular directions correctly and are consistent with the experimental data to the extent that even an assignment of individual dependences

angular dependence	multiplicity	crystal coordinates (x = 0.49816, y = 0.63195)	
A1	2	(x, x, x)	$(-x+\frac{1}{4}, -x+\frac{1}{4}, -x+\frac{1}{4})$
A2	4	$(-x+\frac{1}{2}, -x, x+\frac{1}{2})$	$(x+\frac{3}{4}, -x+\frac{3}{4}, x+\frac{1}{4})$
		$(-x, x+\frac{1}{2}, -x+\frac{1}{2})$	$(x+\frac{1}{4}, x+\frac{3}{4}, -x+\frac{3}{4})$
A3	2	$(x+\frac{1}{2}, -x+\frac{1}{2}, -x)$	$(-x+\frac{3}{4}, x+\frac{1}{4}, x+\frac{3}{4})$
B1	2	$(-y+\frac{1}{4}, \frac{1}{8}, y)$	$(y, -y+\frac{1}{4}, \frac{1}{8})$
B2	2	$(y+\frac{3}{4}, \frac{5}{8}, -y+\frac{1}{2})$	$(-y+\frac{1}{2}, y+\frac{3}{4}, \frac{5}{8})$
B3	2	$(y+\frac{1}{4}, \frac{7}{8}, y+\frac{1}{2})$	$(-y, -y+\frac{3}{4}, \frac{3}{8})$
B4	2	$(-y+\frac{3}{4}, \frac{3}{8}, -y)$	$(y+\frac{1}{2}, y+\frac{1}{4}, \frac{7}{8})$
B5	1	$(\frac{1}{8}, y, -y+\frac{1}{4})$	
B6	2	$(\frac{7}{8}, y+\frac{1}{2}, y+\frac{1}{4})$	$(\frac{3}{8}, -y, -y+\frac{3}{4})$
B7	1	$(\frac{5}{8}, -y+\frac{1}{2}, y+\frac{3}{4})$	

Table 8.4: Assignment of the individual curves with the corresponding positions of the resonating nucleus in the crystal.

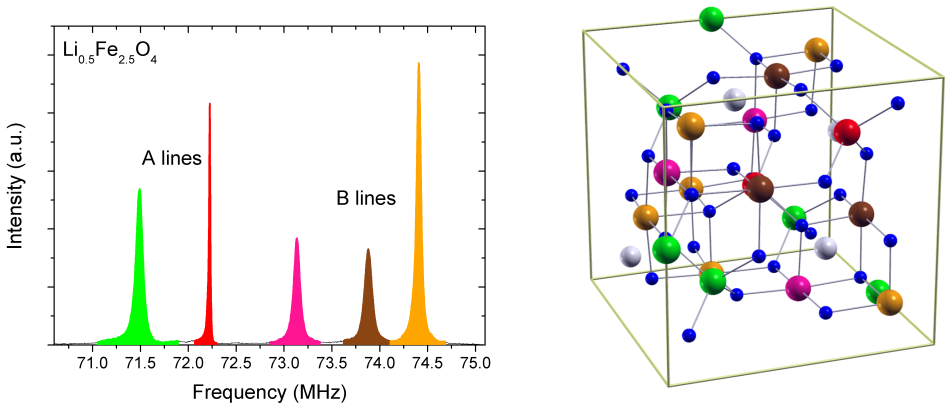

Figure 8.5: Direct assignment of the spectral lines to their corresponding positions in the crystal was enabled by comparison and analysis of the hyperfine field anisotropies. Gray and blue spheres represent lithium and oxygen atoms, remaining five colours correspond to resonance lines in the spectrum on left.

is possible. Table 8.4 itemizes the individual curves together in Fig. 8.4 with their corresponding positions in the crystal. Eventually, crystal positions may be ascribed to the lines in the zero-field ^{57}Fe NMR spectrum, see Fig. 8.5. Agreement of these two approaches shows that *ab initio* calculations of hyperfine field anisotropy might be useful in spectral line assignment also in more complicated compounds.

Besides, it should be noted that the experiment provides data with respect to direction of the external magnetic field, i.e. the magnetocrystalline anisotropy affects the data, while the calculation uses straightly the direction of magnetization. Therefore, the equilibrium direction of magnetization for the used external magnetic field (0.266 T) would have to be derived for the experimental data in order to allow more authentic comparison with the calculation.

8.4 Tensors of Hyperfine Field Anisotropy

In the following text, the anisotropies of hyperfine interaction are further compared and evaluated quantitatively. According to equation (3.9), the dependence of the hyperfine field on the direction of magnetization involves tensor of hyperfine field anisotropy $\mathbf{A}$, which in general is a second rank traceless symmetric tensor with five independent components. For tetrahedral site with position (x, x, x), i.e. nuclei that contribute to the dependence A1 (in Fig. 8.4), only one independent component remains (due to local symmetry C_3):

$$\mathbf{A_{tetra}} = \begin{pmatrix} 0 & p & p \\ p & 0 & p \\ p & p & 0 \end{pmatrix} \tag{8.2}$$

For the octahedral sites with local symmetry C_2 the tensor keeps three independent components, and e.g. for position (7/8, y + 1/2, y + 1/4) in the structure (dependence B6 in Fig. 8.4) the tensor reads:

$$\mathbf{A_{octa}} = \begin{pmatrix} -2t & r & r \\ r & t & s \\ r & s & t \end{pmatrix} \tag{8.3}$$

Tensor matrices of the other crystallographically equivalent sites were derived by using equation (3.10). For ordered lithium ferrite (space group $P4_332$), four different tensors were obtained for tetrahedral sites, $\mathbf{A}^{(1)}_{\text{tetra}}, \ldots, \mathbf{A}^{(4)}_{\text{tetra}}$, and twelve tensors for octahedral sites, $\mathbf{A}^{(1)}_{\text{octa}}, \ldots, \mathbf{A}^{(12)}_{\text{octa}}$. Introducing angle

α to describe the direction of magnetization in $(0\bar{1}1)$ plane ($\alpha = 0°$ for direction [100] and $\alpha = 90°$ for [011]), the substitution into equation (3.11) gave the individual branches of the angular dependences. Four tensors of the tetrahedral sites yielded three branches (one is double degenerated):

$$\begin{aligned} B^{(1)}_{\text{tetra}} &= B_{\text{iso}^{\text{tetra}}} + p\sin^2\alpha + p\sqrt{2}\sin 2\alpha, \\ B^{(2,3)}_{\text{tetra}} &= B_{\text{iso}^{\text{tetra}}} - p\sin^2\alpha, \\ B^{(4)}_{\text{tetra}} &= B_{\text{iso}^{\text{tetra}}} + p\sin^2\alpha - p\sqrt{2}\sin 2\alpha \end{aligned} \tag{8.4}$$

Similar procedure for the twelve tensors of octahedral sites produced seven different branches (since five of them are double degenerated):

$$\begin{aligned} B^{(1,2)}_{\text{octa}} &= B_{\text{iso}^{\text{octa}}} + t\cos^2\alpha - \frac{1}{2}(t-2r)\sin^2\alpha + \frac{1}{\sqrt{2}}(r+s)\sin 2\alpha, \\ B^{(3,4)}_{\text{octa}} &= B_{\text{iso}^{\text{octa}}} + t\cos^2\alpha - \frac{1}{2}(t-2r)\sin^2\alpha - \frac{1}{\sqrt{2}}(r+s)\sin 2\alpha, \\ B^{(5,6)}_{\text{octa}} &= B_{\text{iso}^{\text{octa}}} + t\cos^2\alpha - \frac{1}{2}(t+2r)\sin^2\alpha + \frac{1}{\sqrt{2}}(r-s)\sin 2\alpha, \\ B^{(7,8)}_{\text{octa}} &= B_{\text{iso}^{\text{octa}}} + t\cos^2\alpha - \frac{1}{2}(t+2r)\sin^2\alpha - \frac{1}{\sqrt{2}}(r-s)\sin 2\alpha, \\ B^{(9,10)}_{\text{octa}} &= B_{\text{iso}^{\text{octa}}} - 2t\cos^2\alpha + (t-s)\sin^2\alpha, \\ B^{(11)}_{\text{octa}} &= B_{\text{iso}^{\text{octa}}} - 2t\cos^2\alpha + (t+s)\sin^2\alpha + r\sqrt{2}\sin 2\alpha, \\ B^{(12)}_{\text{octa}} &= B_{\text{iso}^{\text{octa}}} - 2t\cos^2\alpha + (t+s)\sin^2\alpha - r\sqrt{2}\sin 2\alpha. \end{aligned} \tag{8.5}$$

These equations were used to fit the experimental and calculated data in order to obtain the components of tensors $\mathbf{A}_{\text{tetra}}$ and $\mathbf{A}_{\text{octa}}$. See Fig. 8.6 for an example of such fit. The description of angular dependences using power series approximation sufficiently matched the experimental and calculated data.

The values of parameters p, t, r and s are displayed in Table 8.5. Comparing the experimental and the calculated dependences is quite straightforward for tetrahedral sites, since there is only one independent component in tensor $\mathbf{A}$. However, in the octahedral case, using these parameters for comparison is rather cumbersome. A suitable invariant of the tensor $\mathbf{A}$, appropriately characterizing the anisotropic character, usually performs better; e.g. the symmetric anisotropy:

$$\begin{aligned} \Gamma &= \frac{1}{2}((A_{xx}-A_{yy})^2 + (A_{yy}-A_{zz})^2 + (A_{zz}-A_{xx})^2) \\ &+ \frac{3}{4}((A_{xy}+A_{yx})^2 + (A_{yz}+A_{zy})^2 + (A_{zx}+A_{xz})^2). \end{aligned} \tag{8.6}$$

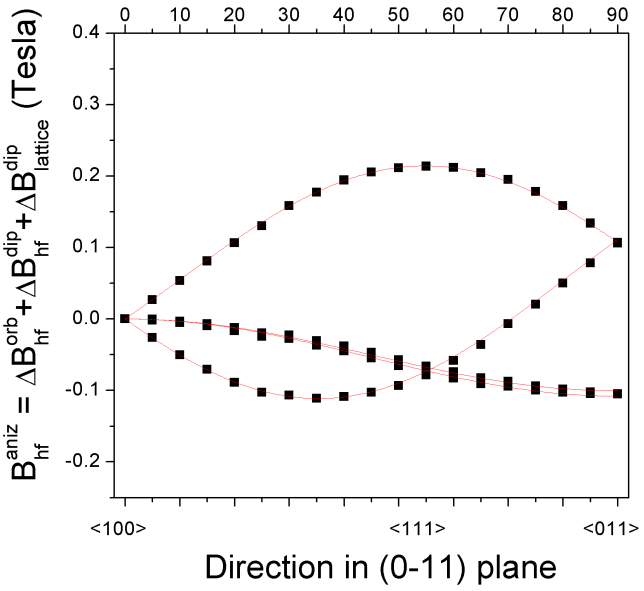

Figure 8.6: An example of fitting procedure for tetrahedral sites using the formulae for B_{tetra}.

parameter	p (T)	t (T)	r (T)	s (T)	Γ_{tetra} (T^2)	Γ_{octa} (T^2)
experiment	0.21 ± 0.03	-0.161 ± 0.001	-0.26 ± 0.08	-0.46 ± 0.09	0.38	1.29
calculation	0.107 ± 0.003	-0.122 ± 0.001	-0.34 ± 0.01	-0.36 ± 0.01	0.10	1.23

Table 8.5: Parameters p, t, r and s obtained from fits of the experimental and calculated dependences are displayed.

Γ may be rewritten as a combination of the first two invariants:

$$\Gamma = \frac{3}{2}\mathrm{Tr}[\mathbf{A}\cdot\mathbf{A}] - \frac{5}{2}[\mathrm{Tr}\mathbf{A}]^2, \tag{8.7}$$

which reduces to

$$\Gamma = \frac{3}{2}\mathrm{Tr}[\mathbf{A}\cdot\mathbf{A}], \tag{8.8}$$

since tensors $\mathbf{A}$ are traceless. Values of Γ_{tetra} and Γ_{octa} are shown in Table 8.5. The results for octahedral sites agree reasonably (5%), while invariants Γ differ significantly for tetrahedral sites.

8.5 Li NMR in Lithium Ferrite

In addition to ^{57}Fe spectral lines in the frequency range 71–75 MHz, another spectrum located at lower frequencies was detected. Roughly measured NMR spectrum consisted of a relatively intensive resonance line at ~ 10 MHz and a weaker band of lines in the range 8–20 MHz. Detailed assignment and interpretation of this spectrum from experiment would require additional measurements in various external magnetic field and at different temperatures. Yet an estimate may be proposed, based on the calculated hyperfine parameters and properties of nuclei present in the compound. Considering its nuclear properties, isotope ^{7}Li is the most probable candidate for NMR signal in this frequency range. Nuclear spin of ^{7}Li is 3/2, gyromagnetic ratio is $\gamma = 16.55$ MHz.T^{-1}, nuclear quadrupolar momentum $Q = -4.01 \times 10^{-28}$ m^2, and its natural abundance is 92%. Calculated hyperfine magnetic field in the lithium site was $B_{\mathrm{hf}} = -0.095$ T, and the main component of electric field gradient tensor $V_{zz} = 0.0676 \times 10^{-21}$ Vm^{-2}. Asymmetry η is zero due to presence of trigonal axis. Analogously to the NMR spectra of octahedral iron, there are two magnetically nonequivalent lithium sites with ratio 1:3 for magnetization in direction $\langle 111 \rangle$, which leads to two different values of lattice dipolar field $B^{\mathrm{dip}}_{\mathrm{lattice}}$: field 1.07 T for the site with local axis parallel with direction of magnetization and -0.36 T for the other three sites.

Both electric and magnetic hyperfine interactions were of comparable magnitude, which made necessary to solve the eigenvalue problem of the total interaction Hamiltonian. The diagonalization was carried out separately for the two lithium sites that differ by the total magnetic field and by mutual direction of electric and magnetic fields. The eigenvalues, obtained in the process, correspond to resonance frequencies of observable transitions, and the wave functions may be used to evaluate the probability of each transition using the first-order perturbation theory. Simulated spectrum was created as a superposition of Pearson curves (Lorentzian^2) at calculated frequencies with the amplitudes proportional to the transition probabilities and with line widths related to experimental lines (~ 1 MHz). Comparison of experimental and simulated ^{7}Li NMR spectra is displayed in Fig. 8.7. Although the spectra do not exactly match each other, the agreement of spectral ranges may be used to support the assignment of the spectrum to ^{7}Li resonance. It should be noted, that it was not possible to measure below 6 MHz owing to limitations of the NMR spectrometer.

Contribution of ^{6}Li isotope can be neglected considering its low natural

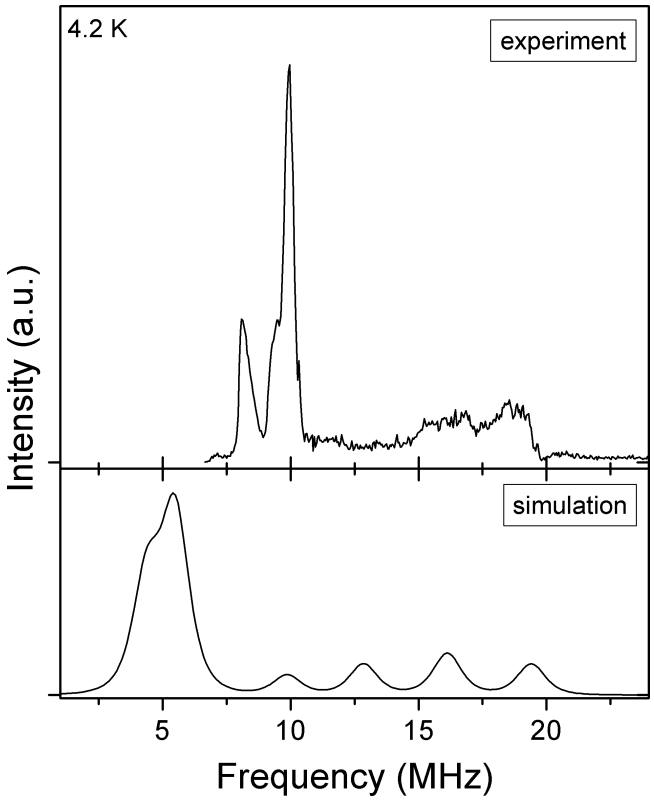

Figure 8.7: Top: Experimental NMR spectrum, assigned to resonance of ^{7}Li isotope, was measured at 4.2 K in zero external magnetic field. Bottom: ^{7}Li NMR spectrum was simulated from the calculated hyperfine parameters.

abundance. It also has lower values of gyromagnetic and quadrupolar momenta than ^{7}Li, which would presumably place its NMR resonance below the frequencies of the measured spectrum. Resonance of ^{17}O was detected by Kovtun *et al.* [19] at 47.6 and 48.6 MHz, therefore, it can be also ruled out.

8.6 Summary of Lithium Ferrite Results

Anisotropy of hyperfine fields on iron nuclei was derived from the series of *ab initio* calculations of electron structure of lithium ferrite. Comparison of calculated anisotropy with experimental dependences of ^{57}Fe NMR spectra on direction of external magnetic field allowed to assign unambiguously the individual lines in the ^{57}Fe NMR spectra to crystal positions. We acquired additional NMR spectrum at lower frequencies, and assigned it to ^{7}Li resonance, based on calculated hyperfine fields.

Chapter 9

Results on Magnetites

NMR spectroscopy is one of the most suitable experimental techniques for studying the low temperature phase of magnetite Fe_3O_4 with the aim to understand the electronic structure. The method is the only one that clearly distinguishes all crystallographically (and magnetically) nonequivalent iron sites in the ^{57}Fe spectrum. Despite extensive effort, both experimental and theoretical, the crystallographic sites (tetrahedral and octahedral, A and B) are attributed only to groups of spectral lines, but the assignment of an individual spectral line to a particular crystal position is yet unknown. The absence of accurate assignment of NMR spectrum is caused mainly by two factors: the overall complexity of magnetite structure below the Verwey transition and the lack of complementary experimental method.

The chapter is devoted to three different areas concerning magnetite. The first part involves calculations of hyperfine fields and their comparison with experiment. The idea behind lies in matching the experimental and calculated properties: in section 9.1 the dependences of hyperfine fields on the direction of external magnetic field are compared.

Two other parts are rather based on experimental approach. The static spectrum is far from being the only output NMR provides. Further information may be extracted e.g. from observation of dynamic processes under certain conditions, from relaxation of NMR signal, by studying effects connected with domain structure, or by introducing defects or substitutions and studying their effect. Section 9.2 is concerned with switching of magnetic easy axis induced by external magnetic field and accompanying structural changes, and section 9.3 relates cationic defects (vacancies) in magnetite

sample	notation	preparation
Fe_3O_4	001	skull melter
Fe_3O_4	111	skull melter
Fe_3O_4	00S	skull melter
Fe_3O_4	B	floating zone
$Fe_{3.0000}O_4$	0000	skull melter
$Fe_{2.9925}O_4$	0025	skull melter
$Fe_{2.9895}O_4$	0035	skull melter
$Fe_{2.9865}O_4$	0045	skull melter
$Fe_{2.9859}O_4$	0047	skull melter
$Fe_{2.9838}O_4$	0054	skull melter
$Fe_{2.9829}O_4$	0057	skull melter
$Fe_{2.9820}O_4$	0060	skull melter
$Fe_{2.9802}O_4$	0066	skull melter
$Fe_{2.9769}O_4$	0077	skull melter
$Fe_{2.9730}O_4$	0090	skull melter
$Fe_{2.98}Al_{0.02}O_4$	Al:Fe_3O_4	floating zone
$Fe_{2.95}Ga_{0.05}O_4$	Ga:Fe_3O_4	floating zone
$Fe_{2.992}Ti_{0.008}O_4$	Ti:Fe_3O_4	floating zone

Table 9.1: Studied single crystal magnetite samples with their nominal composition are listed.

and their effect on electronic structure.

9.0.1 Studied Samples

Stoichiometric purity of magnetite is crucial factor influencing most of the observable properties. High quality single crystal magnetite samples of various compositions used in this work were prepared by means of floating zone technique (group of Dr. V. A. M. Brabers, Technical University of Eindhoven) or from the melt using the cold crucible technique (group of Prof. J. M. Honig, Purdue University; some samples were further treated by Prof. Z. Kąkol and Prof. A. Kozłowski, AGH University in Kraków).

In case of floating zone, a very pure crystal is prepared from iron oxide, which is obtained from the decomposition of pure iron oxalate. Skull-melter prepared, high quality samples were grown from pure Fe_2O_3 and subjected to subsolidus annealing under CO/CO_2 gas mixtures to establish the appropriate metal/oxygen ratio, and then rapidly quenched to room temperature to freeze in the high temperature thermodynamic equilibrium. Sample 00S was ground to the spherical shape 3 mm in diameter for the purpose of

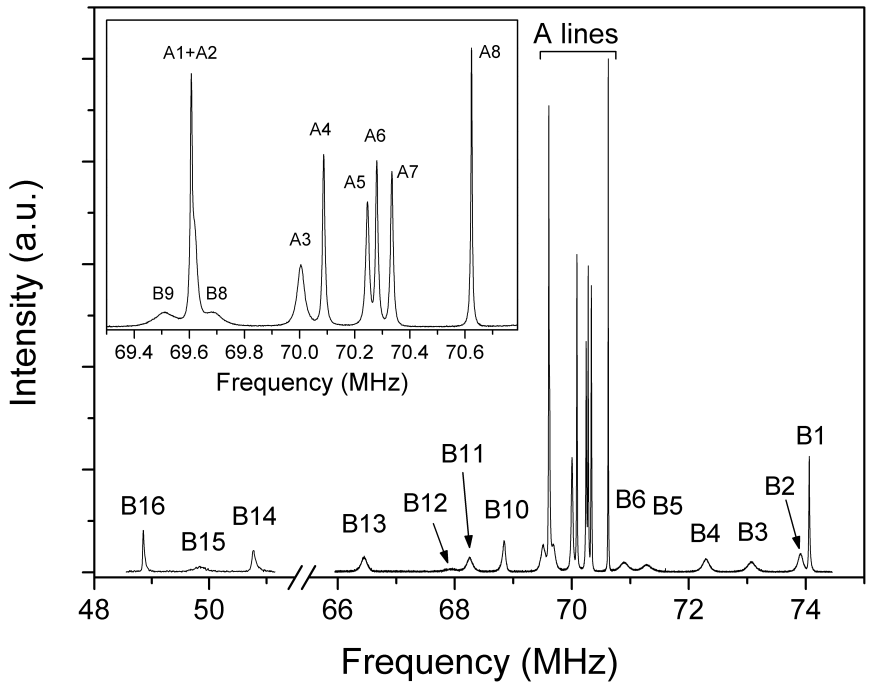

Figure 9.1: Example of ^{57}Fe NMR spectrum of magnetite Fe_3O_4, high quality single crystal sample 0000, was measured in zero external magnetic field at 4.2 K. Spectral intensities were not corrected with respect to frequency dependence. Line B7 is hidden beneath the A subspectrum.

measurement in external magnetic fields. All magnetite samples studied in this work are summarized in Table 9.1

9.1 Hyperfine Fields in Magnetite

Above T_V the symmetry of magnetite crystal structure is cubic and the NMR spectrum is simple, consisting of one A line, that corresponds to tetrahedral irons, and of B subspectrum, originating in the octahedral sites. The B subspectrum reflects the direction of magnetization, and is therefore split into two lines (1:3) above the temperature of reorientation transition ($T_R \sim 130$ K stoichiometric magnetite), where the magnetization lies in the $\langle 111 \rangle$ direction, while for direction $\langle 100 \rangle$ ($T_V < T < T_R$) the subspectrum consists of a single B line.

Below T_V the NMR spectrum is composed of eight A lines and sixteen B lines, in accordance with Cc space group. Due to its complex character, the ^{57}Fe NMR spectrum below temperature of the Verwey transition T_V indicates the quality and stoichiometric purity of a magnetite sample. Particularly, there are several features observed by NMR, that can be used as an evaluation of the magnetite sample. Spectral line widths are the most noticeable feature, especially for the A lines which may be very narrow for a high quality sample (see Fig. 9.1): e.g., monitoring the shape of two accidentally overlapping A lines, that lie lowest in the frequency (lines A1+A2, at 69.607 MHz). Also the relaxations express some information on sample purity, as very good samples tend to have e.g. the spin-lattice relaxation times in seconds or even tens of seconds.

9.1.1 Hyperfine Field Anisotropy in Magnetite

In this section the anisotropy of hyperfine field in low temperature phase of magnetite Fe_3O_4 is studied by using the *ab initio* calculations. Calculated anisotropies are then compared to experimental NMR data of M. Mizoguchi [33]. Although the monoclinic Cc is recognized so far as the true symmetry of magnetite below the Verwey transition, the low temperature structure was refined only in a smaller monoclinic P2/c symmetry cell, which was therefore used in our calculations. Crystallographic unit cell with P2/c symmetry, $(Fe_8)[Fe_{16}]O_{32}$, has only two non-equivalent tetrahedral A sites (compared to eight sites in Cc) and six non-equivalent octahedral B sites (while Cc has sixteen B sites). The structural parameters used for the calculation were taken from neutron diffraction data of Wright *et al.* [34], and were minimized with respect to energy and atomic forces. For the exchange-correlation functional the generalized gradient approximation of Perdew-Burke-Ernzerhof [62] was employed, with SIC scheme [54] using parameters $U = 7.5$ eV and $J = 1.4$ eV. Other important parameters are displayed in Table 9.2.

The spin-orbit interaction (s-o) was included in the calculations in order to allow complying of magnetization to crystal lattice. First the calculation without s-o was carried to self-consistency, then the symmetry was reduced taking directions of $\mathbf{M}$ into account. The experiment (Mizoguchi [33]) was carried out with external magnetic field of 1.3 T rotated step by step in three perpendicular planes (ac), (ab), and (bc), where a, b and c are magnetically hard, intermediate and easy axes of magnetite. Energetic difference between a state with magnetization in hard and magnetization in easy axis is quite

compound	Fe radius (a.u.)	O radius (a.u.)	matrix size (RK_{max})	k-points (division)	G_{max}
$(Fe_8)[Fe_{16}]O_{32}$ (without s-o)	2.0	1.5	4145 5.7	18 (2 6 6)	14
$(Fe_8)[Fe_{16}]O_{32}$ (s-o)	2.0	1.5	4145 5.7	36 (2 6 6)	14

Table 9.2: Parameters used for calculations of magnetite P2/c. RK_{max} denotes $RMT_{min} \times K_{max}$. 1 a.u. = 0.0529177 nm.

high in magnetite. Therefore, it is expectable that while in the experiment the external magnetic was rotated within the given plane, the actual path of magnetization was somewhat different, especially when approaching the hard axis.

In order to derive the direction of magnetization for directions and magnitude of external field used by Mizoguchi ($|\mathbf{B}| = 1.3$ T), we used the results of magnetocrystalline anisotropy measurements in low temperature phase of magnetite obtained by K. Abe *et al.* [75] at 4.2 K: $K_a = 25.5$, $K_b = 3.7$, $K_u = 2.1$, $K_{aa} = 1.8$, $K_{bb} = 2.4$ and $K_{ab} = 7.0$ in 10^4 J/m^3. Directions of magnetization in dependence on orientation of $\mathbf{B}$ were then found by minimizing the energy:

$$E_a = -\mathbf{M}\cdot\mathbf{B} + K_a\alpha_a^2 + K_b\alpha_b^2 + K_{aa}\alpha_a^4 + K_{bb}\alpha_b^4 + K_{ab}\alpha_a^2\alpha_b^2 - K_u\alpha_{111}^2, \quad (9.1)$$

where α_a, α_b and α_{111} are direction cosines of the magnetization with respect to the monoclinic a, b and cubic [111] axes (rhombohedral elongation is assumed to be parallel with [111]).

While the planes of rotation of external magnetic field used by Mizoguchi keep high symmetry, the acquired equilibrium direction of magnetization runs on a quite general paths. Therefore, the unit cell loses all operations of symmetry, except for the inversion. In space group Cc, each site splits into two non-equivalent, i.e. there are sixteen tetrahedral sites and thirty-two octahedral sites. In case of P2/c space group, the two A sites split into four magnetically nonequivalent sorts (2:2:2:2), and the six octahedral iron sites (originally 2:2:2:2:4:4) produce ten magnetically nonequivalent sorts (1:1:1:1:2:2:2:2:2:2; two lines did not split any further). For clarity of the plots, the lines are grouped and labelled in a way that corresponds to situation in zero magnetic field. I.e., lines B1–B16 in Cc each denote two of the thirty-two lines, lines B_1–B_6 in P2/c represent ten lines (B_3 and B_4 label only one line each).

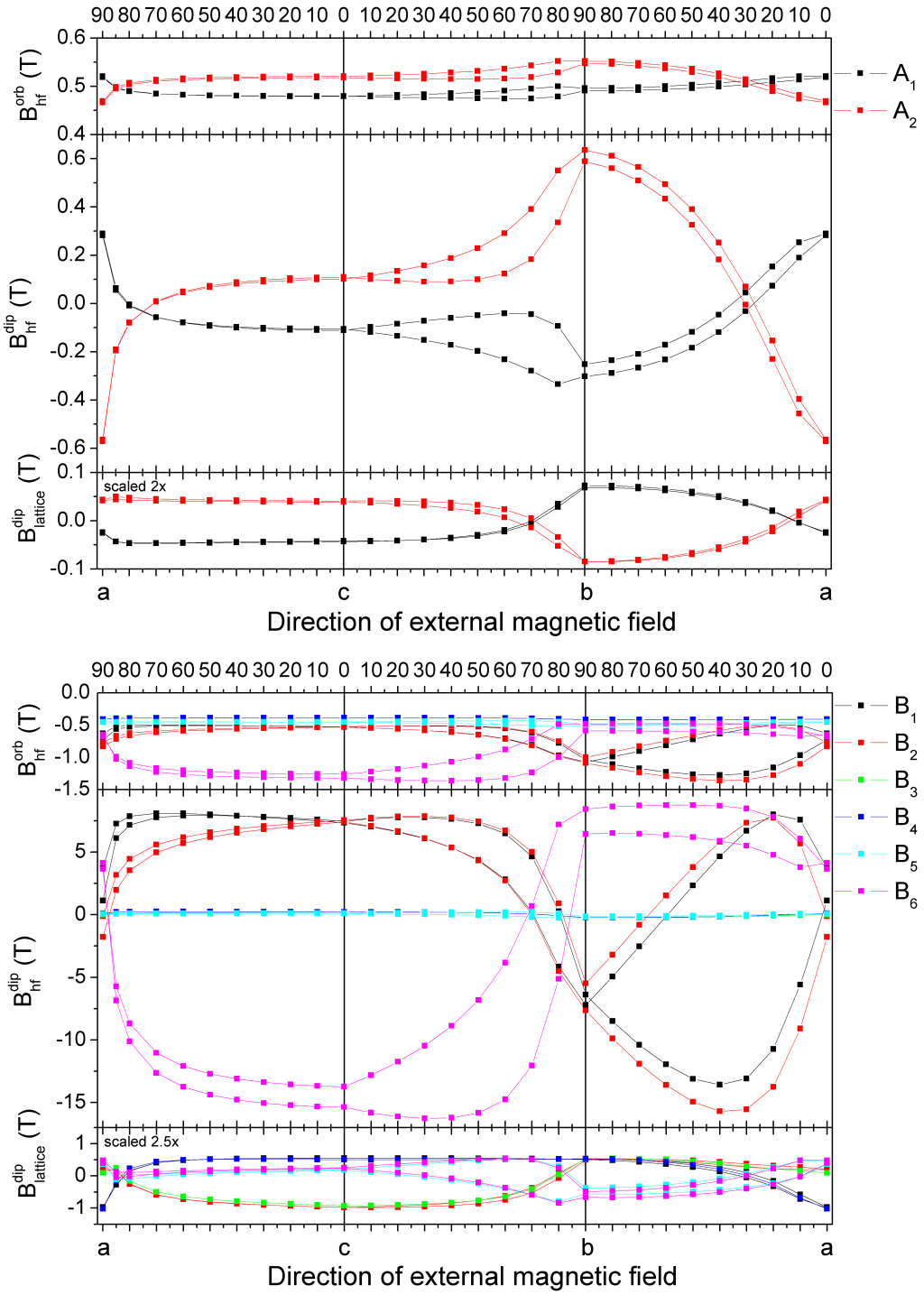

Figure 9.2: Calculated anisotropy of hyperfine field on ^{57}Fe nuclei in tetrahedral (top) and octahedral (bottom) sites of magnetite. Note that the scales of $B_{\mathrm{hf}}^{\mathrm{orb}}$ are different.

The energy window for s-o calculation was increased (from 2.0 Ry to 4.0 Ry) to include additional eigenstates. Anisotropic terms of hyperfine magnetic field, i.e. the dipolar interaction of the nuclear spin with on-site electron spin ($B_{\mathrm{hf}}^{\mathrm{dip}}$) and on-site electron orbital moment ($B_{\mathrm{hf}}^{\mathrm{orb}}$), were acquired from the calculations using the one-step approach as in previous chapters (i.e. running one iteration of s-o SCF after fully converged calculation without s-o). Also the term arising from interaction with magnetic moments of all other ions in the system was calculated ($B_{\mathrm{lattice}}^{\mathrm{dip}}$). These three parts were summed and compared to experimental angular dependences.

Dependence of the individual calculated contributions to the anisotropy, $B_{\mathrm{hf}}^{\mathrm{dip}}$, $B_{\mathrm{hf}}^{\mathrm{orb}}$, and $B_{\mathrm{lattice}}^{\mathrm{dip}}$, is displayed in Fig. 9.2. The planes of rotation imitate those used in experiment with field of 1.3 T: (*ac*), (*ab*), and (*bc*), however, the equilibrium directions were used in the calculations. E.g., the mark 30 degree in (*ac*) plane, which represents direction of magnetic field $\mathbf{B} = (\frac{1}{2}, 0, \frac{\sqrt{3}}{2})$, corresponds to equilibrium direction of magnetization $\mathbf{M} = (0.306, 0.025, 0.952)$. For both types of sites, the dipolar term of the hyperfine field, $B_{\mathrm{hf}}^{\mathrm{dip}}$, is dominant. While the orbital part of the hyperfine field, $B_{\mathrm{hf}}^{\mathrm{orb}}$, has quite significant isotropic part, its contribution to anisotropy is almost negligible. Isotropic part of $B_{\mathrm{hf}}^{\mathrm{dip}}$ is small compared to its anisotropic part, and $B_{\mathrm{lattice}}^{\mathrm{dip}}$ has anisotropic part only.

The dependence of ^{57}Fe NMR spectra on external magnetic field direction was measured at temperature 4.2 K on a sample (12 mm sphere), that was cooled through the Verwey transition under external magnetic field of 1.5 T applied along $[\bar{1}12]$ direction. Such cooling helped to suppress the formation of differently oriented structural domains in the monoclinic phase.

Since the calculated structure (P2/c) differs from the real one (Cc), the number of branches in the angular dependence is lower. Despite it, the calculated and experimental data may be compared, at least qualitatively, as they display some common characteristics. Upon more detailed inspection, we may classify the experimental NMR angular dependences of 32 octahedral B sites (labelled by twos) into three groups with similar behaviour, see Fig. 9.3. First group contains sixteen lines (labelled B1, B2, B3, B4, B6, B8, B9 and B11) that display relatively low anisotropy of hyperfine field, second group consists of ten lines (B5, B7, B10, B12 and B13) that have maximal anisotropy field at *c* axis (i.e. their frequency increases towards the direction of *c* axis), and the splitting in the (*ab*) plane is quite pronounced. Lines of the third group (B14, B15 and B16) have deep minimum at *c* axis, while the dependences are nearly constant in the (*ab*) plane.

However such division is not unique, as some lines mix several features

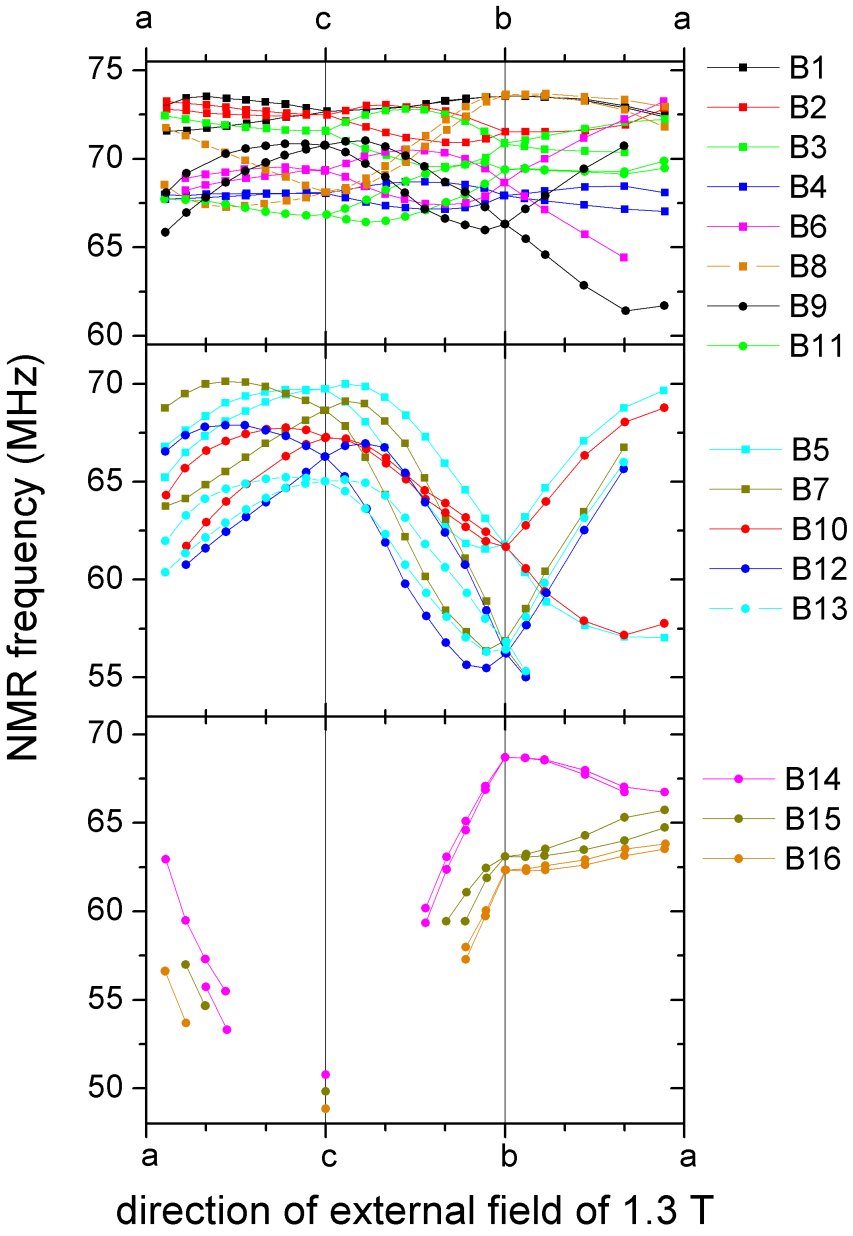

Figure 9.3: Experimental angular dependences of ^{57}Fe NMR spectra were measured at 4.2 K in external magnetic field of 1.3 T by Mizoguchi [33]. Angular dependences of the B lines are classified into three groups. On top are the B lines that exhibit relatively low overall anisotropy, lines that have maximal anisotropy field at c axis and large splitting in (ab) plane are displayed in the middle, and in the bottom are the lines that have deep minimum at c axis, while being nearly constant in (ab).

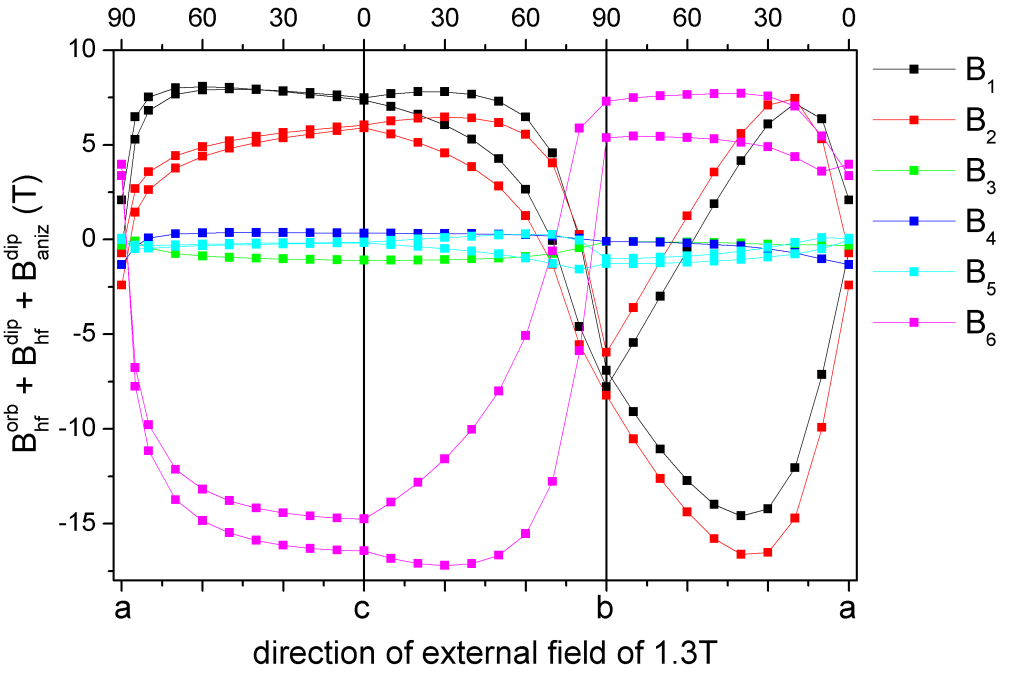

Figure 9.4: Calculated anisotropy of hyperfine field on ^{57}Fe nuclei in octahedral sites of magnetite is shown.

together, and so their assignment to a given group may be disputable, e.g. curve B9 could also belong to the second group. The calculated dependences feature similar characteristics (Fig. 9.4) and may be analogously assigned to these three groups. Anisotropy of calculated dependences B_3, B_4, and B_5 is very low compared to the others, and therefore belong into first group, curves B_1 and B_2 display features that place them in second group (maximum at c, large splitting in (ab) plane), and curve B_6 fits nicely into third group. The dependences B_1–B_6 of the P2/c structure are assigned to their corresponding position in the crystallographic unit cell (see Table 9.3).

By dividing both the calculated anisotropies of hyperfine field and the measured angular dependences into three groups according to their character, it is possible to assign a set of lines in Cc structure to particular lines of P2/c structure (Table 9.4). Such assignment then allows evaluating (at least qualitatively) the relation between P2/c and Cc structures. The strongest and most individual dependence is found in the third group and also in second group, which deserves a bit detailed discussion.

According to calculations (in P2/c), the dominating contribution to the anisotropy is $B_{\mathrm{hf}}^{\mathrm{dip}}$ (Fig. 9.2), which is connected with direction of the on-

angular dependence	coordinates in P2/c		
B_1	0	0	0
	$\frac{1}{2}$	0	0
B_2	0	$\frac{1}{2}$	0
	$\frac{1}{2}$	$\frac{1}{2}$	0
B_3	0.2499	0.0002	0.5067
	0.7501	0.9998	0.4933
B_4	0.7501	0.5002	0.4935
	0.2499	0.4998	0.5065
B_5	0.3790	0.7503	0.7597
	0.6210	0.2497	0.2403
	0.1210	0.2497	0.7602
	0.8790	0.7503	0.2398
B_6	0.3764	0.7503	0.2534
	0.6236	0.2497	0.7466
	0.1238	0.2497	0.2529
	0.8762	0.7503	0.7471

Table 9.3: The individual angular dependences of the B lines are displayed with their relative coordinates in the crystal structure with P2/c unit cell parameters: $a = 1.677515$ nm, $b = 0.5944407$ nm, and $c = 0.5924701$ nm, and $\gamma = 90.2363°$.

P2/c		Cc		common features
lines	number of sites	lines	number of sites	
B_3, B_4, B_5	8 (2:2:4)	B1, B2, B3, B4, B6, B8, B9, B11	32	relatively low overall anisotropy
B_1, B_2	4 (2:2)	B5, B7, B10, B12, B13	20	maximal anisotropy at c axis, large splitting in (ab) plane
B_6	4	B14, B15, B16	12	deep minimum at c axis, nearly constant in (ab) plane

Table 9.4: Experimental dependences in Cc structure are assigned to calculated ones in P2/c structure. The assignment is based on common features that the dependences display in planes of rotation (ac), (bc), (ab).

site	μ (μ_B)	μ_{orb} (μ_B)	valence (from μ)	charge difference Fe(B)$^{2.5-q}$		
				calculated	Wright	Nazarenko
A_1	4.093	0.014	3.004			
A_2	4.086	0.015	2.996			
B_1	−3.577	−0.059	2.205	−0.30	−0.12	−0.12
B_2	−3.576	−0.062	2.204	−0.30	−0.11	−0.12
B_3	−4.194	−0.011	2.822	0.32	0.11	0.12
B_4	−4.193	−0.011	2.821	0.32	0.11	0.12
B_5	−4.156	−0.012	2.785	0.29	0.09	0.10
B_6	−3.560	−0.070	2.189	−0.31	−0.09	−0.10

Table 9.5: Calculated magnetic and orbital moments (μ, μ_{orb}) for sites in P2/c. Charge differences q in octahedral sites were derived from the calculated moments and compared with experimental data of Wright *et al.* [34] and Nazarenko *et al.* [76].

site spin. Therefore, huge difference between the dependences of the three groups suggests that the corresponding octahedral iron atoms have different magnetic moments. Analogous behaviour may be observed for B_{hf}^{orb}, which is smaller in magnitude, but also supports this differentiation. B_{hf}^{orb} is proportional to projection of orbital momentum onto direction of magnetization, and thus its pronounced changes indicate non-zero value of orbital momentum of the octahedral iron atom. Consequently, P2/c sites corresponding to lines B_1, B_2, and B_6 have presumably significant orbital momentum, which means that their valence states are closer to Fe^{2+} (i.e. charge lower than 2.5). The remaining octahedral iron atoms (corresponding to lines B_3, B_4, and B_5) then have valency higher than $Fe^{+2.5}$, which results in lower orbital momentum and therefore less varying dependence of B_{hf}^{orb}. These arguments are supported by calculated values of spin magnetic moments and orbital moments, and are also in agreement with charge disproportion observed by Wright *et al.* ([34], valences determined from Bond valence sums) and Nazarenko *et al.* ([76], resonant x-ray diffraction), see Table 9.5.

The above stated considerations and findings for P2/c now can be applied to Cc. The diffraction methods (e.g. neutron and synchrotron x-ray diffraction by Wright *et al.* or resonant x-ray scattering experiments by Nazarenko *et al.*) consider the transfer from P2/c (usually constrained by Pmca pseudosymmetry) to Cc symmetry as a small correction; the Cc reflections are weak and their refinement is troublesome. However, comparison of hyperfine field anisotropy for P2/c and Cc shows remarkable differences

	c (easy)	b (intermediate)	a (hard)
δ_{orb}	0	1.173	2.603
δ_{dip}	0	0.05	−0.04
δ_{exp}	0	0.54	2.66

Table 9.6: Magnetocrystalline anisotropy energy for easy, intermediate and hard axes per volume of the unit cell are given in 10^6 J/m^3 with respect to the value for easy axis.

(Table 9.4), when the numbers of lines in particular groups are considered. The most striking difference can be found in third group, where the line B_6 comprise of four positions in P2/c (i.e. B_6 has relative intensity 4/16), whereas there are only three lines of the Cc structure (B14, B15, B16) with total intensity 12/64 (i.e. 3/16). This means that NMR, namely the anisotropy of hyperfine interaction, is also an effective instrument to study the charge disproportion in Cc magnetite. In the future, by analogous calculations in Cc space group, the approach based on matching the curves of hyperfine field anisotropy could accomplish the complete interpretation of NMR spectrum below T_{V}.

In addition to hyperfine field anisotropy calculations, also the magnetocrystalline anisotropy was evaluated as the difference in energy (with respect to easy axis) per volume of the unit cell, $\delta_{\mathrm{orb}} = \Delta E^{\mathrm{an}}_{\mathrm{orb}}/V$. The calculated anisotropy corresponding to the on-site orbital momentum, δ_{orb} reproduced the magnetic axes: easy (c), intermediate (b) and hard (a), see Table 9.6. The anisotropy is presented with respect to value for the easy axis c. Also the dipolar anisotropy δ_{dip} was calculated by summing only the spin parts of magnetic moments in a sphere with radius 128 a.u. (~ 6.8 nm). The neglection of the orbital momentum part of magnetic moment is justified, as apparently, δ_{dip} is by more than order of magnitude smaller than the single ion anisotropy δ_{orb}. Experimental values δ_{exp} were taken from Abe *et al.* [75].

9.2 Axis Switching in Magnetite

NMR spectroscopy can be used for local observation of dynamics and accompanying structural changes in low temperature phase of magnetite in order to study the phenomenon of axis switching (AS). In this chapter results of NMR studies of axis switching are presented, preceded by careful characterization by magnetic measurements and preparatory NMR experiments.

Changes in the ^{57}Fe NMR spectra evidence that a structural transition, interrelated with the axis switching, is reached in the material. The switching process is observed in the finite time. The dynamics of the observed process is analyzed using the Singular Value Decomposition and employing the theory of Kolmogorov-Johnson-Mehl-Avrami for description of the experimental data, both from magnetization measurements and NMR.

9.2.1 Magnetization Experiments

The sample was a single crystal of magnetite (sample 00S, see Table 9.1) annealed in CO/CO_2 gas mixture for desired stoichiometry, and ground to the spherical shape (3 mm in diameter). Sample quality was checked prior and after grounding by AC magnetic susceptibility. Magnetization experiment was aimed to roughly check switching field vs. temperature for this particular sample. The measurements were performed at magnetic field up to 1.2 T in the temperature range from 4.2 K up to T_V. The sample was oriented with one $\langle 100 \rangle$ axis parallel to measurement rod of the magnetometer; two other directions of $\langle 100 \rangle$ type could be aligned along external magnetic field provided by rotatable head. All magnetization measurements were performed by group of Prof. Kozłowski of AGH University in Kraków. Analysis of these measurements is within the frame of this work.

For each experiment, the sample was first cooled from 150 K to specified temperature (see Fig. 9.5) in magnetic field $B = 0.8$ T directed along one of the cubic axes, [100], establishing both crystallographic axis c as well as easy magnetic axis. Field dependence of magnetic moment, $M(B)$, was then measured up to $B = 1.2$ T (and down to 0 T); direction of the field remained the same (i.e. along magnetic easy axis). The sample was then rotated by 90° and $M(B)$ was measured again, this time with field pointing along [010], magnetically unspecified direction. With this last experiment, $M(B)$ was initially completely different than it was for field in magnetic easy direction until the axis switching occurred, which was signaled by a rapid magnetic moment growth (see Fig. 9.5). The switching fields, B_{sw}, found by this method are shown in the inset of Fig. 9.5.

Since the axis switching has a relaxation character, the process is time dependent. This time dependence (in the form of $M(t)$ once the field of 0.8 T was set within 10 s) is presented in Fig. 9.6 for several temperatures where the process could be observed by used setup. It should first be noted that although at $T = 50$ K the magnetic field $B = 0.8$ T cannot switch the axis even after 1.5 h waiting, the process is very fast (~ 10 s) at 65 K. This

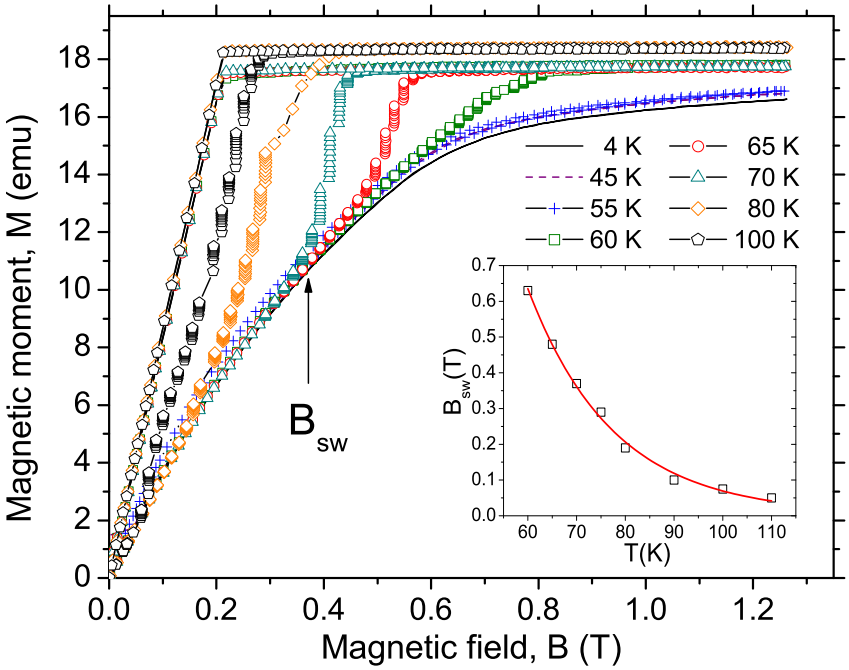

Figure 9.5: $M(B)$ along [010], initially unspecific magnetic direction, after magnetic easy axis [100] was established by the field (0.8 T) cooling. The arrow shows the external magnetic field, B_{sw}, triggering the change of magnetic easy axis at 70 K. In the inset, the approximate temperature dependence of B_{sw} is shown. (The field sweep rate was 0.4–0.5 T/min.)

fast response, also supposedly magnetic-field dependent, certainly affects the $M(B)$ results shown above and more careful analysis is desirable.

To analyze the time dependence of magnetic measurements one can investigate how the volume of the sample transforms from initial, unswitched phase towards final, switched phase. The value of measured magnetization at time $t = 0$ s marks the beginning of the process, while for $t \to \infty$ saturated value of magnetization is reached, corresponding to the state when the whole volume of the sample is transformed. Let V denote the volume of the sample that has already transformed and V_0 the total volume of the sample. Then the fraction transformed, $f = \frac{V}{V_0}$, is a function that describes the transformation process in time. It can be assigned to an observable quantity, e.g. for magnetization measurements (Fig. 9.6) we can define $f = \frac{M - M_0}{M_\infty - M_0}$,

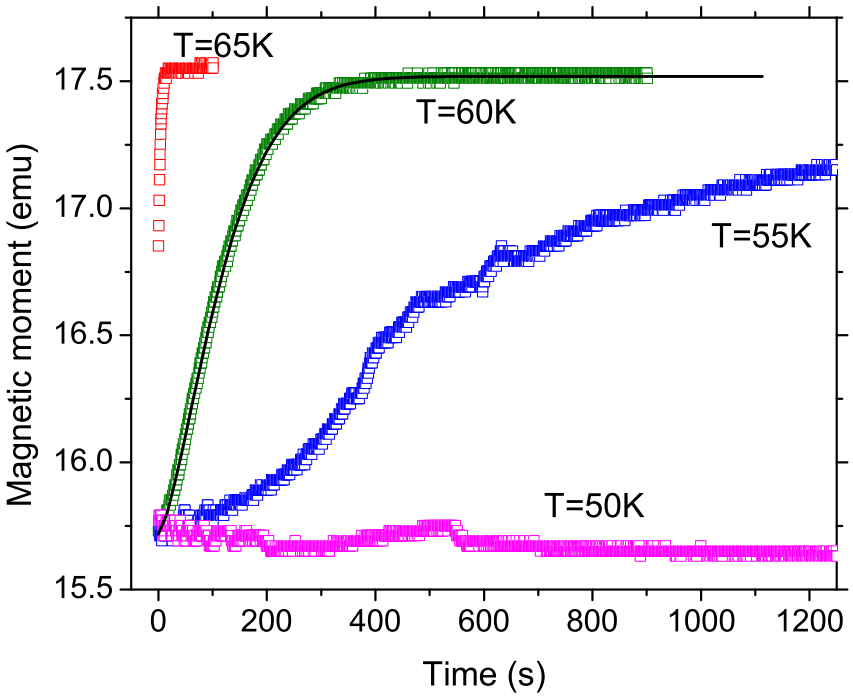

Figure 9.6: Time dependence of magnetic moment once the field of 0.8 T was suddenly (within 10 s) applied along [010] direction commencing (or not, as at 50 K) axis switching process. The fit (line) to the model (see Eq. 9.4) is also shown for $T = 60$ K. For 65 K, we have estimated that the process had started ca. 9 s before the first experimental point was captured.

where M_0 is the magnetization at the beginning of the switching process and M_∞ stands for the magnetization of fully transformed sample. The function $f(t)$ depends on sample history and is supposedly very complicated. In general, it is a functional of temperature and external magnetic field in the whole course of the process up to time t. Apparently, its rate of change, $\mathrm{d}f/\mathrm{d}t$ is highly sensitive to change of temperature or applied magnetic field.

Switching of magnetic easy axis in magnetite and induced structural change is a type of isothermal transformation, for which the concept of phase transformation kinetics, as defined by the Kolmogorov-Johnson-Mehl-Avrami (KJMA) [77, 78, 79, 80, 81] theory can be adopted. KJMA theory describes the kinetics of transformation process by statistical considerations

of nucleation and growth. Although the original Avrami model was developed for crystal growth, it has also been widely used to characterize various transformations in solids, including domain switching in ferromagnetics and ferroelectrics [82, 83, 84, 85]. Usually, the equation that describes the time dependence of a fraction transformed, f, reads

$$f = 1 - e^{-kt^n}, \tag{9.2}$$

where parameter k is Avrami coefficient, which is related to the rate of nucleation and growth and is therefore sensitive to temperature and magnetic field. Parameter n stands for Avrami exponent that rules the mechanism of the transformation, among other characteristics also the effective dimensionality of the transition. Equation (9.2) can be rewritten introducing a characteristic time τ:

$$f = 1 - e^{-(\frac{t}{\tau})^n}, \tag{9.3}$$

and expressed in terms of magnetization:

$$M = M_\infty - (M_\infty - M_0)e^{-(\frac{t}{\tau})^n}. \tag{9.4}$$

Using the equation 9.4, the fitting procedure for $T = 60$ K and $B = 0.8$ T matched the experimental data very well and yielded $n = 1.451 \pm 0.004$ and $\tau = 133 \pm 3$ s. Magnetization measurements for other temperatures ($T = 65$ K and 55 K) are burdened with quite a considerable error. For $T = 65$ K the transformation proceeded too fast to allow observation of the initiation of the switching while, on the contrary, at temperature $T = 55$ K the process developed rather slowly, which made the experiment vulnerable to temperature fluctuations and instabilities. Time derivative of f has the form $\frac{\mathrm{d}f}{\mathrm{d}t} = \frac{nt^{n-1}}{\tau^n}\exp(-\frac{t}{\tau}^n)$, which for $n \sim 1.45$ yields relation $\mathrm{d}f = t^{0.45}(1-f)\mathrm{d}t$. This simply means that increment of fraction transformed is proportional to untransformed fraction and depends also approximately on square root of time. Since no simple physical picture stands after such time dependence, this was not further elaborated on. Time dependences for other temperatures were not analyzed, however, all magnetization measurements helped to design the NMR experiments.

9.2.2 NMR Experiment

External static magnetic field was supplied by superconducting magnet-cryostat system Janis with a split solenoid. The temperature variation was performed in a built-in anti-cryostat (Variable Temperature Insert VTI Janis enabling the continuous helium flow) with Lakeshore 332S controller.

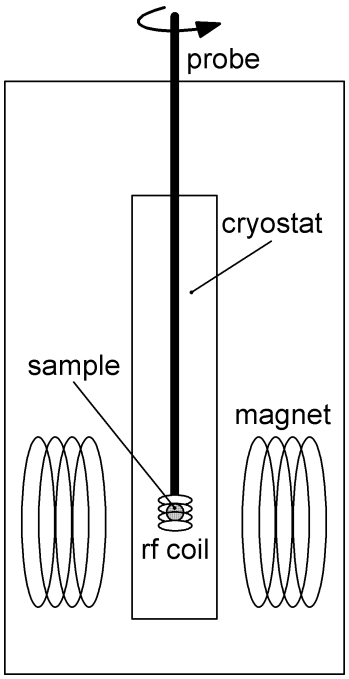

Figure 9.7: Cubic [001] axis of the sample, vertical, is parallel to the rf coil axis. By rotating the probe, the direction of external magnetic field can be adjusted along any chosen direction within the (001) plane.

Temperature was measured by Cernox sensor placed close to the sample. The axis of superconducting solenoid was perpendicular to the axis of radiofrequency (rf) coil in the NMR probe, allowing to change the magnetic field direction on the sample simply by rotating the probe around its vertical axis (see scheme in Fig. 9.7). The sample position was fixed in the rf coil so that [001] cubic axis was parallel to the rf coil axis. We estimate the precision of specified crystallographic direction alignment for ca. 4° (taking into account accuracy of Laue crystal orientation and sample transfer to the probe).

The axis switching phenomenon and following structural transformation was studied by NMR experiment in several consecutive steps. At first, we checked for several possible factors that could influence the experimental results, i.e. spin-lattice and spin-spin relaxation, excitation conditions

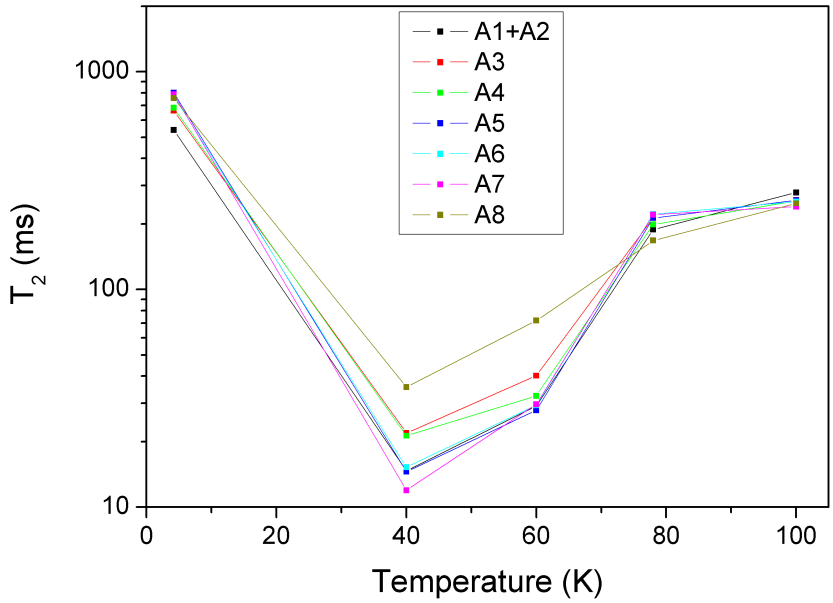

Figure 9.8: T_2 relaxation time of A lines in magnetite at five different temperatures.

and also how cooling of the sample in magnetic field suppresses formation of structural domains in the monoclinic phase. Furthermore, the effect of gradual change of external field direction (in respect to field-cooling direction) on the NMR spectra was considered. After these preparative steps we proceeded to experiments that detected the axis switching by NMR spectroscopy. Finally, also the dynamics of the switching process was observed by NMR and analyzed. All these steps are described in the following paragraphs in more detail. Although all spectral lines, A and B, were measured, only A lines are analyzed here: they are of higher amplitude, and so more subtle details could be inferred.

9.2.3 NMR: Effects of Relaxation, Excitation Conditions and Field Cooling

NMR Relaxation

When concerned with time-dependent phenomena such as axis switching, the NMR relaxations become crucial parameters to project the NMR ex-

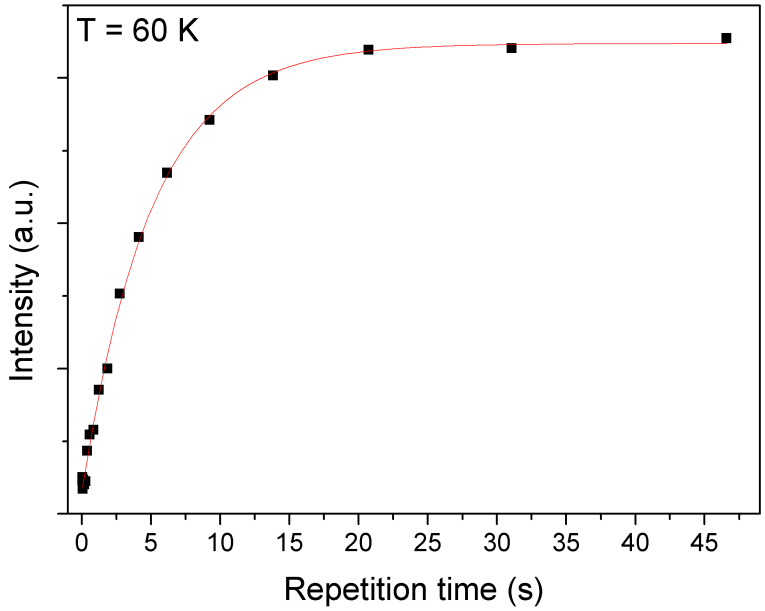

Figure 9.9: Dependence of A3 line intensity on repetition time between two scans. Each data point was obtained as a sum of 16 scans. Within the short repetition times the system cannot reach the equilibrium, which significantly lowers the intensity during the next scan. Red curve is the fit of the dependence of intensity $I = I_0(1-\mathrm{e}^{-t/T_1})$ to experimental data points yielding $T_1 = 5.05$ s.

periment. In this context, the spin-spin relaxation (characterized by a time T_2) limits the length of used pulse series, whereas the spin-lattice relaxation (time T_1) essentially determines the overall length of NMR measurement. E.g., when comparing intensities of NMR lines with very short T_2 times, the applied pulse sequences should be short enough, so that the decay of echo intensity with time may be neglected. For this purpose a rough temperature dependence of T_2 time was obtained on studied sample; T_2 dependences for A lines are given in Fig. 9.8. All used pulse series were designed with respect to T_2 at given temperature, so that the effect of T_2 relaxation on measured data may be neglected. The spin-spin relaxation was slow enough in order to allow summation of 50 spin echoes within the Carr-Purcell pulse sequence.

The effect of spin-lattice relaxation on length of measurement is more problematic issue and cannot be simply resolved. Usually some reasonable

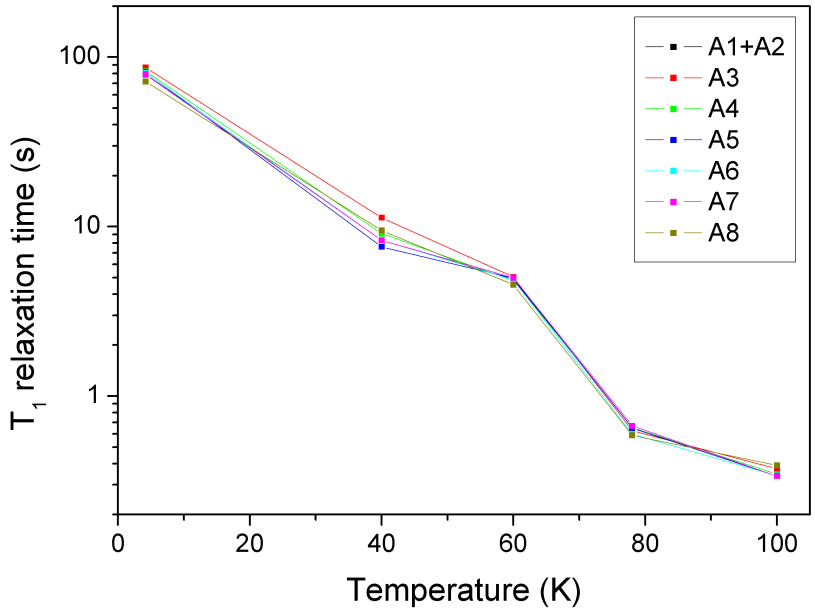

Figure 9.10: T_1 relaxation time of A lines in magnetite at five different temperatures.

number of scans has to be acquired in the NMR measurement, in order to gain sufficient signal-to-noise ratio. However, the time space between two consecutive scans (i.e. "repetition time") must be long with respect to T_1 in order to allow the system to return to equilibrium. An example of such behaviour is displayed in Fig. 9.9. Consequently, in case of very long T_1 times there is a danger that the measurement is too slow to observe any dynamics of the monitored system. In order to help finding suitable temperature range, temperature dependences of relaxation T_1 was roughly scanned below the Verwey transition (Fig. 9.10).

Temperature dependences of relaxation times T_1 and T_2 display similar characteristics as observed by Novák *et al.* [39], i.e. a shallow plateau for T_1 dependence and a deep minimum in T_2 dependence between 40 and 60 K.

NMR Excitation

Magnetization in a magnetite sample, which has not been treated by any field cooling process and therefore consists of various magnetic domains, may dwell with the same probability in any direction formed from cubic

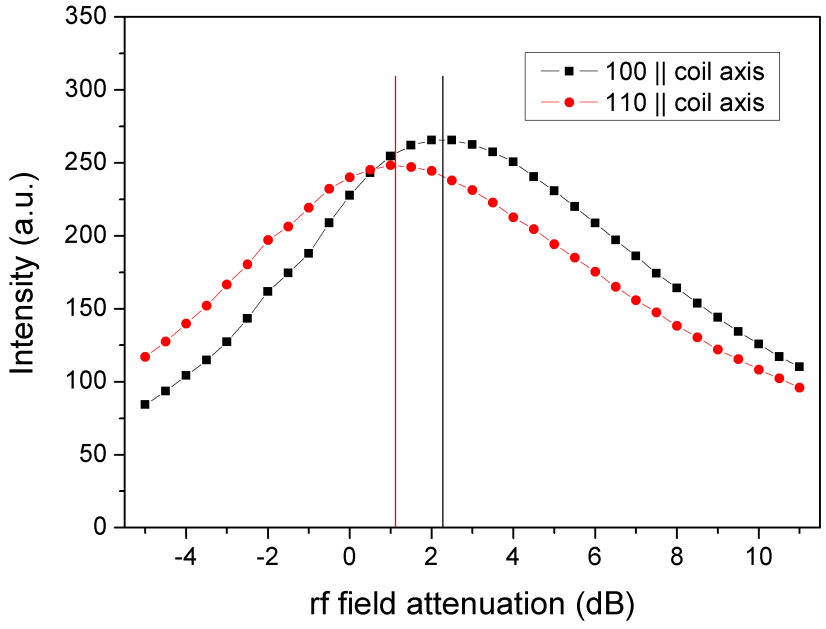

Figure 9.11: Dependence of NMR signal intensity on rf field is compared for two orientations of the sample in the coil. The dependences were measured at 69.607 MHz at 4.2 K (A1+A2 doublet).

⟨100⟩ easy axes during the Verwey transition. However, for a particular positioning of the sample in rf coil, the coil can only excite and detect nuclei in such magnetic domains that have non-zero projection of magnetization onto the plane perpendicular to rf coil axis [49]. It is possible to observe measurable changes in excitation of NMR signal for different directions of rf coil axis with respect to crystallographic system of the sample. Comparison of NMR signal intensity dependence on rf field attenuation for two distinct orientations of the sample in the coil are displayed in Fig. 9.11. In the first case one of the crystallographic ⟨100⟩ axes (e.g. [100]) coincides with rf coil axis and nuclei in such domain type cannot be excited and detected, whereas nuclei in domains with magnetization lying in (100) plane are well excited. In latter case the sample was oriented so that axis of the coil lied in [110] direction, therefore nuclei in domains of [001] type contributed fully, and the types [100] and [010] only partially. Special attention was thus paid to a careful positioning of the sample in the rf coil, in order to avoid any undesirable effects connected with excitation.

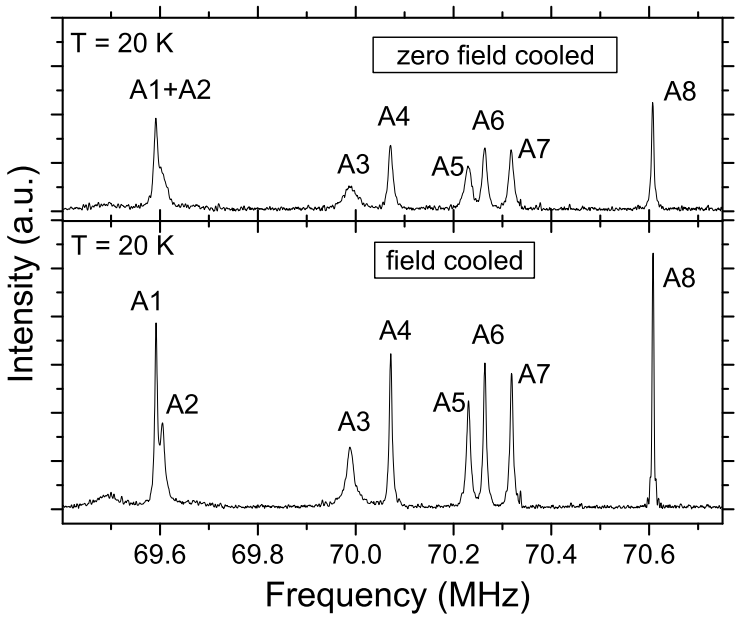

Figure 9.12: ^{57}Fe NMR spectra of zero field cooled and field cooled sample measured in zero external magnetic field at 20 K. Spectral range of A lines is plotted, only A lines are denoted.

Field Cooling

Another important factor is the formation of domains during cooling through the Verwey transition. Figure 9.12 shows NMR spectra in the frequency range of A lines (69.4–70.8 MHz) obtained at 20 K in zero magnetic field after the sample was cooled through Verwey transition either in zero magnetic field (ZFC) or in magnetic field of 1.3 T (FC)

In ZFC case the sample is supposed to consist of structural domains with different orientations of their monoclinic crystallographic axes a, b and c, and thus monoclinic c axes are randomly distributed among former $\langle 100 \rangle$ axes of the cubic structure. As the sample was oriented with its [001] cubic axis parallel to the rf field, one third of the structural domains in the monoclinic phase had the rf field parallel to the hyperfine field. Nuclei in such structural domains cannot contribute to NMR signal [49]. Additionally, formation of structural domains with monoclinic c axes distributed in all $\langle 100 \rangle$ cubic directions broadened the NMR lines, supposedly due to internal strains.

In FC measurement the sample was cooled through the Verwey tran-

spectral line	intensity (a.u.)		FC:ZFC ratio	deviation from 3:2 (%)
	FC	ZFC		
A1+A2	240	161	1.49	−1
A3	139	92	1.51	1
A4	136	89	1.53	2
A5	114	76	1.50	0
A6	122	80	1.53	2
A7	122	79	1.54	3
A8	127	83	1.54	3

Table 9.7: Comparison of integral intensities of spectral lines for FC and ZFC. Spectra were recorded at 20 K in zero magnetic field.

sition under magnetic field of 1.3 T perpendicular to the rf coil axis (e.g. [010] axis) and strong enough to suppress the formation of structural domains, i.e. all monoclinic c axes were created from the [010] cubic axis. The spectral lines were significantly narrowed compared to ZFC spectrum as the structural disorder due to presence of several domains was reduced. Due to spectral line narrowing, A1 and A2 were particularly resolved. This way, after field cooling, the monoclinic c axes of the structure were perpendicular to the rf coil axis (lying in former cubic [001]), and therefore, nuclei in the whole sample contributed to the NMR signal, which is evidenced in the spectrum.

The measured FC and ZFC spectra allowed comparing the integral intensities even quantitatively. The integral intensity of FC spectrum was 1.5 times higher than the ZFC spectrum intensity (see Table 9.7), which reflects the fact that all nuclei in FC case add to the NMR signal while only two thirds of the nuclei do contribute in ZFC case. This analysis confirmed that cooling through the Verwey transition in external magnetic field 1.3 T suppressed the structural disorder with respect to c axis orientation. (However, partial disorder persisted, caused by ambiguity of a and b axes, or by the c axis twinning.)

9.2.4 Angular Dependence of NMR Spectra

In the next step NMR spectra were measured in dependence on the direction of external magnetic field with respect to the crystallographic axes of the sample. Spectra measured in external magnetic field display frequency shifts and line splitting as an effect of magnetic non-equivalency of iron sites and anisotropy of hyperfine interaction. (For a general direction of magne-

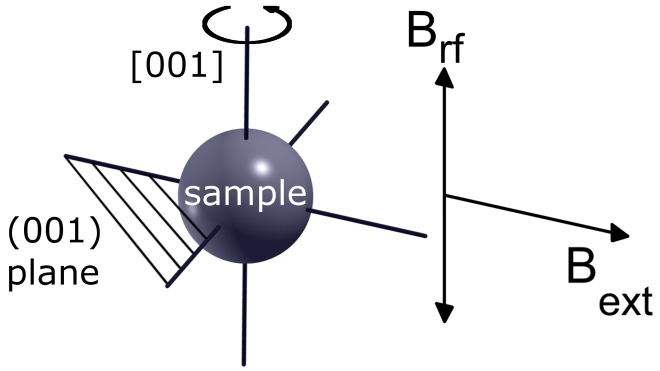

Figure 9.13: Experimental arrangement: rotational axis [001], directions of external magnetic field and radiofrequency field are designated.

tization in uniformly magnetized single crystal each line can split into two lines. In our case, additional splitting can occur due to the presence of *a*-*b* and *c*-*c* twins.)

The field-cooling procedure as before (i.e. 1.3 T set along [010] direction) was applied again, cooling down to 20 K. Then the magnetic field was set to 0.3 T for the following measurements. The chosen temperature and magnetic field were sufficiently low in order not to allow the axis switching during this experiment. Also the temperature was suitable compromise between the increase of nuclear spin-lattice relaxation rate and signal decrease with increasing temperature. One should note, however, that the field of 0.3 T does not ensure the magnetization to be parallel to the field, especially for high angles between the magnetic field and easy axis direction. The probe was rotated around its axis in steps of 5–10 degree (sample rotation around [001], see Fig. 9.13). NMR spectra obtained for different angles in (001) plane are displayed in Fig. 9.14.

External field, stronger than the demagnetization field and applied in the easy direction of magnetization, induces frequency shift of the spectral lines that corresponds to ^{57}Fe gyromagnetic factor (1.378 MHz/T). The absolute value of the shift is identical for all spectral lines; it is positive for A lines and negative for B lines. In magnetic field 0.3 T the observed frequency shift was

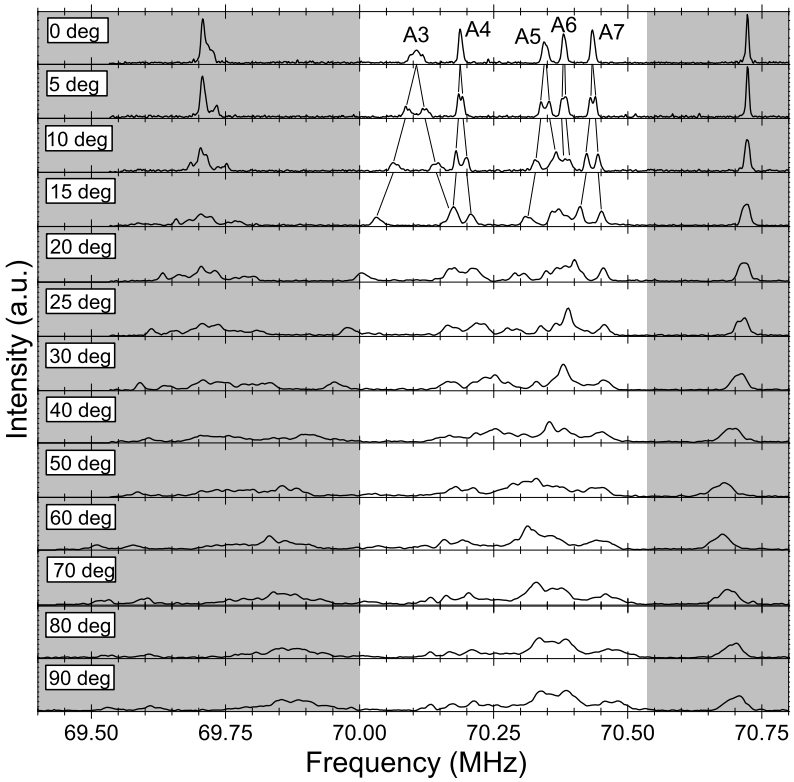

Figure 9.14: Angular dependence of NMR spectra in 0.3 T external magnetic field at $T = 20$ K. Spectral range of A lines is plotted only. Lines A3–A7 in the highlighted area were measured in the subsequent experiment (axis switching dynamics).

0.114 MHz,* yielding the demagnetization field of 0.215 T. This value agrees with magnetization 0.615 T obtained from magnetization data in [44] using demagnetization factor $D = 1/3$ as for sphere. External magnetic field, applied in a non-collinear way with respect to the easy axis, changes the direction of magnetization, which is observable in the NMR spectra due to anisotropy of hyperfine interaction [33, 64]. For the [010] (the direction of magnetic field during cooling, i.e. the easy axis), the spectral lines are narrow, and as the magnetization moves from this direction, the lines shift, split, and broaden. Though magnetic field of 0.3 T is not strong enough to align the magnetization precisely into its direction, it is sufficient to provide reasonable notion of spectra dependence on magnetization direction. Such

*Which means that the change of magnetic field on nucleus was 0.085 T.

information was needed to understand the NMR spectra obtained during the axis switching procedure.

9.2.5 Axis Switching Detection by NMR

The experiment was arranged in a similar way as for angular dependence measurements, i.e. cubic [001] axis parallel with rf coil axis and [010] axis parallel with the external magnetic field (Fig. 9.13), and the sample was cooled in magnetic field 1.3 T through the Verwey transition to 20 K. Then the magnetic field was reduced to 0.3 T and NMR spectrum was recorded (see Fig. 9.15a), naturally, agreeing precisely with 0 degree spectrum in the angular dependence. Now the probe was rotated 90 degree clockwise (CW) so that [010] direction became perpendicular and [100] parallel to the external magnetic field (see Fig. 9.15b); as expected, the spectrum agreed with 90° spectrum in the angular dependence. At this point the easy axis (c axis) remained in direction not favorable with the new direction of magnetization forced by the external magnetic field. However, at given conditions (temperature 20 K and magnetic field of 0.3 T) axis switching could not occur yet.

To enable the structural changes, temperature was raised to 80 K and the field was increased to 1.3 T for more than 5 minutes, which is long enough for switching to occur (according to Fig. 9.6). Then the temperature was lowered back to 20 K, likewise the field was reduced to 0.3 T once again. Subsequently measured NMR spectrum (Fig. 9.15c) had the same character as Fig. 9.15a spectrum, which revealed that the crystal structure underwent a change to comply with the new direction of easy axis. The c axis had a new direction, perpendicular to that of in Fig. 9.15a-b.

Then the probe was turned 90° CCW, back into the original position and the spectrum (Fig. 9.15d) showed similar features as in Fig. 9.15b. Now the conditions enabling the axis switching were set again (temperature 80 K and magnetic field of 1.3 T for more than 5 minutes), and the spectrum recorded at 20 K in 0.3 T field (Fig. 9.15e) verifies that the easy axis switched back into the field direction. Fig. 9.15f displays spectrum after the probe was rotated once again by 90° CW (configuration is the same as in Fig. 9.15b). Also the spectra 9.15b, 9.15d and 9.15f displayed more similar features. These results confirmed that the phenomenon of magnetic easy axis switching coupled with structural transformation is well reproducible.

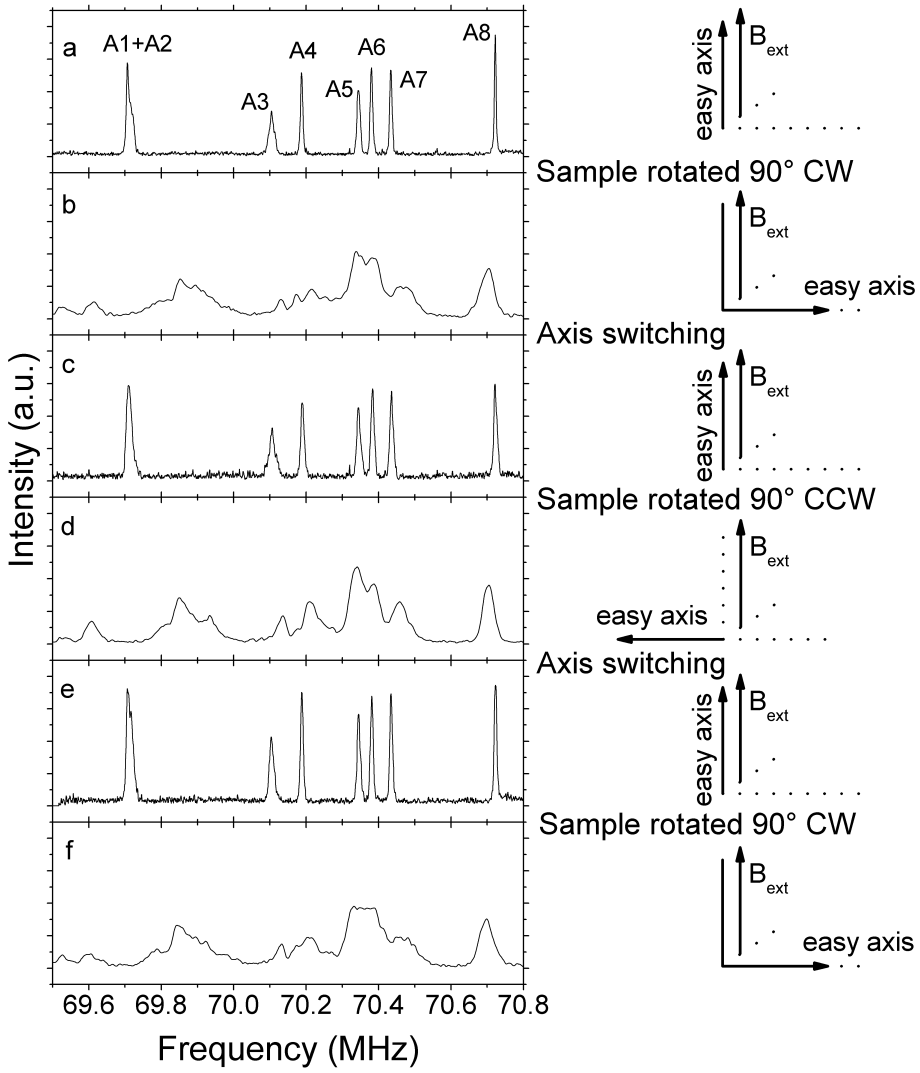

Figure 9.15: Axis switching detection by NMR. Figures 9.15a, 9.15c and 9.15e correspond to external magnetic field set along the easy axis, while in 9.15b, 9.15d and 9.15f the external field is perpendicular to the easy axis (field $B = 0.3$ T, temperature $T = 20$ K). Between the measurements b and c (and also between d and e), the sample was heated up to 80 K, and the field of 1.3 T was applied to switch the easy axis. Scheme on right side describes the steps of the experiment; see details in text.

9.2.6 Axis Switching Dynamics

In the previous step, the axis switching was detected by NMR by comparing spectra of the sample before and after the changes induced by external magnetic field. It was thus natural to use the NMR method to study the dynamics of this process. In order to do so, the timescale of the switching had to be stretched from minutes to hours or tens of hours by adjusting carefully the experimental conditions (temperature and magnetic field). We tried to remain in temperature range close to 60 K where the magnetization measurements were analyzed in detail, while also the T_1 relaxation times were reasonably short at these temperatures. Lower temperature would seemingly extend the course of switching process, and therefore allow more averaging. However, with lowering the temperature the undesired effects of temperature fluctuations or instabilities would inevitably increase.

Finally, considering the magnetic measurements (Fig. 9.5 and 9.6) and measurements of T_1 relaxation times (Fig. 9.10), the temperature 57 K and external magnetic field of 0.5 T were chosen as suitable conditions to induce the development of the axis switching within approximately 20 hours, which was long enough for NMR to capture the dynamics of the process. Only lines A3–A7 were measured in order to obtain sufficient number of NMR spectra with reasonable signal/noise ratio in the course of the AS process.

The experiment was arranged in a similar way as before — the sample was cooled in field of 1.3 T through the Verwey transition to 57 K. After the field was reduced to 0.5 T, the probe was rotated 90 degrees in order to start the switching. In the following time, NMR spectra were recorded one after another, each spectrum taking approximately 106 minutes. The resulting NMR spectra are displayed in Fig. 9.16. From the comparison with spectra in Fig. 9.14, it follows that the first measured spectrum (in front of Fig. 9.16) displays the state at the very beginning of the switching process while the last measured spectrum (in the rear of Fig. 9.16) indicates that the switching already occurred. When comparing spectra in Fig. 9.16 with those in Fig. 9.15, the frequency shift of about 0.2 MHz due to higher temperature (57 K compared to 20 K) and magnetic field (0.5 T vs. 0.3 T) must be taken in account.

9.2.7 Analysis of NMR Results on Switching Dynamics

In order to obtain more information, the NMR results were further treated. The set of time evolved NMR spectra (Fig. 9.16) was first corrected for

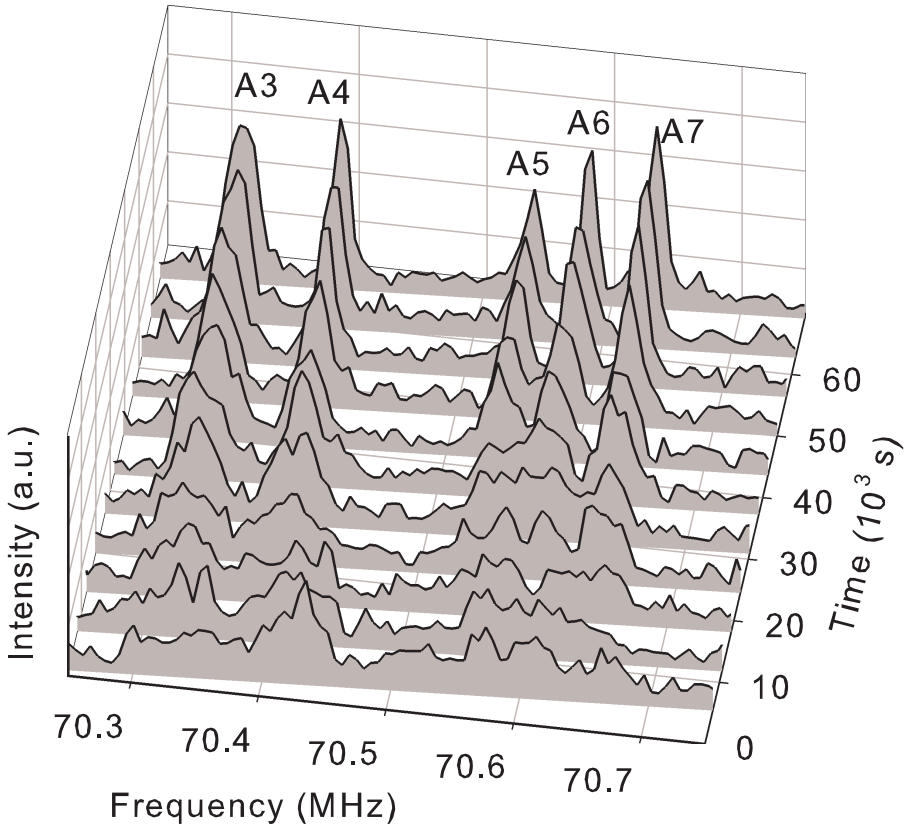

Figure 9.16: Axis switching dynamics observed by NMR ($T = 57$ K, $B = 0.5$ T). See text for details.

a finite time needed for the spectrum measurement, causing that various regions of each (frequency swept) spectrum were not obtained at the same instant. By using a linear interpolation (and extrapolation for the right half of the first spectrum and the left half of the last one), the shapes of individual spectra were adjusted so that each spectrum $Y_i(\nu)$ was related to a time point in which the central region of the spectrum was measured.

Further analysis was performed by using a Singular Value Decomposition (SVD) [86]. This procedure helps to comprehend series of $Y_i(\nu)$, $i = 1, 2, \ldots, N$ spectra (in our case $N = 11$) via their conversion into linear combinations of a set of new spectral components $U_j(\nu)$, $j = 1, 2, \ldots, 11$ that are mutually orthogonal, i.e. $\int U_j(\nu)U_k(\nu)\,d\nu = \delta_{jk}$. Coefficients of linear combinations are expressed by elements of a real unitary matrix V_{ij}

and positive singular numbers W_j:

$$Y_i(\nu) = \sum_{j=1}^{N} V_{ij} W_j U_j(\nu). \tag{9.5}$$

The singular number W_j stands for the statistical weight of the j-th orthogonal spectral component $U_j(\nu)$ and the matrix element V_{ij} quotes relative portion of the j-th component $U_j(\nu)$ in the i-th analyzed spectrum $Y_i(\nu)$. The orthogonal components $U_j(\nu)$ are ordered, so that the corresponding singular numbers W_j form a descending succession. Usually, not all N orthogonal components $U_j(\nu)$ but only the first few (D) of them are significant to approximate the set of input spectra within an experimental error (incurred by noise in NMR spectra):

$$Y_i(\nu) \simeq \sum_{j=1}^{D} V_{ij} W_j U_j(\nu). \tag{9.6}$$

D is referred to as factor dimension and characterizes complexity of the information contained in the analyzed series of spectra. For instance, if the switching process represented just a simple jump from the original conditions to the final state without any additional process or intermediate state, the factor dimension should be two.

The SVD results are shown in Fig. 9.17. The dependence of the singular numbers W_j on the number j of orthogonal component $U_j(\nu)$ (upper left graph) displays clearly that only three singular numbers lie above the line corresponding to the noise contributions. This indicates that factor dimension is three. Another way to determine the factor dimension is to consider D in equation 9.6 as a gradually increasing independent integer variable, and to plot values of the residual error, i.e. the difference between the left and right site in equation 9.6 expressed as a standard deviation (upper right graph in Fig. 9.17). Also this criterion provides three as the factor dimension: for $D = 3$ the residual error drops down to the line of the noise level.

The three corresponding orthogonal components $U_j(\nu)$, $j = 1, 2, 3$, and columns of matrix V_{ij}, $j = 1, 2, 3$, are also shown in Fig. 9.17. Since index i is connected with an individual measured spectrum, and therefore, with a particular time point within the switching process, the dependences of the elements V_{ij} of j-th matrix column on index i describe the time evolution of the NMR spectra.

Presence of three relevant orthogonal components $U_j(\nu)$ and also the time evolution of their contribution to the measured spectra (particularly

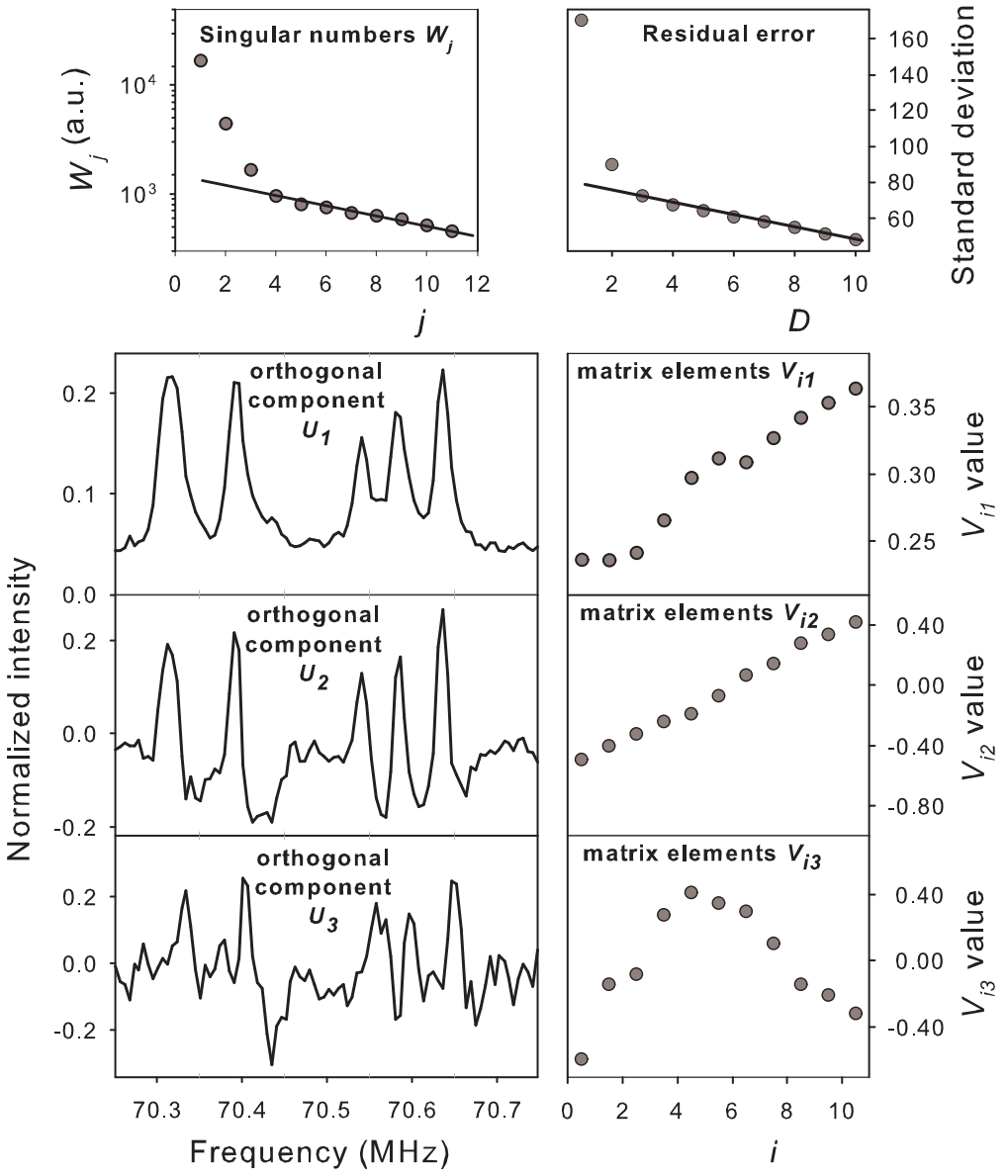

Figure 9.17: Singular Value Decomposition (SVD) of time-evolved NMR spectra. Dependences of singular numbers on index j (top left graph) and of the residual error on number of employed spectral components D (top right graph) indicate that the factor dimension is three. Below are shown graphs of the three significant orthogonal spectral components U_j (left) and the corresponding columns of the coefficient matrix V_{ij}. Time interval between i and $i+1$ corresponds to 106 minutes.

that of the third orthogonal component) indicate that the NMR picture of the switching process is somewhat more complicated than a simple conversion of one spectral profile into another. Interpretation of SVD data requires thus to propose an adequate hypothesis of the observed changes within the series of spectra.

At first, we consider the meaning of the three relevant orthogonal spectral components. Considering their shapes (Fig. 9.17) we can conclude that the first component resembles an "average" spectrum and the second component is close to a difference between the final and the first spectrum. The third component possesses rather shape of a difference between the last spectrum (Y_{11}) and this spectrum in a slightly shifted frequency scale. Such frequency shift (corresponding to a field of 7 mT) might be caused by a change of an effective demagnetization field during the switching process.

Our analysis then proceeded with construction of 'pure' spectral profiles corresponding to the zero-time (Z_0) and the time of $i = 12$ (Z_S) when we consider the switching to be completed. These spectral profiles were constructed from SVD results extrapolating the coefficients V_{ij}, $j = 1, 2, 3$, by quadratic polynomials for $i = 1, 2, 3, 4$ (to obtain V_{0j}) and for $i = 8, 9, 10, 11$ (for V_{Sj}):

$$\begin{aligned} Z_0(\nu) &= \sum_{j=1}^{3} V_{0j} W_j U_j(\nu) \\ Z_S(\nu) &= \sum_{j=1}^{3} V_{Sj} W_j U_j(\nu). \end{aligned} \tag{9.7}$$

The third spectral profile Z_Δ was constructed to characterize the effect of a frequency shift. It is well known that small spectral shifts can be very well quantitatively described by addition of a proper spectral profile. To do so, we obtained the difference spectrum $Z_{\mathrm{diff}} = Z_S(\nu) - Z_S(\nu - 10\,\mathrm{kHz})$, and then we found by a least-square fit the best approximation of Z_{diff} as a linear combination of the three SVD orthogonal components $U_j(\nu)$, given by $V_{\Delta j}$:

$$Z_{\mathrm{diff}}(\nu) \simeq \sum_{j=1}^{3} V_{\Delta j} W_j U_j(\nu) = Z_\Delta(\nu). \tag{9.8}$$

This spectral profile enables us to quantify the overall frequency shift of the spectrum as an appropriate linear combination of spectral profiles Z_S and Z_Δ. Finally, portions of the three constructed spectral shapes (Z_0, Z_S, and

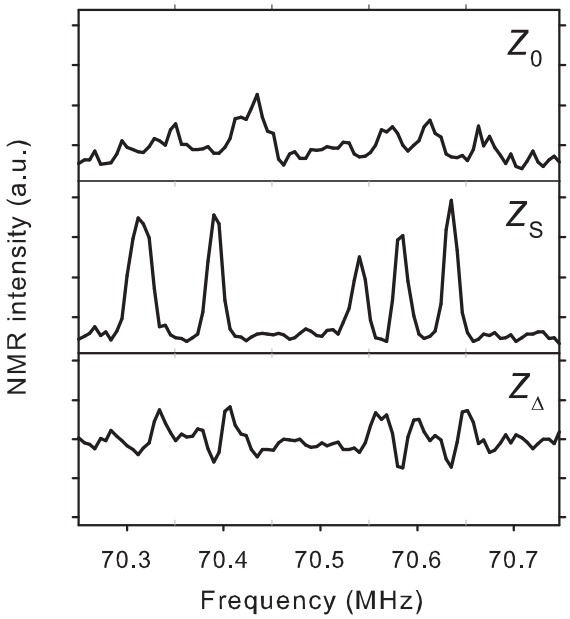

Figure 9.18: Spectral shapes of the zero-time NMR spectrum (Z_0), NMR spectrum of the completely switched sample (Z_S), and the difference spectrum (Z_Δ) caused by a 10 kHz shift of the frequency scale (corresponding to 7 mT). The spectra were constructed as linear combination of the three significant SVD orthogonal components.

Z_Δ, Fig. 9.18) in individual NMR spectra $Y_i(\nu)$ determine the amounts of resonating nuclei in the initial (P_0) and switched (P_S) environment as well as the frequency shift $\Delta\nu$, according to

$$\begin{aligned} Y_i(\nu) &= P_0(t_i)Z_0(\nu) \\ &+ P_S(t_i)[Z_S(\nu) + \Delta\nu(t_i)Z_\Delta(\nu)]. \end{aligned} \tag{9.9}$$

P_0, P_S and $\Delta\nu$ values obtained by a least-square fit of $Y_i(\nu)$ using this equation are shown in Fig. 9.19.

Even though P_0 and P_S values were determined as independent parameters in equation 9.9, their sum is always close to 100%, which confirms plausibility of our data interpretation. Common fit of $1 - P_0$ and P_S to KJMA function (eq. 9.4) yielded $n = 1.37 \pm 0.09$ and $\tau = (2.86 \pm 0.09) \times 10^4$ s. The value of Avrami exponent n agrees well with that acquired from analysis of magnetization measurement (see section 9.2.1). This implies that the character of the transformation is the same for both experimental methods, despite the remarkable difference in timescales. The variation of character-

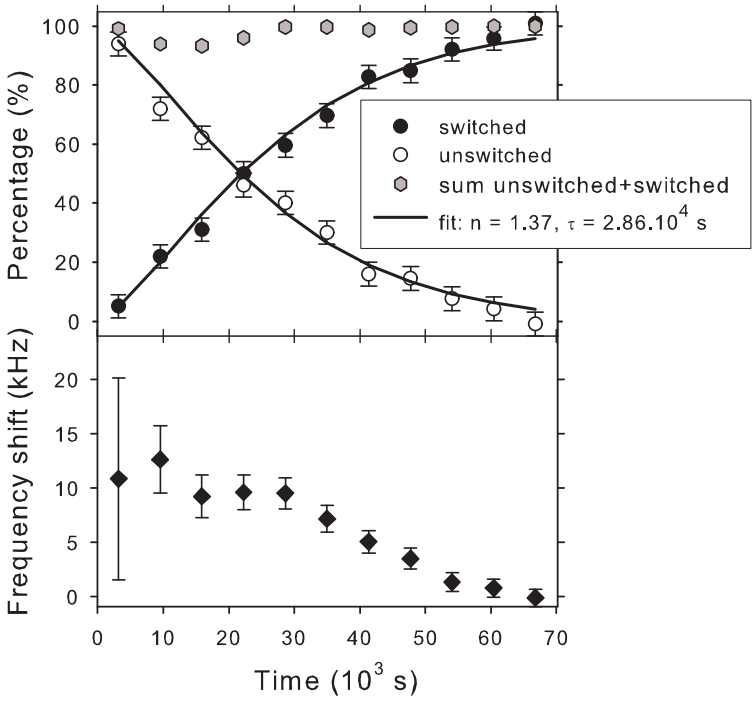

Figure 9.19: Top: Time evolution of the amounts of resonating nuclei in the initial and switched environment and their sum (circles), and the corresponding fits by Avrami equation (lines) are shown. Bottom: Time evolution of frequency shift.

istic times with small changes in temperature or magnetic field illustrates the delicate nature of the switching phenomenon.

9.2.8 Comparison of NMR and Magnetization Results

Magnetic and NMR measurements were performed and analysed in magnetite single crystalline sphere at temperatures below the Verwey transition temperature and in magnetic field set within (001) plane. The goal was to find whether magnetic easy axis switching, the phenomenon closely linked to magnetite low temperature structure and related to the Verwey transition, can also be observed by NMR spectroscopy. We have found that eight tetrahedral lines, after the field was applied perpendicularly to the original easy axis above some certain temperature, have nearly the same shape as those with field along this easy axis. Thus, we conclude that we have switched an axis to the new direction and that this switching phenomenon is visible through the NMR experiment.

We have also observed the temporal changes of the A line spectra caused by the undergoing axis switching. Qualitatively similar effects as for time dependence of magnetization caused by axis switching were found. Magnetization data (for T=60 K, B=0.8 T) and NMR data (for T=57 K, B=0.5 T), that monitored the switching process in time, were analyzed using Kolmogorov-Johnson-Mehl-Avrami theory. Our measured time dependences comply well with KJMA theory: the KJMA function (9.2) describes the experimental data in the whole measured timescales, particularly, the Avrami exponent n did not change with time during the observed switching process. The values of Avrami exponent n were very close for both applied experimental methods, which reflects that the nature of the observed phenomenon is the same, despite the timescales are quite different.

9.3 Magnetite with Cationic Vacancies

Introducing a small number of cation vacancies raises interesting question how the valence changes and whether some charge is localized near the iron vacancy. Therefore, studying local structure could provide valuable information concerning the structure of magnetite. The cation vacancy has a remarkable impact on local symmetry and electronic structure, and therefore, it is expected to change the hyperfine fields on iron nuclei in its vicinity. NMR spectroscopy can monitor these iron nuclei as their different hyperfine fields give rise to a pattern of satellite resonant lines separated from the resonance line of iron nuclei that are unaffected by proximity of the vacancy.

A series of magnetite single crystals, $Fe_{3(1-\delta)}O_4$, (δ =0.0025–0.0090) with cation vacancy located on octahedral sites were studied by means of NMR spectroscopy. The measurements were performed in zero external magnetic field at various temperatures below and above the Verwey transition. Below T_V the NMR spectra are complicated (see Fig. 9.20) and to extract information concerning the ions in the vicinity of the vacancy is hardly possible. Our measurements show only pronounced line broadening, which increases with increasing δ. Therefore, the study focuses on the cubic phase at temperatures above T_V, where the resolution of NMR spectra is much better due to higher crystal symmetry.

In the temperature interval $T_V < T < T_R$ the magnetization $\mathbf{M}$ is along the $\langle 001 \rangle$ direction, and thus in a stoichiometric magnetite all ferric ions in the A sublattice are magnetically equivalent; the same holds for Fe ions

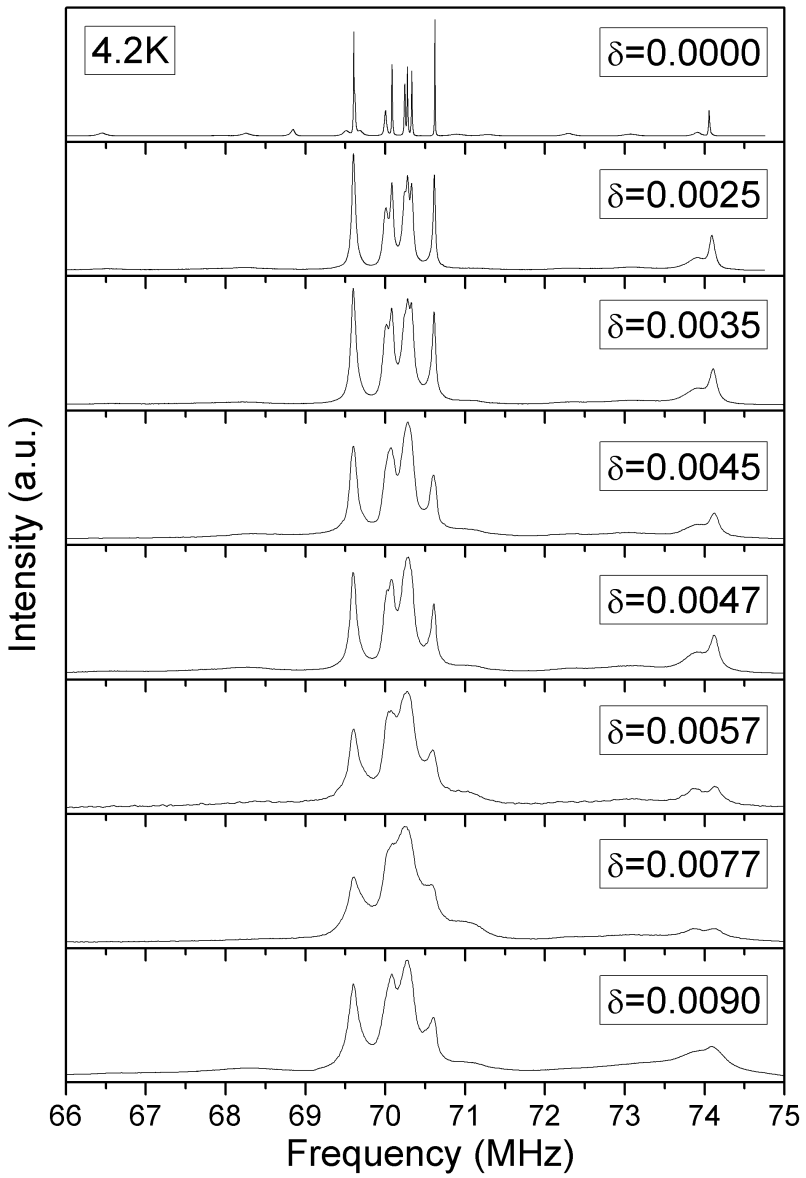

Figure 9.20: ^{57}Fe NMR spectra of eight magnetite samples with varying concentration of cationic vacancies. Spectra were measured in zero field at 4.2 K. Only lines in region 66–75 MHz are displayed.

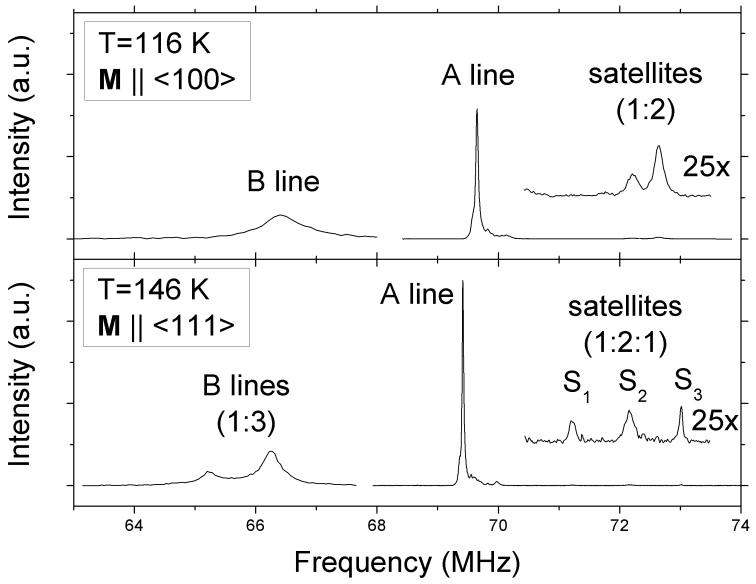

Figure 9.21: Examples of ^{57}Fe NMR spectra of sample $\delta = 0.0025$ measured well above and well below $T_{\mathrm{R}} \sim 127$ K.

in the B sublattice. The NMR signal thus consists of two lines with the intensity ratio 1:2. For $T > T_{\mathrm{R}}$, $\mathbf{M}$ is along $\langle 111 \rangle$, and due to the local trigonal symmetry of the B sites, two B lines appear. Line B_1 corresponds to those B sites for which $\mathbf{M}$ is parallel to the local trigonal axis, while B_2 originates from the remaining B sites. The A sites remain magnetically equivalent.

The presence of vacancies or impurities leads to a modification of the hyperfine field. For the iron nuclei that are close to defect corresponding change of the resonance frequency is of the order of 1 MHz, and as a consequence, satellite lines can be detected in the NMR spectra. The number of satellite lines is dictated by the topology of defect-oxygen-iron cluster, and from the intensity ratio of satellite to the main line the concentration of the defect may be determined [87, 88]. The analysis of satellite structure of the A line, that is caused by a defect in the B sublattice, revealed that for $\mathbf{M} \parallel \langle 001 \rangle$ ($T_{\mathrm{V}} < T < T_{\mathrm{R}}$) two satellites with the intensity ratio 1:2 should appear, while for $M \parallel \langle 111 \rangle$ ($T > T_{\mathrm{R}}$) three satellites intensities of which are in the ratio 1:1:2 should be observed. The center of gravity of the satellite lines should be preserved when crossing T_{R}.

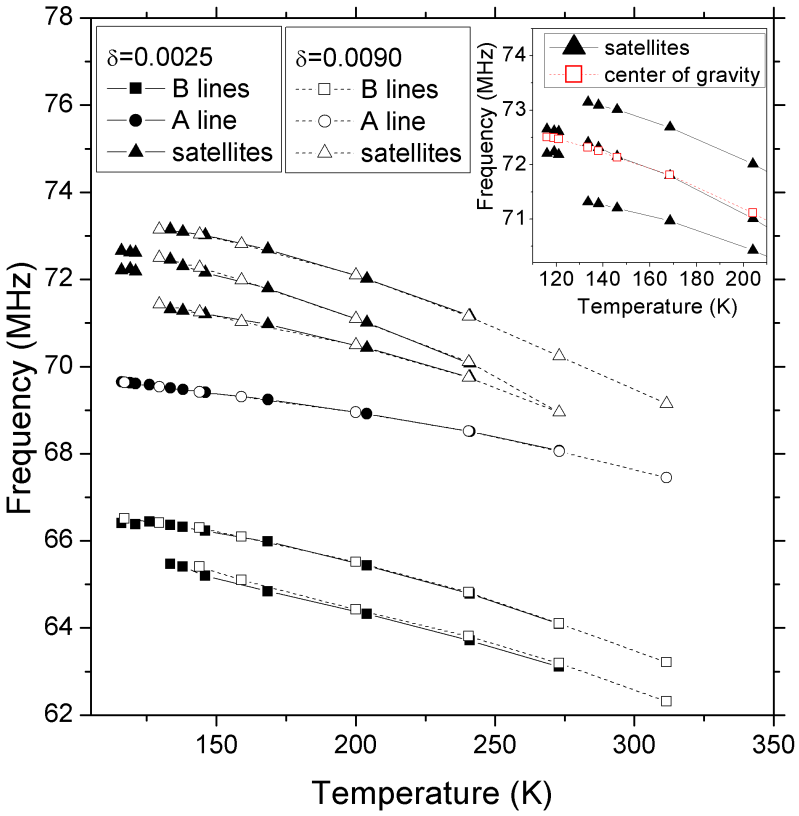

Figure 9.22: Temperature dependence of the resonance frequencies of the main lines and satellite lines for samples $\delta = 0.0025$ and $\delta = 0.0090$. The inset displays the temperature dependence of the centre of gravity of the satellite lines.

The scenario described above was fully reflected in the temperature dependent measurements of the two samples studied in detail ($\delta = 0.0025$ and $\delta = 0.0090$). For the sample with $\delta = 0.0025$ the reorientation transition was observed at temperature $T_R = 127$ K. Examples of ^{57}Fe NMR spectra measured above and below T_R are displayed in Fig. 9.21. The vacancy content NMR, determined from the ratio of satellite to main line integrated signals, agrees well with the nominal values of δ. The NMR frequencies of main and satellite lines as functions of the temperature for both $\delta = 0.0025$ and $\delta = 0.0090$ samples are displayed in Fig. 9.22. The center of gravity of the satellite lines is continuous through T_R (inset in Fig. 9.22) proving thus

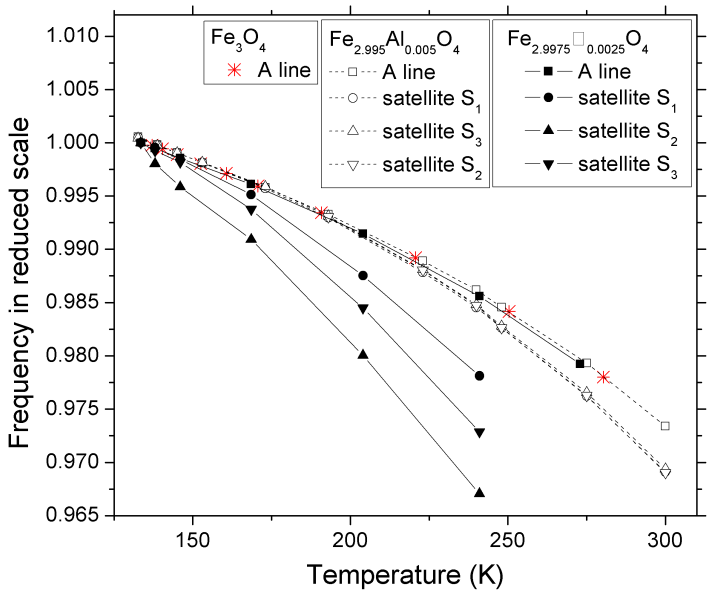

Figure 9.23: Comparison of temperature dependences of reduced frequencies for stoichiometric magnetite Fe_3O_4, Al-substituted magnetite ($Fe_{2.995}Al_{0.005}O_4$) and nonstoichiometric magnetite sample $\delta = 0.0025$ ($Fe_{2.9975}\square_{0.0025}O_4$). The frequency scale was normalized so that the frequencies at temperature 134 K are equal to 1.

that the satellites originate from the same Fe(A)-O-vacancy complex.

It can be seen in Fig. 9.22 that the frequencies of all three satellite lines S_1, S_2 and S_3 decrease more rapidly with increasing temperature than the frequency of the main line A. This behavior is clearly connected with the smaller exchange field caused by one missing exchange interaction Fe(A)-O-Fe(B). Similar effect was observed earlier on Al-substituted magnetite [89]. Detailed comparison of these two systems shows that for $Fe_{3(1-\delta)}O_4$ system the decrease of frequency with increasing temperature is faster, see Fig. 9.23, where the plots are shown in a reduced scale.

Of importance is another aspect seen in Fig. 9.23: while the temperature dependences of the reduced frequency in Al-substituted magnetite are the same for all satellite lines, corresponding dependences in the magnetite with vacancies clearly differ. Such anomaly could only be explained by different exchange fields, and as the satellites originate from the same Fe(A)-O-vacancy complex, it means that the exchange interaction of this

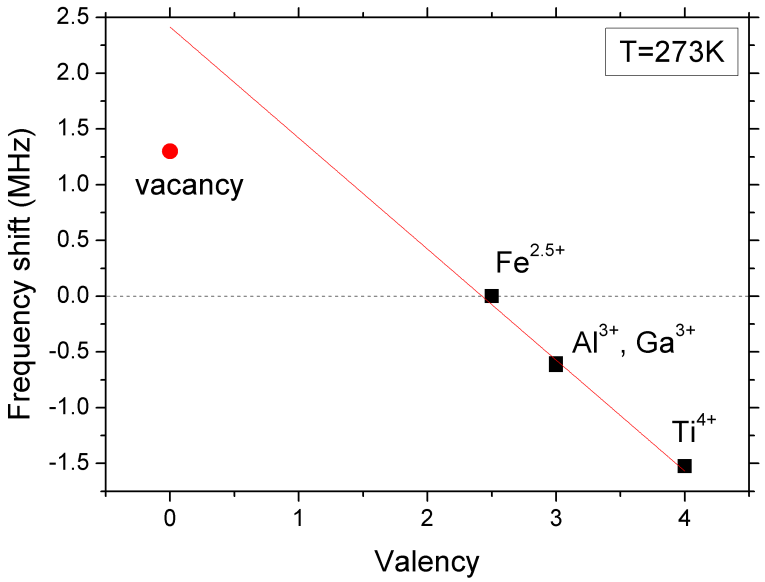

Figure 9.24: Center-of-gravity shift of satellites is plotted as a function of nominal valency of the substitution/defect in neighboring octahedral B site for Ti^{4+}, Al^{3+}, Ga^{3+} and the vacancy. The point denoted $Fe^{2.5+}$ represents the undisturbed main line.

Fe(A) is anisotropic. Furthermore, Fe(A) in question remains in the trivalent state with zero angular momentum in the ground state, as documented by almost unchanged resonance frequency. For anisotropy of exchange to appear, the orbital momentum must be non-zero. The possible mechanism is that the mobile electrons on the B sublattice are repelled by the vacancy and tetravalent iron in the low spin state appears on the site nearest to the vacancy. Fe^{4+} possesses non-zero orbital momentum, thus Fe^{3+}(A)-O-Fe^{4+}(B) exchange would be anisotropic.

Our data in Ref. [90] (obtained at temperature 273 K) enabled us to compare frequency shifts of vacancy-induced satellites with the ones induced by Al^{3+}, Ga^{3+} and Ti^{4+} substitutions entering B sites. As seen in Fig. 9.24 the shift decreases as the valency of the defect increases. Possible explanation lies in the movement of the oxygen ions caused by the defect—defect with higher valency will attract more strongly the oxygen anion, and as a consequence, the distance of this anion to the nearest Fe(A) will increase. Increase of this distance should then lead to a smaller hybridization of Fe(A)

compound	Ti/Ga/Al radius (a.u.)	Fe radius (a.u.)	O radius (a.u.)	matrix size (RK_{max})	k-points (division)	G_{max}
$(Fe_{16})[Fe_{31}Ti]O_{64}$	1.8	1.8	1.6	12225 (7.0)	28 (6 6 6)	16
$(Fe_{16})[Fe_{31}Al]O_{64}$	1.8	1.8	1.6	12219 (7.0)	28 (6 6 6)	16
$(Fe_{16})[Fe_{31}Ga]O_{64}$	1.8	1.8	1.6	12226 (7.0)	28 (6 6 6)	16
$(Fe_{16})[Fe_{31}\square]O_{64}$	1.8	1.8	1.6	12225 (7.0)	28 (6 6 6)	16

Table 9.8: Parameters used for calculations are displayed. RK_{max} denotes $RMT_{min} \times K_{max}$. 1 a.u. = 0.0529177 nm.

$3d$ electrons with the $2p$ electrons of oxygen, which in turn will be reflected in the increase of the hyperfine field.

In order to further inspect changes connected with these substitutions (or vacancy) in the octahedral site, *ab initio* calculations were performed on the respective compounds, i.e. magnetite structures with Ti, Al, or Ga substitution in octahedral site and magnetite structure with a vacancy. The concentrations of substitutions or vacancies in the experimentally studied compounds were rather low. Therefore, to obtain reasonably low concentrations, supercell structures $2 \times 2 \times 2$ were created, and one octahedral iron atom was either substituted by Ti, Al, or Ga, or removed. Naturally, this lowered the symmetry of the crystallographic unit cell: the $Fd\bar{3}m$ cubic cell $2a \times 2a \times 2a$ changed to rhombohedral R3m cell $a\sqrt{2} \times a\sqrt{2} \times 2a\sqrt{3}$ with substitution (or vacancy) positioned at $(\frac{1}{2}, \frac{1}{2}, \frac{1}{2})$. Parameters used for calculations are displayed in Table 9.8, GGA+U method was employed with $U_{\text{eff}} = 4.5$ eV for Fe atoms.

Internal structural parameters of the substituted supercells and the supercell with vacancy were optimized with respect to total energy and atomic forces. Therefore, one of the results is how dimension of the oxygen octahedron changes with different substitution. Table 9.9 displays the substitution-oxygen distances, together with calculated magnetic moments of Fe(A) and Fe(B). Geometric properties of the triad Fe(A)-O-X(B) vary strongly for different X(B) (X = Ti, Ga, Al or vacancy $\square$). When the differences in ionic radii are taken into account, the displacement of oxygen towards the nearest Fe(A) depends monotonously on the valence of X(B), and thus supports the conclusions drawn from the frequency shifts in NMR spectra (Fig. 9.24).

compound		$Ti:Fe_3O_4$	$Ga:Fe_3O_4$	$Al:Fe_3O_4$	Fe_3O_4	$\square:Fe_3O_4$
nominal valence		Ti^{4+}	Ga^{3+}	Al^{3+}	$Fe^{2.5+}$	
ionic radius (Shannon, nm)		0.0745	0.0760	0.0675	0.0785–0.0920 (Fe^{3+}–Fe^{2+})	
X-O-Fe(A) distances (nm)	X-O	0.19764	0.20046	0.19393	0.20547	0.22004
	O-Fe(A)	0.19101	0.19013	0.18835	0.18950	0.18302
Fe(A) magnetic moment (μ_B)	min.	3.884	3.883	3.874	3.899	3.891
	min.	3.884	3.883	3.874	3.899	3.891
	max.	3.904	3.899	3.911	3.899	3.904
Fe(B) magnetic moment (μ_B)	min.	−3.425	−3.418	−3.450	−3.784	−3.506
	mean	−3.615	−3.588	−3.697	−3.784	−3.817
	max.	−3.979	−3.983	−4.002	−3.784	−3.996

Table 9.9: Calculated geometric parameters and magnetic moments of irons are displayed for several octahedrally substituted magnetites and for magnetite with octahedral vacancy. Compound notation: $Ti:Fe_3O_4$ stands for $(Fe_{16})[Fe_{31}Ti]O_{64}$ etc.

9.4 Summary of Magnetite Results

This chapter presented three approaches, each of them being a promising path to the complete assignment of ^{57}Fe NMR lines. Anisotropy of hyperfine field in magnetite of P2/c structure was calculated *ab initio* and qualitatively compared to experimental dependences of ^{57}Fe NMR spectra on direction of external magnetic field. By dividing both the calculated and experimental dependences into three groups according to their character, it was possible to assign a set of lines in Cc structure to a particular line of P2/c structure. The magnetocrystalline anisotropy, which was also calculated, reproduced the magnetic easy, intermediate and hard axes.

With respect to switching of easy axis in magnetite below the Verwey transition, magnetic and NMR measurements were performed and analysed. We detected changes in the ^{57}Fe NMR experimental spectra that evidence the structural transition interrelated with the axis switching. We also observed the switching process in time and analyzed the dynamics, contained in magnetization and NMR data, by using Kolmogorov-Johnson-Mehl-Avrami theory. Our measured time dependences comply well with KJMA theory, particularly, the Avrami exponent did not change with time during the observed switching process. Qualitatively similar effects for both experimental methods were found: the values of Avrami exponent were very close, which reflects that the nature of the observed phenomenon is the same, despite the timescales are quite different.

Magnetites with vacancies in octahedral sites were studied by ^{57}Fe NMR spectroscopy and by *ab initio* calculations. In cubic phase above the Verwey transition the satellite structure induced by vacancies was identified. The temperature dependence of satellite lines indicated that the presence of vacancy leads to a redistribution of the electrons in octahedral sublattice and to appearance of iron ions possessing appreciable orbital moment. The geometry of oxygen octahedron was studied in magnetite with vacancy and with different substitutions in B site by comparison of frequency shifts in the NMR spectra and by calculating the electronic structures. The displacement of oxygen towards the nearest tetrahedral iron was found to depend monotonously on the valence of substitution.

Chapter 10

Conclusions

Three systems of transition metal oxides with spinel structure, manganese ferrite, lithium ferrite and magnetite, were studied experimentally by nuclear magnetic resonance spectroscopy and from the first principles by calculations of electron structure. These methods showed to be beneficial for investigation of the studied problematics, whether applied individually and in cooperation, as the combination of accurate present-day approaches allowed comparison and mutual verification, which produced a number of outcomes:

1. Manganese ferrites with various degrees of manganese-iron inversion and with different manganese contents were investigated. The main resonance lines of ^{57}Fe NMR spectrum were unambiguously assigned to iron nuclei in corresponding crystallographic positions, and thus the magnetic structure of manganese ferrite was confirmed to comply with the Goodenough-Kanamori-Anderson rules, i.e. all moments within a given sublattice are parallel and the total magnetizations of sublattices are mutually antiparallel.

2. Values of degrees of inversion were evaluated from the intensities of spectral lines in the NMR experiment, and a systematic difference was found in comparison to results from neutron diffraction and magnetization measurements. Besides analyzing the intensities of NMR lines, we performed *ab initio* calculations of four different arrangements that have shown that a pairing of Fe(A)-Mn(B) is energetically favourable. Based on these results, we draw conclusion that the distribution of inverted iron atoms in the A sublattice is not random.

3. By calculating the density of states we have also found out that applying GGA+U opens the insulating gap in the band structure of manganese ferrite.

4. On ordered lithium ferrite we demonstrated the potential of *ab initio* calculations to complement the NMR method and to become a valuable tool for interpretation of NMR spectra. Anisotropy of hyperfine fields on iron nuclei was derived from the series of *ab initio* calculations of electron structure of lithium ferrite and compared to experimental ^{57}Fe NMR results. Matching the calculated anisotropies to the experimental ones allowed to assign unambiguously the individual lines in the ^{57}Fe NMR spectra to crystal positions. Thus we revealed a new path for assignment and interpretation of NMR spectra, allowing to use NMR to study even more complicated systems.

5. We acquired additional NMR spectrum at lower frequencies, and assigned it to ^{7}Li resonance, based on the calculated hyperfine fields.

6. The study of magnetite followed the procedures developed on lithium ferrite: Anisotropies calculated in the P2/c structure were qualitatively compared to experimental dependences of ^{57}Fe NMR spectra on direction of external magnetic field. By dividing both the calculated and experimental dependences into three groups according to their character, it was possible to assign a set of lines in Cc structure to particular lines of P2/c structure. These results represent a promising method that could be a step towards solving the complicated structure of magnetite at low temperatures.

7. The switching of magnetic easy axis induced by external magnetic field and the accompanying structural changes were studied by means of magnetic and NMR measurements below the Verwey transition. We detected changes in the ^{57}Fe NMR experimental spectra that evidence the structural transition interrelated with the axis switching. Moreover, we observed the switching process in the ocurse of time and analyzed its dynamics by formalism of Kolmogorov-Johnson-Mehl-Avrami theory. Our measured time dependences complied well with KJMA theory, particularly, the Avrami exponent did not change with time during the observed switching process. Qualitatively similar effects for both experimental methods were found: the values of Avrami exponent were very close, which illustrated that the nature of

the observed phenomenon is the same, despite the markedly different timescales of the two methods.

8. Magnetites with vacancies in octahedral sites were studied by ^{57}Fe NMR spectroscopy and by *ab initio* calculations. In cubic phase above the Verwey transition we identified the satellite structure induced by vacancies, and from temperature dependence of these satellites we concluded that the presence of vacancy leads to a redistribution of the electrons in octahedral sublattice connected with appearance of iron ions possessing appreciable orbital moment. For comparison, the geometry of oxygen octahedron was then evaluated also in magnetites with different substitutions in octahedral site. The displacement of oxygen towards the nearest tetrahedral iron was found to depend monotonously on the valence of substitution.

Bibliography

[1] W. H. von Aulock. *Handbook of Microwave Ferrite Materials*. Academic Press, New York, 1965. [cited at p. 3]

[2] A. Gupta and J. Z. Sun. *J. Magn. Magn. Mat.*, 200:24, 1999. [cited at p. 3]

[3] W. Eerenstein, T. T. M. Palstra, S. S. Saxena, and T. Hibma. *Phys. Rev. Lett.*, 88:247204, 2002. [cited at p. 3]

[4] S. Krupička. *Fyzika feritů a příbuzných magnetických kysličníků*. Academia, Praha, 1969. [cited at p. 3]

[5] J. S. Griffith. *The theory of transition-metal ions*. Cambridge University Press, Cambridge, 1961. [cited at p. 6]

[6] Z. Jirák, Z. Šimša, J. Šimšová, V. Roskovec, S. Vratislav, and V. A. M. Brabers. In *Proceeding of International Conference on Magnetism ICM-73*, volume V, page 260, Moscow, 1974. Nauka. [cited at p. 7, 40]

[7] Z. Šimša and V. A. M. Brabers. *IEEE Trans. Magn.*, Mag-11:1303, 1975. [cited at p. 7, 9]

[8] H. Yasuoka and A. Hirai. *J. Phys. Soc. Jap.*, 22:174, 1967. [cited at p. 7]

[9] M. Rotter, B. Sedlák, and Z. Šimša. *Czech. J. Phys. B*, 27:1189, 1977. [cited at p. 7, 9]

[10] A. Kokalj. *Comp. Mater. Sci*, 28:155, 2003. Code available from `http://www.xcrysden.org/`. [cited at p. 8, 11, 13]

[11] J. Goodenough. *Magnetism and the Chemical Bond*. John Wiley and Sons, New York, 1963. [cited at p. 8, 9]

[12] P. W. Anderson. *Solid State Phys.*, 14:99, 1963. [cited at p. 8, 9]

[13] R. Vautier and M. Paulus. *Landolt-Bornstein, Numerical Data and Functional Relationships in Science and Technology, New Series*, volume 12, page 122. Springer-Verlag, Berlin, 1980. [cited at p. 9]

[14] A. J. Heeger and T. W. Houston. *J. Phys. Soc. Jap.*, 19:A661, 1964. [cited at p. 9]

[15] Y. Yasuoka. *Phys. Rev.*, 135:1182, 1964. [cited at p. 9]

[16] T. Kubo, A. Hirai, and H. Abe. *J. Phys. Soc. Jap.*, 26:1094, 1966. [cited at p. 9]

[17] T. Kubo, H. Yasuoka, and A. Hirai. *J. Phys. Soc. Jap.*, 21:812, 1969. [cited at p. 9]

[18] T. Shirakashi and T. Kubo. *Am. Mineral.*, 64:599, 1979. [cited at p. 9]

[19] N. M. Kovtun, A. M. Kotelva, and A. A. Shemyakov. *J. Exp. Theor. Phys. Lett.*, 45:320, 1987. [cited at p. 9, 43, 58, 60, 79]

[20] J. H. Shim, S. Lee, and B. I. Min. *Phys. Rev. B*, 75:134406, 2007. [cited at p. 9, 42]

[21] D. J. Singh, M. Gupta, and R. Gupta. *Phys. Rev. B*, 65:064432, 2002. [cited at p. 9, 52, 57]

[22] Xu Zuo, B. Barbiellini, and C. Vittoria. *J. Mag. Mag. Mater.*, 306:272, 2004. [cited at p. 9, 52]

[23] G. F. Dionne. *J. Appl. Phys.*, 99:08M913, 2006. [cited at p. 9]

[24] H. Štěpánková, B. Sedlák, V. Chlan, P. Novák, and Z. Šimša. *Phys. Rev. B*, 77:092416, 2008. [cited at p. 9, 43]

[25] I. G. Austin and D. Elwell. *Contempt. Phys.*, 11:455, 1970. [cited at p. 11]

[26] E. W. Gorter. *Philips Res. Rep.*, 9:295, 1954. [cited at p. 11]

[27] S. Ogawa, Y. Morimoto, and Y. Kimura. *J. Phys. Soc. Jap.*, 17:1671, 1962. [cited at p. 11]

[28] H. Yasuoka. *J. Phys. Soc. Jap.*, 11:1071, 1962. [cited at p. 11]

[29] V. D. Doroshev, N. M. Kovtun, and V. N. Selesnev. *Sov. Phys. Sol. State*, 13:911, 1971. [cited at p. 11, 67]

[30] V. D. Doroshev, V. A. Klochan, N. M. Kovtun, and V. N. Selesnev. *Phys. Status Solidi A*, 9:679, 1972. [cited at p. 11, 67, 70, 71, 72]

[31] P. Novák, H. Štěpánková, J. Englich, J. Kohout, and V. A. M. Brabers. *Phys. Rev. B*, 61:1256, 2000. [cited at p. 12, 14]

[32] M. Iizumi and G. Shirane. *Solid State Commun.*, 17:433, 1975. [cited at p. 12]

[33] M. Mizoguchi. *J. Phys. Soc. Jpn.*, 70:2333, 2001. [cited at p. 12, 14, 83, 87, 104]

[34] J. P. Wright, J. P. Attfield, and P. G. Radaelli. *Phys. Rev. B*, 66:214422, 2002. [cited at p. 12, 13, 83, 90]

[35] G. Subías, J. García, and J. Blasco. *Phys. Rev. B*, 71:155103, 2005. [cited at p. 13]

[36] G. Kh. Rozenberg, M. P. Pasternak, W. M. Xu, Y. Amiel, M. Hanfland, M. Amboage, R. D. Taylor, and R. Jeanloz. *Phys. Rev. Lett.*, 96:045705, 2006. [cited at p. 13]

[37] K. P. Belov. *Phys. Usp.*, 36:380, 1993. [cited at p. 14]

[38] A. R. Muxworthy and E. McClelland. *Geophys. J. Int.*, 140:101, 2000. [cited at p. 14]

[39] P. Novák, H. Štěpánková, J. Englich, and J. Kohout. Temperature dependence of NMR in magnetite. In *Ferrites: Proceeding of the Eight International Conference on Ferrites*, 2001. [cited at p. 14, 99]

[40] B. A. Calhoun. *Phys. Rev.*, 94:1577, 1954. [cited at p. 15]

[41] E. Vittoratos, I. Baranov, and P. P. M. Meincke. *J. Appl. Phys.*, 42:1633, 1971. [cited at p. 15]

[42] G. Król, J. Kusz, Z. Tarnawski, Z. Kąkol, W. Tabiś, and A. Kozłowski. *Acta Phys. Pol. A*, 109:601, 2006. [cited at p. 15]

[43] G. Król, J. Kusz, Z. Tarnawski, Z. Kąkol, A. Kozłowski, and J. M. Honig. *J. Alloys Compd.*, 442:83, 2007. [cited at p. 15]

[44] Z. Kąkol and J. M. Honig. *Phys. Rev. B*, 40:9090, 1989. [cited at p. 15, 104]

[45] R. Aragón, R. J. Rasmussen, J. P. Shepherd, J. W. Konitzer, and J. M. Honig. *J. Mag. Mag. Mater.*, 54–55:1335, 1986. [cited at p. 15]

[46] A. Abragam. *Principles of Nuclear Magnetism*. Clarendon Press, Oxford, 1978. [cited at p. 16]

[47] C. P. Slichter. *Principles of Magnetic Resonance*. Springer-Verlag, New York, 1990. [cited at p. 16]

[48] M. Levitt. *Basics of Nuclear Magnetic Resonance*. John Wiley and Sons, New Jersey, 2001. [cited at p. 16]

[49] E. A. Turov and M. P. Petrov. *Nuclear Magnetic Resonance in Ferro- and Antiferromagnets*. Halsted Press-Wiley, 1972. [cited at p. 16, 100, 101]

[50] H. Štěpánková. Anizotropie hyperjemného pole ve ferimagnetických oxidech, habilitační práce, 1999. [cited at p. 22]

[51] D. J. Singh. *Planewaves, Pseudopotentials and the LAPW Method*. Kluwer Academic, Boston, 1994. [cited at p. 26]

[52] E. Sjøstedt, L. Nordström, and D. J. Singh. *Solid State Commun.*, 114:15, 2000. [cited at p. 26]

[53] P. Blaha, K. Schwarz, G. K. H. Madsen, D. Kvasnicka, and J. Luitz. *WIEN2k, An Augmented Plane Wave + Local Orbitals Program for Calculating Crystal Properties*. Techn. Universität Wien, 2001. ISBN 3-9501031-1-2. [cited at p. 26]

[54] V. I. Anisimov, J. Zaanen, and O. K. Andersen. *Phys. Rev. B*, 44:943, 1991. [cited at p. 27, 34, 68, 83]

[55] S. Blügel, H. Akai, R. Zeller, and P. H. Dederichs. *Phys. Rev. B*, 35:3271, 1986. [cited at p. 28]

[56] R. Coehoorn. *J. Mag. Mag. Mater.*, 159:55, 1996. [cited at p. 28, 35, 36]

[57] L. Severin, M. Richter, and L. Steinbeck. *Phys. Rev. B*, 55:9211, 1997. [cited at p. 28]

[58] P. H. Dederichs, R. Zeller, H. Akai, and H. Ebert. *J. Mag. Mag. Mater.*, 100:241, 1991. [cited at p. 28]

[59] V. S. Stepanyuk, R. Zeller, P. H. Dederichs, and I. Mertig. *Phys. Rev. B*, 49:5157, 1994. [cited at p. 28]

[60] V. Chlan, P. Novák, H. Štěpánková, J. Englich, J. Kuriplach, and D. Nižňanský. *J. Appl. Phys.*, 99:08M903, 2006. [cited at p. 28, 37]

[61] V. Procházka, B. Sedlák, H. Štěpánková, M. Pfeffer, R. Řezníček, and V. Chlan. New experimental procedure for broad nmr spektra measurement. In *Proceedings of the 16th Conference of Czech and Slovak Physicists 2008*, page 212, Hradec Králové, 2009. [cited at p. 29]

[62] J. P. Perdew, S. Burke, and M. Ernzerhof. *Phys. Rev. Lett.*, 77:3865, 1996. [cited at p. 33, 53, 68, 83]

[63] P. Novák, J. Kuneš, W. E. Pickett, Wei Ku, and F. R. Wagner. *Phys. Rev. B*, 67:140403(R), 2003. [cited at p. 35]

[64] H. Štěpánková, J. Englich, E. G. Caspary, and H. Lütgemeier. *J. Magn. Magn. Mater.*, 177:253, 1998. [cited at p. 36, 104]

[65] V. Chlan. Studium hyperjemných interakcí v magnetických granátech yttria a lutecia metodou NMR a NQR, 2004. [cited at p. 37]

[66] P. Novák and V. Chlan. *Submitted to Phys. Rev. B*, 2009. [cited at p. 38]

[67] V. A. M. Brabers. *Ber. Dt. Keram. Ges.*, 47:648, 1970. [cited at p. 39]

[68] D. F. Howarth, J. A. Weil, and Z. Zimpel. *J. Magn. Res.*, 161:215, 2003. [cited at p. 46]

[69] V. N. Seleznev, I. K. Pukhov, A. I . Drokin, and V. A. Shapovalov. *Fiz. Tverd. Tela*, 12:885, 1970. [cited at p. 67]

[70] P. B. Braun. *Nature*, 170:1123, 1952. [cited at p. 68]

[71] A. I. Smolentsev, A. B. Meshalkin, N. V. Podberezskaya, and A. B. Kaplun. *J. Struct. Chem.*, 49:953, 2008. [cited at p. 68]

[72] C. Lee, Ph. Ghosez, and X. Gonze. *Phys. Rev. B*, 50:13379, 1994. [cited at p. 69]

[73] J. Goniakowski, J. M. Holender, L. N. Kantorovich, and M. J. Gillan. *Phys. Rev. B*, 53:957, 1996. [cited at p. 69]

[74] F. Favot and A. Dal Corso. *Phys. Rev. B*, 60:11427, 1999. [cited at p. 69]

[75] K. Abe, Y. Miyamoto, and S. Chikazumi. *J. Phys. Soc. Jap.*, 41:1894, 1976. [cited at p. 84, 91]

[76] E. Nazarenko, J. E. Lorenzo, Y. Joly, J. L. Hodeau, D. Mannix, and C. Marin. *Phys. Rev. Lett.*, 97:056403, 2006. [cited at p. 90]

[77] A. N. Kolmogorov. *Izv. Akad. Nauk SSSR, Ser. Materm.*, 3:355, 1937. [cited at p. 94]

[78] J. Johnson and R. Mehl. *Trans. AIME*, 135:416, 1939. [cited at p. 94]

[79] M. Avrami. *J. Chem. Phys.*, 7:1103, 1939. [cited at p. 94]

[80] M. Avrami. *J. Chem. Phys.*, 8:212, 1940. [cited at p. 94]

[81] M. Avrami. *J. Chem. Phys.*, 9:117, 1941. [cited at p. 94]

[82] P. Chandra. *Phys. Rev. A*, 39:3672, 1989. [cited at p. 95]

[83] H. Orihara, S. Hashimoto, and Y. Ishibashi. *J. Phys. Soc. Jpn.*, 63:1031, 1994. [cited at p. 95]

[84] A. A. Hirsch and G. Galeczki. *J. Magn. Magn. Mater.*, 114:179, 1992. [cited at p. 95]

[85] H. L. Richards, M. A. Novotny, and P. A. Rikvold. *Phys. Rev. B*, 54:4113, 1996. [cited at p. 95]

[86] E. R. Malinowski. *Factor Analysis in Chemistry*. Wiley, third edition, 1972. [cited at p. 108]

[87] J. Englich, P. Novák, and H. Lütgemeier. *Int. J. Modern Phys. B*, 12:609, 1998. [cited at p. 116]

[88] H. Štěpánková, J. Kohout, J. Englich, and P. Novák. *Hyperfine Interact.*, 131:2, 2000. [cited at p. 116]

[89] E. Gamaliy, H. Štěpánková, J. Englich, J. Kohout, A. Shnezko, P. Novák, and V. A. M. Brabers. *J. Magn. Magn. Mater.*, 242:732, 2002. [cited at p. 118]

[90] V. Chlan, E. Gamaliy, H. Štěpánková, K. Kouřil, J. Englich, J. Kohout, and V. A. M. Brabers. *J. Magn. Magn. Mater.*, 310:2555, 2007. [cited at p. 119]

Articles Related to the Thesis

1. V. Chlan, H. Štěpánková, V. Procházka, J. Englich, J. Kohout, D. Nižňanský, J. Buršík: Antisite defects in lutetium and yttrium iron garnets prepared by liquid mix technique, *J. Magn. Magn. Mater.*, 290:993–996, 2005.

2. J. Kohout, E. Gamaliy, H. Štěpánková, J. Englich, V. Procházka, V. Chlan, V. A. M. Brabers: NMR of ^{57}Fe, ^{69}Ga and ^{71}Ga in Ga substituted magnetite, *J. Magn. Magn. Mater.*, 290:1018–1020, 2005.

3. V. Chlan, P. Novák, H. Štěpánková, J. Englich, J. Kuriplach, D. Nižňanský: Hyperfine interactions in lutetium iron garnet, *J. Appl. Phys.*, 99:08M903, 2006.

4. V. Chlan, E. Gamaliy, H. Štěpánková, K. Kouřil, J. Englich, J. Kohout, V. A. M. Brabers: Nuclear magnetic resonance of ^{57}Fe in Al, Ga and Ti-substituted magnetite above Verwey temperature, *J. Magn. Magn. Mater.*, 310:2555-2557, 2007.

5. V. Chlan, V. Procházka, H. Štěpánková, B. Sedlák, P. Novák, Z. Šimša, V. A. M. Brabers: ^{57}Fe NMR study of manganese ferrites, *J. Magn. Magn. Mater.*, 320:e96-e99, 2008.

6. H. Štěpánková, B. Sedlák, V. Chlan, P. Novák, Z. Šimša : ^{57}Fe NMR and spin structure of manganese ferrite, *Phys. Rev. B*, 77:092416, 2008.

7. V. Procházka, B. Sedlák, H. Štěpánková, M. Pfeffer, R. Řezníček, V. Chlan: New experimental procedure for broad NMR spektra measurement, Proceedings of the 16th Conference of Czech and Slovak Physicists 2008, 212-221, Hradec Králové, 2009

8. V. Chlan, P. Novák, H. Štěpánková, R. Řezníček, K. Kouřil, A. Kozłowski: Electronic structure and hyperfine fields in non-stoichiometric magnetite above the Verwey transition, *J. Magn. Magn. Mater.*, In Press,

DOI: 10.1016/j.jmmm.2009.03.026

9. V. Chlan, P. Novák: Ab-initio calculation of electronic structure of partially inverted manganese ferrite, *J. Magn. Magn. Mater.*, In Press, DOI: 10.1016/j.jmmm.2009.06.001

10. P. Novák, V. Chlan: Contact hyperfine field at Fe nuclei from density functional calculations, Submitted to *Phys. Rev. B*, 2009.

11. V. Chlan, K. Kouřil, H. Štěpánková, R. Řezníček, J. Štěpánek, W. Tabiś, G. Król, Z. Tarnawski, Z. Kąkol, A. Kozłowski: Magnetic axis switching phenomenon in magnetite: NMR Studies, Submitted to *Phys. Rev. B*, 2009.

Other Articles

12. K. Kouřil, J. Kohout, H. Štěpánková, J. Englich, V. Chlan: Nuclear magnetic resonance of ^{57}Fe from magnetic domains and walls in yttrium iron garnet, *Acta Phys. Slovaca*, 56:31–34, 2006.

13. V. Procházka, H. Štěpánková, J. Štěpánek, A. Snezhko, V. Chlan, K. Kouřil: Exchange interactions in barium hexaferrite, *Acta Phys. Slovaca*, 56:165–168, 2006.

14. H. Štěpánková, J. Englich, J. Štěpánek, J. Kohout, M. Pfeffer, J. Černá, V. Chlan, V. Procházka, E. Bunyatova: Nuclear spin-lattice relaxations in ethanol with dissolved TEMPO radicals, *Acta Phys. Slovaca*, 56:141–144, 2006.

15. K. Kouřil, V. Chlan, H. Štěpánková, P. Novák, K. Knížek, J. Hybler, T. Kimura, Y. Hiraoka, J. Buršík: Hyperfine interactions in magnetoelectric hexaferrite system, *J. Magn. Magn. Mater.*, In Press, DOI: 10.1016/j.jmmm.2009.03.011

16. H. Štěpánková, K. Kouřil, V. Chlan, P. Görnert, R. Müller, J. Štěpánek: Internal magnetic fields in submicron particles of barium hexaferrite detected by ^{57}Fe NMR, *J. Magn. Magn. Mater.*, In Press, DOI: 10.1016/j.jmmm.2009.04.002

17. V. Procházka, M. Sikora, Cz. Kapusta, H. Štěpánková, V. Chlan, K. Knížek, Z. Jirák: Local surrounding of Mn in $LaMn_{1-x}Co_xO_3$ compounds by means of EXAFS on MnK: *J. Magn. Magn. Mater.*, In Press, DOI: 10.1016/j.jmmm.2009.06.002